UNSTABLE RADIATIVE-DYNAMICAL INTERACTIONS

by

STEVEN JOHN GHAN

B. S., Atmospheric Sciences
University of Washington (1979)
S. M., Meteorology, Massachusetts
Institute of Technology (1981)

Submitted to the Department of
Earth, Atmospheric and Planetary Sciences
in Partial Fulfillment of
the Requirements of the Degree of
Doctor of Science

at the

Massachusetts Institute of Technology
April 1988

Signature of Author _____
Department of Earth, Atmospheric, and
Planetary Sciences
April 1988

Certified by _____
Peter H. Stone
Professor, Meteorology
Thesis Supervisor

Accepted by _____
Chairman, Departmental Graduate Committee

UNSTABLE RADIATIVE-DYNAMICAL INTERACTIONS

by

STEVEN JOHN GHAN

Submitted to the Department of
Earth, Atmospheric and Planetary Sciences
on April 14, 1988 in partial fulfillment of the requirements for
the Degree of Doctor of Science in Meteorology

Abstract

The interaction between trace shortwave radiative absorbers and the dynamical circulation is shown to be linearly unstable for horizontally uniform basic states with a vertical gradient in the basic state absorber mixing ratio. Two types of instability are identified, described as the advective mode and the propagating mode. The advective mode is usually unstable when the basic state absorber mixing ratio decreases with height. Upward motion, high absorber concentration and warm temperatures are typically in phase for this mode. Growth rates, which can be competitive with those associated with baroclinic instability, are largest for perturbations that are much shorter than the internal deformation radius. Thus, the requirement that the basic state be horizontally uniform is often satisfied for the advective mode. The propagating mode is normally unstable when the basic state absorber mixing ratio increases with altitude. Propagating waves such as Rossby and inertia-gravity waves are amplified by the feedback with absorber transport and radiative heating. Growth rates for the propagating mode are usually bounded by the frequency of oscillation of the ambient wave, an important limitation for slowly propagating waves such as Rossby waves. Vertical transport of the absorber by the amplifying mode is down the basic state absorber gradient in each case. Complicating factors such as the effects of dissipative processes, vertical shear, and scattering of sunlight are also considered.

The competition between vertical transport of absorber due to the modal instability mechanism described above and that due to initial horizontal patchiness of an absorber injection is also examined. For patches with horizontal scales much larger than the deformation radius the modal form of absorber transport is shown to be important, while for smaller patch scales the nonmodal form dominates.

Thesis Supervisor: Peter H. Stone

Title: Professor of Meteorology

Contents

Acknowledgements

I would like to thank my thesis advisor, Professor Peter Stone, for his guidance and enduring patience during the course of my thesis program. His comments, as well as those by Professors Emanuel, Lindzen, and Lorenz and Dr. Rosen of my thesis committee led to significant generalizations of the original theory presented here.

I also wish to thank my colleagues at Livermore, especially Karl Taylor and Curt Covey for numerous engaging discussions, and Michael MacCracken for his enthusiastic support.

Keith Grant supplied the longwave radiation code used in the numerical simulations. Karl Taylor supplied the tracer advection subroutine. Curt Covey initiated the development of the solar radiation code and the application of the theory to the Martian atmosphere. Finally, Nancy Kliment and Floy Worden typed the manuscript with exceptional accuracy.

This work was performed under the auspices of the U.S. Department of Energy by the Lawrence Livermore National Laboratory under Contract No. W-7405-Eng-48.

1. Introduction

An outstanding feature of the terrestrial and Martian atmospheres is their near-transparency with respect to solar radiation. Although terrestrial water clouds scatter a significant fraction of the incoming solar radiation, and ozone absorbs much of the ultraviolet radiation, most absorption of visible radiation normally occurs at the surface. Radiative heating rates throughout most of the troposphere are dominated instead by infrared radiative cooling.

In the Martian atmosphere this situation is occasionally disrupted by global-scale dust storms, which increase the solar opacity of the atmosphere, leading to substantial tropospheric warming. Although such global storms fortunately do not develop in the terrestrial atmosphere, recent numerical simulations (Malone et al., 1986) involving the terrestrial atmospheric response to massive injections of absorptive smoke produced by hypothetical post-nuclear war fires have exhibited a similar phenomenon. Substantial lofting of the smoke is found to occur in these simulations, suggesting that the feedback between shortwave radiative heating and the dynamical response to the heating can be important. In the case of Martian dust storms, it has been suggested (Gierasch and Goody, 1973) that the phenomenon is similar to a terrestrial hurricane, with dust playing the role of water vapor lifted from the surface by the intense surface winds and transported to an inner core where heating (latent in the case of hurricanes, radiative in the case of dust storms) drives the circulation. There is, however, an important distinction between terrestrial and dusty hurricanes: whereas the radiative heating of dusty hurricanes is limited by the available insolation, the latent heating of terrestrial hurricanes is limited only by the efficiency with which water vapor can be transported to the hurricane core.

The interaction between radiative heating, the dynamical circulation, and an absorber distribution has been investigated in several previous analytical studies. Lindzen (1966a,b) and Leovy (1966) examined the interaction between ozone and photochemical, shortwave radiative, and dynamical processes in the stratosphere and mesosphere. Gierasch et al. (1973) proposed an instability mechanism involving clouds, longwave radiation, and the dynamical circulation. Houben (1981) considered the interaction of Martian dust, solar radiation, and tidal circulations.

While these previous works represent important contributions to the specific problems that they address, there exists as yet no general theory of unstable radiative-dynamical interactions. The work of Lindzen (1966a,b) and Leovy (1966) specifically includes photochemical processes that, though important for ozone, do not apply to most aerosols. The theory developed by Geirasch et al. (1973) is restricted to constituents that are important only for infrared radiation. Leovy et al. (1973), Leovy and Zurek (1979), and Schneider (1983) discuss mechanisms for the interaction of solar heating and transport of dust, but never explicitly represent the dust transport. Houben (1981) treats dust transport, but only horizontally. Haberle et al. (1982), Haberle et al. (1985), and Malone et al. (1986) treat the vertical transport of the absorber, but resort to numerical means to do so. What is clearly needed for Martian dust, post-nuclear war smoke, stratospheric ozone, volcanic aerosols, and any other shortwave radiative absorber is a general theory for the unstable interaction between the absorber and the dynamical circulation. The development of such a theory shall be the topic of this dissertation.

As in other instability theories, only modal (i.e., exponentially amplifying) instabilities shall be considered in the theory. Thus, lofting of the absorber due simply to an initial horizontal inhomogeneity in its distribution will be excluded from the initial analysis. While such nonmodal lofting may be important for both Martian dust storms and smoke lofting, it is not as amenable to analysis as is

the modal instability. The obvious question of which form of lofting, modal or nonmodal, is more important shall be addressed in numerical simulations.

For clarity the theory is developed under a variety of simplifying approximations. However, the general procedure is the same in each case. In particular, the radiative heating is first expressed in terms of an absorber mixing ratio. The equations governing conservation of mass, momentum, potential temperature and absorber mixing ratio are then linearized about a horizontally uniform basic state. The linear system of equations is then reduced to a single partial differential equation (PDE). By expressing solutions in terms of orthogonal basis functions with a time dependence given by $\exp(-i\sigma t)$, the PDE reduces to an algebraic equation for σ. Solutions are unstable if $Im(\sigma) > 0$.

An important parameter that emerges from the analysis is the rate of radiative-dynamical feedback, defined as

$$\alpha \equiv -\frac{RS_0 a\overline{T}}{c_p N^2 H}\,\frac{\partial \overline{q}}{\partial z} \tag{1.1}$$

where S_0 is the solar constant, $\overline{q}$ is the basic state absorber mass mixing ratio, a is the specific absorption coefficient for the absorber, and

$$\overline{T}(z) = \exp\left(-\frac{1}{\mu}\int_z^\infty a\rho_0\overline{q}dz'\right) \tag{1.2}$$

is the basic state transmissivity between the top of the atmosphere and level z. The remaining symbols take their standard meteorological meaning, as defined in Appendix A. One interpretation of α is that α^{-1} represents the time scale in which perturbations in absorber mixing ratio, through vertical advection induced by radiative heating, feed back upon themselves. In many instances the growth rate of unstable disturbances is, in the absence of dissipation, proportional to α; in most cases the growth rate does not exceed the feedback rate. Thus, the radiative-dynamical feedback rate characterizes the growth rate. By determining limits to the feedback rate, we can place an upper bounds on the growth rate.

For example, if we assume that $\overline{q}(z)$ decreases exponentially with scale height h, then for grey absorption

$$a\,\frac{\partial \overline{q}}{\partial z} = -a\overline{q}/h = -\frac{\tau_a}{\rho_0}\frac{H+h}{Hh^2} \tag{1.3}$$

where

$$\tau_a(z) = \int_z^\infty a\rho_0\overline{q}dz' \tag{1.4}$$

is the absorption optical depth from the top of the atmosphere to level z. The feedback rate then becomes

$$\alpha = \alpha_0\,\frac{H}{h}\,\left(1+\frac{H}{h}\right)\,\tau_a\,\exp\left(-\frac{\tau_a}{\mu}\right) \tag{1.5}$$

where

$$\alpha_0 = \frac{RS_0}{c_p\rho_0 N^2 H^3} \simeq 4\times 10^{-6}\mathrm{s}^{-1} \tag{1.6}$$

for $\rho_0 = 1$ kg m^{-3}, $S_0 = 1360$ Wm^{-2}, $N = 10^{-2}$s^{-1}, and $H = 10$ km. At sufficiently high altitudes, where $\tau_a \ll \mu$, the transmissivity is near unity but the absorber gradient is small, so the feedback rate is small. In optically thick atmospheres ($\tau_a \gg 1$), the absorber gradient is large near the surface but the transmissivity is small, so the feedback rate is again small. However, at the altitude for which $\tau_a = \mu$ the feedback rate for a given $\overline{q}(z)$ is a maximum, given by

$$\alpha_{\max} = 0.37\;\alpha_0\;\mu\frac{H}{h}\left(1+\frac{H}{h}\right) \quad . \tag{1.7}$$

For $\mu = 1$ (i.e., summertime at local noon), maximum values are

$$\alpha_{\max} = \begin{cases} (4\text{ days})^{-1} & \text{for } h = H = 10\text{ km} \\ (1.7\text{ hrs})^{-1} & \text{for } h = H/10 = 1\text{ km} \end{cases} \quad . \tag{1.8}$$

Thus, if the absorption optical depth exceeds unity and the vertical gradient of absorber mixing ratio is large enough, the radiative-dynamical feedback rate in the summer hemisphere (i.e., when solar radiation is strong) can be quite strong.

Growth rates of unstable modes can be competitive with those associated with baroclinic instability.

The physical mechanism for the instability depends on whether the basic state absorber mixing ratio increases or decreases with altitude. If the basic state absorber mixing ratio decreases with altitude, then upward motion increases the local absorber concentration. Assuming radiative heating increases with increasing local absorber concentration, the upward motion increases the radiative heating, leading to warming. If the perturbation is to amplify, warm temperatures must be positively correlated with the upward motion. To maximize the conversion of potential energy to kinetic energy, warm temperatures should be perfectly correlated with the upward motion. In this instance, this occurs if the frequency of oscillation is much less than the growth rate. As illustrated in Figure 1.1, upward motion, high absorber concentration, radiative heating, and warm temperatures all coincide. This unstable mode we shall term the advective mode, since propagation for this mode is weak; indeed, the mode does not propagate at all in the limit of zero radiative-dynamical feedback.

If, on the other hand, the basic state absorber mixing ratio increases with altitude, then the advective mode is damped. However, as we shall demonstrate, propagating Rossby and inertia-gravity waves can amplify. If the frequency of oscillation is much larger than the growth rate, then high absorber concentrations, and hence strong radiative heating, lags downward motion by one quarter cycle, and lead warm temperatures by one quarter cyle. Thus, warm temperatures are again positively correlated with upward motion. Potential energy is converted to kinetic energy, and the perturbation amplifies. This mechanism was first described by Leovy (1966). Figure 1.1 also illustrates the phase relation for this type of instability, which we shall term a propagating instability because it relies on propagation for the proper phase relation of heating, temperature, and vertical motion.

Note that the growth rate for the propagating instability must be much less than the frequency of oscillation, a significant constraint for slowly propagating waves when the radiative-dynamical feedback rate is strong.

The remainder of this thesis shall describe various aspects of the radiative-dynamical interaction in considerably greater detail. Chapter 2 discusses the representation of the radiative heating in terms of the absorber mixing ratio. In Chapter 3 the theory is developed using the quasi-geostrophic approximation; the theory is generalized to the primitive equations on an f-plane and on a β-plane in Chapter 4. Chapter 5 addresses the effect of mechanical, thermal, and absorber damping processes on the instability. Chapter 6 considers the importance of the constraint that the feedback rate be uniform, and the effect of removing that constraint. The effect of vertical shear in the basic state zonal wind is addressed in Chapter 7, and the effect of scattering is treated in Chapter 8.

The development of the theory of radiative-dynamical interaction in Chapters 2–8 is intentionally general, with few references to specific examples of physical phenomena. This approach is taken to permit the exploration of a wide range of values in parameter space, and hence broaden our understanding of the radiative-dynamical interaction. Indeed, numerous surprising aspects of the interaction are discovered which might have been overlooked in a more specialized investigation.

In Chapter 9 the theory is applied to a specific problem, namely that of smoke lofting following a nuclear war. The particular issue addressed in Chapter 9 is the question of whether nonmodal forms of lofting associated with the initial patchiness of the smoke concentration might dominate the modal form of lofting predicted by the theory. In Chapter 10 nonhydrostatic interactions are considered by applying solar heating to the Morton-Taylor-Turner theory of thermal convection. Application of the hydrostatic instability theory to planetary atmospheres is addressed in Chapter 11. Finally, a summary of the dissertation is presented in Chapter 12.

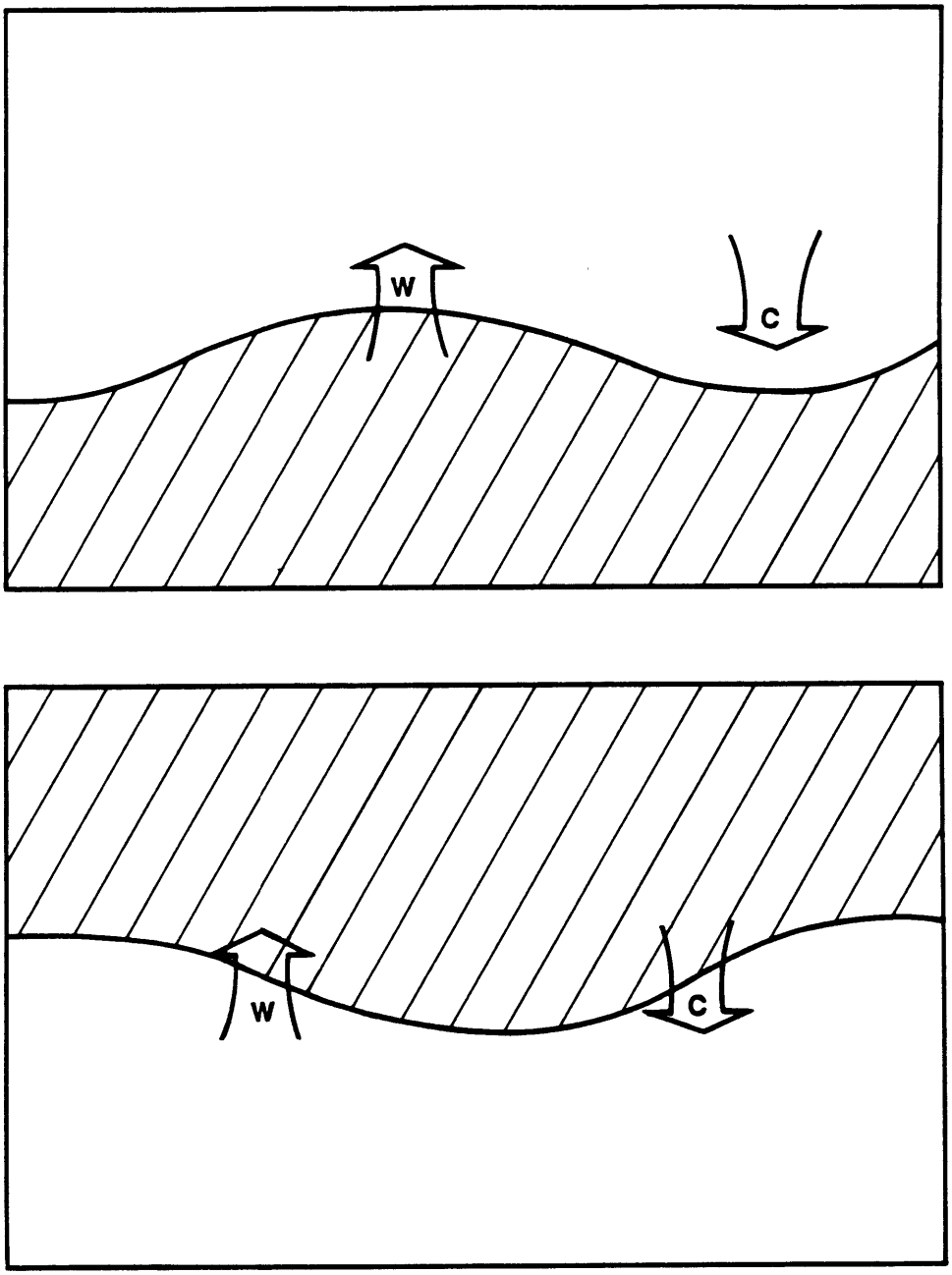

Figure 1.1. Schematic structure of advective mode (top) and propagating mode (bottom) of radiative-dynamical instability. In the propagating mode, phase propagation is from left to right.

2. Parameterization of Radiative Heating

As stated in Chapter 1, the first step in developing a theory of radiative-dynamical instability is to express the shortwave radiative heating in terms of the absorber distribution. Here we do so under the assumption that scattering can be neglected and that absorption is grey (i.e., independent of wavelength in the solar spectrum). Although the first assumption is not strictly true for most aerosols, calculations discussed in Chapter 8 demonstrate little sensitivity to the fraction of sunlight scattered. The grey approximation is reasonable for many aerosols but is inaccurate for most gaseous absorbers. However, we suggest a manner in which nongrey effects can be treated.

In the absence of scattering, the shortwave radiative heating at a level z can be expressed, under the grey approximation, as

$$Q(z) = -\frac{\partial F}{\partial z} = \mu S_0 \frac{\partial}{\partial z} \exp\left(-\frac{1}{\mu}\int_z^\infty a\rho_0 q dz'\right) = S_0 a \rho_0 q(z) T(z) \tag{2.1}$$

where S_0 is the solar constant, μ is the cosine of the solar zenith angle, a is the specific absorption coefficient, q is the absorber mass mixing ratio, and

$$T(z) = \exp\left(-\frac{1}{\mu}\int_z^\infty a\rho_0 q dz'\right) \tag{2.2}$$

is the atmospheric transmissivity. For small perturbations about a stratified $\overline{q}(z)$,

$$Q' \simeq S_0 a \rho_0 \left(\overline{T} q' + \overline{q} T'\right) \tag{2.3}$$

unless $\mu < 0$, in which case $Q' = 0$.

The first term in (2.3) represents the dependence of the local perturbation heating rate on the local perturbation absorber concentration. The second term represents the dependence of the heating on the absorption above the reference level. If, for example, an absorber perturbation has a sufficiently deep vertical distribution, the reduction in the transmissivity due to high absorber concentrations

aloft can reduce or even dominate the enhanced heating associated with high local absorber concentrations. The second term, then, is potentially important and hence should be treated.

To do so, and to determine the conditions under which perturbations in transmissivity are important, we shall assume that the perturbation absorber mixing ratio is, after scaling for density variations with height, oscillatory in the vertical,

$$q' = q_0 \exp\left(\frac{z}{2H} + imz\right) \quad . \tag{2.4}$$

Such a distribution is justified if the coefficients of the problem are constant, permitting plane-wave solutions. If the coefficients are not constant, then numerical methods are required both to express the heating in terms of the absorber distribution, and to solve the eigenvalue problem. For the present we shall assume that the coefficients of the problem are uniform, so that (2.4) is justified. The treatment of cases in which the coefficients vary with altitude is deferred until Chapter 6.

Given (2.4), the perturbation transmissivity

$$T' = \overline{T}\left[\exp\left(-\frac{1}{\mu}\int_z^\infty a\rho_0 q' dz'\right) - 1\right] \simeq -\frac{1}{\mu}\,\overline{T}\int_z^\infty a\rho_0 q' dz' \tag{2.5}$$

can be expressed, assuming a constant density scale height H,

$$T' \simeq -\overline{T}\,\frac{a\rho_0 q'}{\mu}\,\frac{2H}{1 - 2\,imH} \quad . \tag{2.6}$$

Then (2.3) becomes

$$Q' = S_0 a\rho_0\,\overline{T}\left(1 - \frac{2\tau_H}{1 - 2imH}\right)\,q' \tag{2.7}$$

where

$$\tau_H \equiv \frac{Ha\rho_0\overline{q}}{\mu} \tag{2.8}$$

can be interpreted as the absorption optical depth experienced by a beam of sunlight directed at the solar zenith angle from the top of the atmosphere to the reference level, assuming uniform $\overline{q}$.

If τ_H or

$$\tau_m \equiv \frac{a\rho_0\overline{q}}{\mu m} \tag{2.9}$$

is small, then perturbations in the transmissivity can be neglected, so that (2.7) reduces to

$$Q' = S_0 a \rho_0 \overline{T} q' \quad . \tag{2.10}$$

Here τ_m can be interpreted as the absorption optical depth experienced by the direct solar beam through one vertical wavelength, assuming uniform absorber density.

If, on the other hand, τ_H and τ_m are both large, then perturbations in transmissivity are important. In this case, the perturbation heating for deep perturbations ($2mH \ll 1$) becomes

$$Q' \simeq -2 S_0 a \rho_0 \overline{T} \tau_H q' \quad . \tag{2.11}$$

The perturbation heating is now negatively correlated with the perturbation absorber concentration. While this case is not necessarily an unlikely one, we shall find that radiative-dynamical instabilities are possible independent of the sign of the correlation between radiative heating and absorber concentration. Moreover, the basic state transmissivity for such large optical depths is small, so less sunlight is available to drive the radiative-dynamical interaction.

If τ_H and τ_m are large but perturbations are shallow ($2\ mH \gg 1$), the perturbation heating becomes

$$Q' \simeq -i S_0 a \rho_0 \overline{T} \tau_m q' \quad . \tag{2.12}$$

In this case the perturbation heating and absorber concentration are 90° out of phase, with the heating leading the absorber concentration for upward-propagating waves, and lagging the absorber concentration for downward-propagating waves. As we shall see in Chapter 4, this phase shift can reduce or in some cases increase the growth rate of the radiative-dynamical instability.

The grey approximation, based on the assumption that the specific absorption coefficient is independent of wavelength, and hence of optical depth, is a reasonable approximation for aerosols, which are typically as large as or larger than wavelengths of most solar radiation. However, for gaseous absorption the grey approximation is generally not valid. A more general treatment is therefore required.

For nongrey absorption, the shortwave radiative heating is, in the absence of scattering, given by

$$Q(z) = \rho_0 q \int_0^\infty a(\lambda) S(\lambda) T(z, \lambda, \mu) d\lambda = S_0 a_0 \rho_0 T_0 q \tag{2.13}$$

where

$$S_0 = \int_0^\infty S(\lambda) d\lambda \tag{2.14}$$

$$T_0(z, \mu) = \frac{1}{S_0} \int_0^\infty S(\lambda) T(z, \lambda, \mu) d\lambda \tag{2.15}$$

$$a_0(z, \mu) = \frac{1}{S_0 T_0} \int_0^\infty a(\lambda) S(\lambda) T(z, \lambda, \mu) d\lambda \quad . \tag{2.16}$$

An accurate treatment of scattering of sunlight is too complicated for analytical techniques. However, a numerical treatment is possible within the context of linear theory. If $\mathbf{q}$ represents a vector of absorber mixing ratio at a discrete set of levels, the perturbation heating can be expressed

$$\mathbf{Q}' = \mathbf{J}\mathbf{q}' \tag{2.17}$$

where

$$J_{ij} = \frac{\partial Q_i}{\partial q_j} \ (\mathbf{q} = \overline{\mathbf{q}}) \tag{2.18}$$

is the Jacobian of the heating with respect to the absorber mixing ratio, evaluated at the basic state absorber concentration. In practice, $\mathbf{J}$ is evaluated numerically from the difference between the heating rate for the basic state absorber distribution, and the heating rate for the basic state absorber distribution plus a small

perturbation in layer j. Note that perturbations in the transmissivity can be neglected if the off-diagonal elements of **J** are set to zero. The treatment of the effects of scattering on the radiative-dynamical interaction is discussed in Chapter 8.

Finally, infrared radiative heating can be treated in a similar manner as for scattering. In this case a Jacobian of the heating with respect to temperature is required. In addition, if the shortwave absorber also emits longwave radiation, a Jacobian of longwave heating with respect to the absorber mixing ratio would also be required. The numerical implementation of this technique presents serious difficulties, however, as discussed in Chapter 8.

3. Quasi-Geostrophic Stability Analysis

The essential aspects of the radiative-dynamical instability can be demonstrated most easily within the context of the quasi-geostrophic theory. In this chapter we present an illustrative solution of the instability, or eigenvalue, problem under a number of somewhat restrictive assumptions. These include, in addition to the quasi-geostrophic approximation, the assumption of no vertical shear in the basic state flow, no dissipation (or, at least, the same uniform damping rate for all dependent variables), and uniform Brünt-Vaisala frequency and radiative-dynamical feedback rate. These assumptions will be relaxed in subsequent chapters.

Consider the linearized quasi-geostrophic equations governing the conservation of vorticity ζ, and potential temperature θ, which for log-pressure coordinates can be written

$$D\zeta + \beta v = f_0 \frac{1}{\rho_0}\frac{\partial}{\partial z}(\rho_0 w) \tag{3.1}$$

$$D\theta = -\frac{\partial \overline{\theta}}{\partial z} w + Q/(Ec_p\rho_0) \tag{3.2}$$

where

$$D = \frac{\partial}{\partial t} + \overline{u}\frac{\partial}{\partial x} + \epsilon \tag{3.3}$$

is the linearized advection and damping operator, and $E = (p/p_0)^\kappa$ is the Exner function. The remaining symbols are defined in Appendix A.

In quasi-geostrophic theory, the horizontal velocity can be expressed in terms of a streamfunction ψ,

$$v = \frac{\partial \psi}{\partial x} \tag{3.4}$$

$$\zeta = \nabla^2\psi \tag{3.5}$$

and the potential temperature follows from the hydrostatic relation

$$\theta = \frac{f_0 H}{RE}\frac{\partial \psi}{\partial z} \quad . \tag{3.6}$$

Substituting (3.4)–(3.6) into (3.1)–(3.2), the conservation equations for vorticity and potential temperature become

$$\left(D\nabla^2 + \beta \frac{\partial}{\partial x}\right)\psi = f_0 \frac{1}{\rho_0}\frac{\partial}{\partial z}(\rho_0 w) \tag{3.7}$$

$$f_0 D\frac{\partial \psi}{\partial z} = -N^2 w + RQ/(c_p \rho_0 H) \quad . \tag{3.8}$$

Solving (3.7) and (3.8) for the vertical velocity w yields the Rossby wave equation

$$f_0^2 \frac{\partial}{\partial z}\frac{1}{\rho_0}\frac{\partial}{\partial z}(\rho_0 D w) + \left(D\nabla^2 + \beta \frac{\partial}{\partial x}\right)\left[N^2 w - RQ/(c_p \rho_0 H)\right] = 0 \tag{3.9}$$

where we have assumed $\overline{u}$ and hence D does not vary with altitude (we shall relax this constraint in Chapter 7).

The feedback between the radiative heating Q and the dynamical circulation w is treated by expressing the heating in terms of a shortwave radiative absorber mixing ratio q and then relating the absorber concentration to the circulation. Combining (2.7) and (3.9), the Rossby wave equation then becomes

$$f_0^2 \frac{\partial}{\partial z}\frac{1}{\rho_0}\frac{\partial}{\partial z}(\rho_0 D w) + \left(D\nabla^2 + \beta\frac{\partial}{\partial x}\right)\left[N^2 w - \frac{RS_0 a\overline{T}}{c_p H}\left(1 - \frac{2\tau_H}{1 - 2\,imH}\right) q'\right] = 0 \quad . \tag{3.10}$$

The linearized equation governing conservation of absorber can be similarly expressed

$$Dq' = -\frac{\partial \overline{q}}{\partial z} w \quad . \tag{3.11}$$

Eliminating q' between (3.10) and (3.11) yields the PDE

$$\frac{f_0^2}{N^2}\frac{\partial}{\partial z}\frac{1}{\rho_0}\frac{\partial}{\partial z}(\rho_0 D^2 w) + (D\nabla^2 + \beta\frac{\partial}{\partial x})(D - \alpha_e)w = 0 \tag{3.12}$$

where

$$\alpha_e \equiv \alpha\left(1 - \frac{2\tau_H}{1 - 2\,imH}\right) \tag{3.13a}$$

represents the effective rate of radiative-dynamical interaction, with

$$\alpha \equiv -\frac{RS_0 a\overline{T}}{c_p N^2 H}\frac{\partial \overline{q}}{\partial z} \tag{3.13b}$$

defined to be the rate of radiative-dynamical interaction in the absence of perturbations in transmissivity. As we shall see, the magnitude of α_e characterizes the growth rate of unstable solutions of (3.12).

If $\tau_H = 0$ then α_e is pure real, with positive α_e corresponding to absorber mixing ratio decreasing with height, and negative α corresponding to absorber mixing ratio increasing with height. This particular sign convention was chosen with absorber lofting, which occurs for positive α_e, in mind. In fact, we shall soon find that unstable modes exist for both positive and negative α_e.

If τ_H is large and perturbations are deep ($2mH \ll 1$), then α_e is again pure real, but with positive (negative) α corresponding to absorber mixing ratio increasing (decreasing) with height.

If τ_H is large and perturbations are sufficiently shallow that $2mH \gg 1$ yet sufficiently deep that $\tau_m = \tau_H/(mH)$ is also large, then α_e is complex, thus altering both the propagation characteristics and, as we shall see in Chapter 4, the growth rate of solutions.

We shall now assume that the coefficients of (3.12) are constant (density is assumed to vary with a constant scale height H). This permits plane-wave solutions, which greatly simplifies the analysis, and justifies the use of (2.7) to represent the heating. While such an assumption is common and often justifiable for the Brünt-Vaisala frequency, it is not necessarily reasonable for the effective radiative-dynamical feedback rate α_e. The conditions under which such an assumption is reasonable, and the effects of treating variations in the feedback rate, are discussed in Chapter 6.

Assuming N^2 and α_e are independent of height, normal mode solutions of the form

$$w(x,y,z,t) = w_0 \exp(z/2H) \exp[i(kx + \ell y + mz - \sigma t)] \qquad (3.14)$$

yield the algebraic relation

$$\frac{f_0^2}{N^2} n^2 D^2 + (k_2^2 D - ik\beta)(D - \alpha_e) = 0 \tag{3.15}$$

where

$$n^2 = m^2 + \frac{1}{4H^2} \tag{3.16}$$

$$k_2^2 = k^2 + \ell^2 \quad . \tag{3.17}$$

Solutions satisfying the proper boundary conditions are unstable provided $Im(\sigma) > 0$. Because

$$D = -i\sigma + \overline{u}ik + \epsilon \tag{3.18}$$

for such waves, this is equivalent to the condition that the real part of D exceeds ϵ.

We shall now consider solutions to (3.15). Although the solutions can be expressed analytically, the expressions are complicated and not particularly meaningful. We shall instead consider several limiting cases, each of which assumes $\tau_H = 0$ and hence $\alpha_e = \alpha$ (cases for which $\tau_H \neq 0$ are considered in Chapter 4). The feedback parameter α_e is therefore pure real, with positive (negative) α_e corresponding to absorber mixing ratio decreasing (increasing) with height.

In the first case the magnitude of the feedback rate is much less than the frequency of internal Rosssby waves, i.e.,

$$|\alpha| \ll k\beta/k_3^2 \tag{3.19}$$

where

$$k_3^2 = k_2^2 + \frac{f_0^2}{N^2}\, n^2 \quad . \tag{3.20}$$

Approximate solutions of (3.15) are

$$D \simeq \frac{i\beta k}{k_3^2} - \alpha \frac{f^2 n^2}{N^2 k_3^2} \quad , \quad \alpha - \frac{i\alpha^2 k_3^2}{\beta k} \frac{f^2 n^2}{N^2 k_3^2} \quad . \tag{3.21}$$

The first solution corresponds to an internal Rossby wave which propagates westward with respect to the mean flow but, in the absence of radiative-dynamical feedback ($\alpha = 0$), does not amplify. The second solution corresponds to the advective mode which, in the absence of feedback, neither propagates nor grows. If $S_0 a\overline{T} \neq 0$ but $\overline{q}_z = 0$, the two solutions correspond to (a) the absorber being simply advected by the mean flow, forcing vertical motion through radiative heating, and driving a circulation through vortex stretching, and (b) no absorber perturbation, with Rossby waves propagating freely; if, on the other hand, $\overline{q}_z \neq 0$ but $S_0 a\overline{T} = 0$, the solutions correspond to (a) Rossby waves propagating freely, advecting the absorber, and (b) the absorber simply advected by the mean flow, with no perturbation circulation.

In the presence of positive radiative-dynamical feedback ($\alpha > 0$, i.e., absorber mixing ratio decreasing with altitude), the Rossby mode is damped but the advective mode will, in the absence of dissipation, amplify. In the absence of dissipative effects, the growth rate of the advective mode is approximately equal to the feedback rate (note that the growth rate is not identically equal to the feedback rate, for (3.15) could only be satisfied in such a case if $n = 0$, which requires that $w = 0$ to satisfy the boundary conditions, but also prevents the physical mechanism, vertical absorber transport, from operating). Because $\alpha \ll k\beta/k_3^2$ for this case and $f^2 n^2 < N^2 k_3^2$ in general, the growth rate of the advective mode dominates the frequency of oscillation (which, incidently, indicates eastward propagation). Thus, the perturbation heating and vertical velocity are in phase, with upward motion coinciding with high absorber concentrations and temperatures.

In the presence of negative radiative-dynamical feedback ($\alpha < 0$, i.e., absorber mixing ratio increasing with height), the advective mode is damped but the Rossby mode is unstable. For perturbations that are short and deep (i.e., $f^2 n^2 \ll N^2 k_2^2$)

the growth rate of the Rossby mode increases with the horizontal scale and decreases with the vertical scale. Thus, for perturbations that are long and shallow, the growth rate is approximately equal to the feedback rate. Because $f^2n^2 < N^2k_3^2$ for all perturbations, the growth rate of the Rossby mode is always less than the feedback rate, which for this case is also much less than the Rossby wave frequency. Thus, the unstable Rossby mode is qualitatively different from the unstable advective mode. Although the perturbation vertical velocity and temperature are in phase for both the unstable advective mode and the unstable Rossby mode, the perturbation heating and vertical velocity are in phase for the advective mode but they are nearly 90° out of phase for the Rossby mode. In terms of energetics, both unstable modes amplify by generating available potential energy (APE) through radiative heating (i.e., $\overline{Q'\theta'} > 0$) and then converting the APE to kinetic energy (i.e., $\overline{w'\theta'} > 0$), but the energy generation process is less efficient for the Rossby mode because the phase difference between the heating and temperature is nearly 90°.

For both positive and negative radiative-dynamical feedback the unstable mode transports the absorber down the gradient of mean absorber mixing ratio, i.e., from the absorber balance the vertical transport

$$\overline{w'q'} = Re\left(-\frac{1}{D}\right)\frac{\partial \overline{q}}{\partial z}\,|w|^2 = -\frac{D_r}{D_r^2 + D_i^2}\,\frac{\partial \overline{q}}{\partial z}\,|w|^2 \tag{3.22}$$

is upward (downward) if the mean absorber mixing ratio decreases (increases) with altitude. Thus, the unstable modes reduce the magnitude of the absorber gradient, and hence reduce the instability of the radiative-dynamical system. The unstable modes will continue to disperse the absorber distribution until the feedback mechanism is too weak to overcome the dissipative processes. Given (3.22) and simple (or the more accurate general analytical) solutions such as (3.20) for the growth

rate and frequency, it may be possible to develop parameterizations for the absorber transport in terms of the basic state variables. However, a plausible closure assumption for the perturbation amplitude $|w|^2$, and a scale selection criterion, are required.

In the second limiting case the magnitude of the feedback rate is much greater than the internal Rossby wave frequency but is much less than another limit:

$$\frac{\beta k}{k_3^2} \ll |\alpha| \ll \frac{\beta k}{k_2^2} \frac{k_3^2}{k_2^2} \quad . \tag{3.23}$$

This case only holds for waves that are long and shallow, i.e., $f^2 n^2 \gg N^2 k_2^2$. Approximate solutions are

$$D \simeq (i-1)\alpha \left(\frac{\beta k}{2\alpha k_3^2}\right)^{1/2}, \; (1-i)\,\alpha \left(\frac{\beta k}{2\alpha k_3^2}\right)^{1/2} \quad . \tag{3.24}$$

The first solution corresponds to the Rossby mode, while the second solution represents the advective mode.

In the presence of positive radiative-dynamical feedback ($\alpha > 0$), the advective mode is again unstable, and the Rossby mode is damped by the feedback. Because the feedback rate is much larger than the internal Rossby wave frequency for this case, the growth rate of the advective mode is much smaller than the feedback rate. Although the growth rate still increases with the feedback rate, it increases more slowly than in the previous limit. The growth rate now depends on the scale of the perturbation, increasing with increasing vertical and meridional scale, and increasing with decreasing zonal scale if the zonal scale is long. In contrast to the previous limit, the growth rate of the advective mode is equal to, rather than much greater than, the oscillation frequency. Propagation is again eastward with respect to the mean flow.

The Rossby mode is strongly affected by the radiative-dynamical feedback for this case. The oscillation frequency is increased substantially. For positive

radiative-dynamical feedback, the damping rate equals the oscillation frequency. For negative feedback (absorber increasing with altitude), the growth rate equals the oscillation frequency and, for the same feedback magnitude, the growth rate of the unstable advective mode. In contrast to the previous limit, the growth rate increases rather than decreases with the vertical scale and, for waves with long zonal scales, decreases rather than increases with increasing zonal scale. Thus, the growth rate is largest for certain vertical and zonal scales. This aspect of the unstable Rossby mode will be more fully explored in Chapter 4.

In the third limiting case we assume that

$$\frac{\beta k}{k_2^2}\,\frac{k_3^2}{k_2^2} \ll |\alpha| \ll f \quad . \tag{3.25}$$

The upper bound follows from subsequent consideration of the primitive equations in Chapter 4. Note that implicit in (3.25) is the assumption that the Coriolis frequency exceeds the Rossby wave frequency. While this is true for synoptic scale waves in mid-latitudes, it is not true for planetary waves in mid-latitudes or for all waves near the equator. Thus, the present case is restricted to sub-planetary scales in mid-latitudes. Approximate solutions of (3.15) for this case are

$$D \simeq \frac{i\beta k}{k_2^2} - \frac{\beta^2 k^2}{\alpha}\,\frac{f^2 n^2}{N^2 k_2^6} \quad , \quad \frac{\alpha k_2^2}{k_3^2} - \frac{i\beta k}{k_3^2}\,\frac{f^2 n^2}{N^2 k_2^2} \quad . \tag{3.26}$$

In the presence of positive radiative-dynamical feedback ($\alpha > 0$), the advective mode is again unstable, but with the growth rate somewhat less than the feedback rate. The growth rate increases with decreasing horizontal scale and increasing vertical scale. In particular, the growth rate is largest for waves with horizontal scales much less than the internal deformation radius, i.e., for such that $k_2^2 \sim k_3^2 \gg f^2 n^2 / N^2$. For all perturbation scales that satisfy the condition (3.25), the growth rate of the advective mode again dominates the frequency of oscillation and, for the same feedback magnitude, the growth rate of the unstable Rossby mode.

In the presence of negative radiative-dynamical feedback ($\alpha < 0$), the Rossby mode is again unstable in the absence of dissipation. As in the case (3.19) with weak feedback, but in contrast to the case (3.23) with moderate feedback and shallow waves, the Rossby mode growth rate for the present case decreases with increasing vertical scale, provided the condition (3.25) is satisfied. As in the case (3.23) with moderate feedback, but in contrast to the case (3.19) with weak feedback, the growth rate of the Rossby mode for the present case (3.25) increases with increasing meridional scale but with decreasing zonal scale (unless the meridional scale is much longer than the zonal scale, in which case the growth rate increases with increasing zonal and meridional scale). This scale dependence is quite different from that of the unstable advective mode, with the growth rate of the Rossby mode either increasing or decreasing with zonal and vertical scales, depending on which of the limits (3.19), (3.23), and (3.25) are satisfied. In the transition between these limits we can expect to find maxima in the Rossby mode growth rate. This feature of the unstable Rossby mode is further addressed in Chapter 4. For all perturbation scales that satisfy (3.25), the growth rate of the Rossby mode is much less than both the feedback rate and the frequency (which, incidently, is increased as a result of the strong radiative-dynamical feedback), and actually decreases as the feedback rate increases in magnitude. This is in contrast to the cases with weak and moderate feedback, in which the growth rate increases with the magnitude of the feedback rate. Thus, for a given perturbation scale (k, l, m), the growth rate of the Rossby mode is largest for an intermediate feedback rate.

Although we cannot demonstrate it analytically, the feedback rate at which the Rossby mode growth rate is largest is found to be near the transition frequency between cases (3.23) and (3.25), i.e.,

$$\alpha_m \equiv -\frac{\beta k}{k_2^2}\,\frac{k_3^2}{k_2^2} \quad . \tag{3.27}$$

Because this feedback rate is not within the limits of the three cases considered by (3.19), (3.22) and (3.25), we cannot offer a simple expression for the maximum Rossby wave growth rate as a function of perturbation scale. However, the analytical solution, though complicated, is readily evaluated numerically. Before examining numerical solutions in the intermediate feedback range, we shall first extend the limits of the present theory to feedback rates exceeding the Coriolis frequency by considering the theory within the context of the primitive equations. However, before doing that, we shall first discuss the appropriate boundary conditions of the instability problem.

In addition to satisfying the dispersion relation (3.15), solutions must also satisfy the boundary conditions, which are

$$w(0) = 0$$

$$\rho_0 w\psi \text{ bounded as } z \to \infty \tag{3.28}$$

The lower boundary condition determines the vertical phase of solutions. For an atmosphere with a finite top, the upper boundary condition leads to the restriction that only a discrete set of vertical wavenumbers is permitted. For an infinite atmosphere, this quantization does not apply. However, downward energy propagation is permitted due to energy released by the instability at higher levels.

In summary, we have found through a number of simplifying approximations that unstable radiative-dynamical interactions are possible when absorber mixing ratio increases or decreases with height. The physical mechanisms for the instability in the two cases are quite different, but also exhibit some similarities. We have derived some approximate expressions for the complex eigenfrequencies in several special cases. These expressions are summarized in Table 3.1. The assumptions required for the analysis in this illustrative chapter are relaxed in the following chapters. Many of the basic conclusions of this chapter are, however, unaltered by the additional considerations.

Table 3.1. Approximate solutions for the complex eigenfrequency σ. Perturbations in transmissivity are neglected (i.e., $\tau_H = 0$).

Mode	Feedback Rate		
	$\lvert\alpha\rvert \ll \frac{\beta k}{k_3^2}$	$\ll \lvert\alpha\rvert \ll \frac{\beta k}{k_2^2}\frac{k_3^2}{k_2^2}$	$\ll \lvert\alpha\rvert$
Advective	$\frac{\alpha^2 k_3^2}{\beta k}\frac{f^2 n^2}{N^2 k_3^2} + i\alpha$	$(1+i)\alpha\left(\frac{\beta k}{2\alpha k_3^2}\right)^{1/2}$	$\frac{\beta k}{k_3^2}\frac{f^2 n^2}{N^2 k_2^2} + \frac{i\alpha k_2^2}{k_3^2}$
Rossby	$-\frac{\beta k}{k_3^2} - \frac{i\alpha f^2 n^2}{N^2 k_3^2}$	$-(1+i)\alpha\left(\frac{\beta k}{2\alpha k_3^2}\right)^{1/2}$	$-\frac{\beta k}{k_2^2} - \frac{i\beta^2 k^2}{\alpha}\frac{f^2 n^2}{N^2 k_2^6}$

4. Generalization to the Primitive Equations

The theory developed so far has been restricted by the quasi-geostrophic approximation, which filters out the inertia-gravity modes. Moreover, the quasi-geostrophic solution of the advective mode is inaccurate when the rate of radiative-dynamical feedback exceeds the Coriolis frequency. To apply the theory to the inertia-gravity modes, and to cases in which the feedback rate exceeds the Coriolis frequency, the theory must be extended to the primitive equations. In addition, nonzero values of the parameter τ_H shall be considered in this chapter.

Linearizing about a horizontally uniform basic state, the primitive equations in log-pressure coordinates can be written

$$Du - fv = -\frac{\partial \Phi}{\partial x} \tag{4.1}$$

$$Dv + fu = -\frac{\partial \Phi}{\partial y} \tag{4.2}$$

$$\frac{\partial u}{\partial x} + \frac{\partial v}{\partial y} + \frac{1}{\rho_0}\frac{\partial}{\partial z}(\rho_0 w) = 0 \tag{4.3}$$

$$D\frac{\partial \Phi}{\partial z} = -N^2 w + \frac{RQ}{c_p \rho_o H} \quad . \tag{4.4}$$

The solution on a β-plane is much more complicated than on an f-plane. Because inertia-gravity waves are insensitive to the β term, we shall first consider the solution for a midlatitude f-plane.

4.1. Midlatitude f-Plane

On an f-plane, the Coriolis parameter is assumed to be constant. Assuming the advective operator D is uniform, the primitive equations can then be reduced to a single partial differential equation for the vertical velocity,

$$(D^2 + f_0^2)D\frac{\partial}{\partial z}\frac{1}{\rho_0}\frac{\partial}{\partial z}(\rho_0 w) + D\nabla^2(N^2 w - \frac{RQ}{c_p \rho_0 H}) = 0 \quad . \tag{4.5}$$

This wave equation differs from the Rossby wave equation (3.9) because of the presence of the D^2 term and the absence of a β-term.

Combining (4.5) with the heating expression (2.7) and the absorber budget equation (3.11) yields

$$(D^2 + f_o^2)D\frac{\partial}{\partial z}\frac{1}{\rho_o}\frac{\partial}{\partial z}(\rho_o w) + N^2\nabla^2(D - \alpha_e)w = 0 \tag{4.6}$$

where the effective radiative-dynamical feedback rate α_e is defined by (3.13). Assuming N, α_e and the density scale height H are constant, normal mode solutions of the form (3.14) yield the algebraic relation

$$(D^2 + f_0^2)Dn^2 + N^2k_2^2(D - \alpha_e) = 0 \quad . \tag{4.7}$$

In the absence of radiative-dynamical feedback ($\alpha_e = 0$), solutions to (4.7) are

$$D = 0, \pm i\frac{Nk_3}{n} \tag{4.8}$$

which correspond to the advective and eastward- and westward-propagating inertia-gravity modes.

In the presence of feedback, solutions to (4.7) are more complicated. We shall therefore consider approximate solutions in some limiting cases, corresponding to whether the magnitude of the radiative-dynamical feedback rate is much greater than or much less than a scale-dependent parameter

$$\gamma \equiv \frac{2Nk_3^3}{3\sqrt{3}\, nk_2^2} \quad . \tag{4.9}$$

In all cases we shall assume $\tau_H = 0$, so that $\alpha_e = \alpha$ is pure real (cases with $\tau_H \neq 0$ are considered in Section 4.2). For waves that are either long and shallow ($f^2n^2 \gg N^2k_2^2$) or short and deep ($f^2n^2 \ll N^2k_2^2$), it can be shown that γ is much larger than the Coriolis frequency. For waves with an intermediate aspect ratio ($f^2n^2 = N^2k_2^2$) γ is of the same order as the Coriolis frequency. Thus, γ is larger than or of the same order as f for all wave scales.

In the first case, we assume weak radiative-dynamical feedback, i.e., $|\alpha| \ll \gamma$. If $|\alpha| \ll f$, this condition is assured for all waves scales. Then approximate solutions to (4.7) are

$$D \simeq \frac{\alpha k_2^2}{k_3^2} \quad , \quad \pm\frac{iNk_3}{n} - \frac{\alpha k_2^2}{2k_3^2} \quad . \tag{4.10}$$

In the presence of positive radiative-dynamical feedback ($\alpha > 0$, i.e., absorber mixing ratio decreasing with altitude), the two inertia-gravity modes are damped by the feedback, while the advective mode amplifies in the absence of dissipation. In fact, the expression for the growth rate of the advective mode agrees exactly with the approximate quasi-geostrophic solution when the feedback rate is much larger than the internal Rossby wave frequency. Thus, we conclude that the quasi-geostrophic solution is accurate for all scales if the feedback rate is less than the Coriolis frequency. Even for feedback rates greater than f, the quasi-geostrophic solution is accurate for waves that are sufficiently short and deep or sufficiently long and shallow that $|\alpha| \ll \gamma$. Note that the oscillation frequency of the advective mode vanishes for the present case because we have assumed an f-plane rather than a β-plane.

In the presence of negative radiative-dynamical feedback ($\alpha < 0$, i.e., absorber mixing ratio increasing with altitude), the advective mode is damped, while both inertia-gravity modes are unstable in the absence of dissipation. The scale-dependence of the growth rate of the unstable inertia-gravity modes is identical to that of the unstable advective mode, except that the growth rate of the inertia-gravity modes is one half that of the advective mode for the same feedback magnitude. As with the Rossby waves on the β-plane, the growth rate of the unstable inertia-gravity waves is much less than the frequency of oscillation. Thus, the inertia-gravity waves will have a phase structure similar to that of the unstable Rossby waves. Leovy (1966) first discussed the physical mechanism of this mode of instability, in the context of the photo-chemistry of oxygen in the lower mesosphere.

For strong radiative-dynamical feedback ($|\alpha| \gg \gamma$), approximate solutions to (4.7) are

$$D \simeq \alpha \left(\frac{N^2 k_2^2}{\alpha^2 n^2} \right)^{1/3} \quad , \quad -\alpha \, \frac{1 \pm i\sqrt{3}}{2} \left(\frac{N^2 k_2^2}{\alpha^2 n^2} \right)^{1/3} \quad . \tag{4.11}$$

In the presence of positive feedback ($\alpha > 0$), the advective mode is again non-propagating and, in the absence of dissipation, unstable. However, the growth rate increases much more slowly with increasing feedback. In particular, the growth rate is proportional to the feedback rate to the one-third power. Moreover, the scale dependence of the growth rate is different from the cases with weaker feedback. The growth rate increases with the vertical scale of the wave, even for waves that are short and deep, and decreases as the horizontal scale increases, even for waves that are long and shallow. For all waves scales for which $|\alpha| \gg \gamma$, however, the growth rate of the advective mode is much less than the feedback rate, and is less than the quasi-geostrophic solution.

In the presence of negative radiative-dynamical feedback ($\alpha < 0$), the inertia-gravity modes are again unstable in the absence of dissipation. The growth rate of the inertia-gravity modes is again equal to one-half that of the unstable advective mode for the same feedback magnitude. The frequency of oscillation of the inertia-gravity modes is greatly increased by the feedback, but is only slightly larger than the growth rate.

Table 4.1 summarizes the approximate expressions for the complex eigenfrequency derived here, along with those derived in Chapter 3.

4.2. β-plane

We have seen that for the advective mode the latitudinal variation of the Coriolis parameter must be accounted for if $|\alpha| \leq \beta k / k_3^2$. We have also seen that the primitive equations may be required if $|\alpha| \geq f$. If $f > \beta k / k_3^2$ then $|\alpha|$ cannot be

both less than $\beta k/k_3^2$ and greater than f, so that the previous analyses are sufficient to cover all possible feedback rates. However, if f $< |\alpha| < \beta k/k_3^2$ the foregoing analyses are inapplicable. In this case it is necessary to treat the primitive equations on a β-plane, if not a sphere. In midlatitudes, the condition $f < \beta k/k_3^2$ is met for the planetary scales (for which spherical geometry is required regardless of the feedback rate); in the subtropics and tropics, f may be less than $\beta k/k_3^2$ for a variety of spatial scales.

In this section we shall consider the radiative-dynamical feedback for the primitive equations on β-planes. Two cases will be considered, namely a midlatitude β-plane, for which $f < \beta k/k_3^2$ for the planetary scales, and an equatorial β-plane, for which $f < \beta k/k_3^2$ for all spatial scales.

In either case, accounting for the latitudinal variation of the Coriolis parameter greatly complicates the analysis. In the absence of radiative-dynamical feedback, the classical β-plane theory of waves (Lindzen, 1967) reduces the linearized primitive equations to a single equation for the meridional rather than vertical velocity; solutions for which $v = 0$ are treated separately. We shall take the same approach here. The resulting wave equation with radiative-dynamical feedback can be written

$$\left(D^2 + f^2\right) D^2 \frac{\partial}{\partial z} \frac{1}{\rho_0} \frac{\partial}{\partial z} (\rho_0 v) + N^2 \left(D\nabla^2 + \beta \frac{\partial}{\partial x}\right) (D - \alpha_e)\, v = 0 \quad . \qquad (4.12)$$

For the middle latitude case it is sufficient to treat f and β as constants in (4.12); this approximation is not reasonable for the equatorial β-plane. Because this distinction alters the analysis considerably, we shall consider the midlatitude and equatorial cases separately.

4.2.1. Mid-latitude β-plane

If f and β are treated as constants in (4.12), then the usual Fourier basis functions given by (3.14) are sufficient to reduce the problem to an algebraic equation,

namely,

$$\frac{n^2}{N^2} D^4 + k_3^2 D^2 - \left(\alpha_e k_2^2 + ik\beta\right) D + i\alpha_e k\beta = 0 \quad . \tag{4.13}$$

This quartic equation for D admits four solutions, corresponding to the advective mode, the Rossby mode, and two inertia-gravity modes. We have discussed these modes in the previous analyses of the quasi-geostrophic system on a mid-latitude β-plane, and the primitive equations on an f-plane. For synoptic and meso-scales in midlatitudes, those treatments covered all possible cases except for the inertia-gravity modes on a β-plane and the Rossby mode when the feedback rate exceeds the Coriolis frequency. Here we shall consider those cases and solutions when the feedback rate does not satisfy any of the special limiting cases. Although one can express exact solutions to (4.13) analytically, the expressions are not meaningful, and hence will not be presented. Rather, we shall present the analytical solutions graphically, thereby illustrating the parametric dependence of the growth rate for parameter ranges that do not admit simple solutions. First we shall consider cases with $\tau_H = 0 (\alpha_e = \alpha)$, and then cases $\tau_H \neq 0$.

The advective mode is unstable for positive radiative-dynamical feedback, i.e., absorber decreasing with altitude. Figure 4.1 shows the advective mode growth rate, normalized by the feedback rate, as a function of the feedback rate, for $\tau_H = 0$, zonal and meridional wavelengths of 1000 km, and a vertical wavelength of 10 km. Three different parameter regimes are evident in this figure. For feedback rates much smaller than the internal Rossby wave frequency (8×10^{-7} s^{-1} for the wave scale assumed in Figure 4.1), the growth rate is, consistent with (3.21), nearly equal to the feedback rate. For feedback rates much larger than the Rossby wave frequency but much smaller than the Coriolis frequency (10^{-4} s^{-1}), the growth rate is again approximately proportional to the feedback rate, but with the constant of proportionality less than one. Consistent with (3.26), the constant is k_2^2/k_3^2, or 0.67 for the wave scale assumed in Figure 4.1. For feedback rates much greater than the

Coriolis frequency, the growth rate increases more slowly than the feedback rate. In particular, according to (4.11), the growth rate increases with the feedback rate to the one-third power in this regime. Thus, the growth rate of the advective mode is always less than the feedback rate, and always increases as the feedback rate increases.

Figure 4.2 shows the advective mode growth rate as a function of vertical wavelength, for $\tau_H = 0$, a feedback rate of 10^{-5} s^{-1} (chosen to be competitive with baroclinic instability), and zonal and meridional wavelengths of 1000 km. For such a horizontal scale, the external Rossby wave frequency is 1.3×10^{-6} s^{-1}, much less than the assumed feedback rate, so that the deepest waves will satisfy the condition (3.25), while shallow waves will satisfy (3.23). Consistent with (3.24) and (3.26), the growth rate increases as the vertical scale increases, eventually reaching the feedback rate. Note that for deep waves the condition (3.23) cannot be satisfied, so that the growth rate is given by either (3.21), (3.26) or (4.10); in either case, the growth rate approaches the feedback rate as the waves become deeper.

Figure 4.3 shows the growth rate of the advective mode as a function of zonal wavelength, for $\tau_H = 0$, a feedback rate of 10^{-5} s^{-1}, a meridional wavelength of 10,000 km, and a vertical wavelength of 10 km. Consistent with (3.24) and (3.26), the growth rate decreases with increasing zonal scale. For very short zonal scales, condition (3.25) applies, so that by (3.26) the growth rate is approximately equal to the feedback rate when the zonal scale is much less than the internal deformation radius, i.e., when $k_2^2 \gg f_0^2 n^2 / N^2$. For the 10 km vertical wavelength, the internal deformation radius is 1000 km.

In summary, the growth rate of the advective mode is always less than the radiative-dynamical feedback rate. It increases with increasing feedback rate, increasing vertical scale, and decreasing meridional and zonal scale. Although Figures 4.2 and 4.3 consider only feedback rates less than the Coriolis frequency, (4.11) tells

us that the same qualitative scale dependence of the advective mode growth rate also holds for feedback rates larger than the Coriolis frequency.

According to (4.10) and (4.11), the growth rate of the inertia-gravity modes for negative radiative-dynamical feedback (absorber increasing with altitude) has the same scale dependence as that of the unstable advective mode, but with half the amplitude for the same feedback rate magnitude. However, the analysis leading to (4.10) and (4.11) is based on an f-plane. On a β-plane, we have seen that the β term enhances the growth rate of the advective mode when the feedback rate is less than the Rossby wave frequency. It remains to be seen whether the inertia-gravity modes are also affected by the β term. Figure 4.4 shows the gravity wave growth rate, normalized by the feedback rate, as a function of the feedback rate, for $\tau_H = 0$, zonal and meridional wavelengths of 1000 km, and a vertical wavelength of 10 km. For feedback rates much larger than the Coriolis frequency (10^{-4} s^{-1}), (4.11) applies, with the growth rate increasing with the cube root of the feedback rate. For feedback rates much less than the Coriolis frequency, (4.10) applies, with the growth rate proportional to the feedback rate, even for feedback rates much less than the Rossby wave frequency. Thus, the analysis of the inertia-gravity mode on the f-plane is a good approximation for all feedback rates. Because the growth rates of the gravity and advective modes have the same scale dependence, we need not discuss the scale dependence of the gravity modes, but refer the reader to the previous discussion of the advective mode.

Of the three modes of instability, the Rossby mode is the most complex and hence, interesting. The analysis of Chapter 3 considered a wide range in the feedback rate, from values much smaller than the Rossby wave frequency to values much larger, but was restricted by the quasi-geostrophic approximation. However, consistent with the fact that Rossby waves are low-frequency modes, the more

general primitive equation solution of (4.13) for the Rossby mode is virtually identical to the quasi-geostrophic solution. Thus, the approximate solutions (3.24) and (3.26) for the Rossby mode are valid for feedback rates larger than the Coriolis frequency as well as smaller.

Figure 4.5 shows the growth rate of the Rossby mode as a function of the feedback rate, for $\tau_H = 0$ and a variety of zonal, meridional and vertical wavelengths. The most notable feature of Figure 4.5 is that for each wave scale the Rossby mode growth rate peaks at a specific feedback rate. This result is consistent with (3.21), (3.24) and (3.26), which indicate that for small feedback rates the Rossby mode growth rate increases as the magnitude of the feedback rate increases, but for large feedback rates the growth rate decreases as the feedback rate increases. The precise transition cannot be determined analytically, but appears to be given by (3.27) i.e., near the lower bound of the feedback rate given in (3.25). For each of the wave scales of Figure 4.5, this value of the feedback rate is indicated on the figure. The agreement between this value and the actual feedback rate of maximum growth is evidently quite good.

The scale dependence of the Rossby mode growth rate also exhibits some interesting features. Figure 4.6 shows the growth rate as a function of vertical wavelength for two cases, each with $\tau_H = 0$. One curve is for synoptic scale waves with zonal and meridional wavelengths of 1000 km and a feedback rate of -10^{-7} s^{-1}, while the other curve is for planetary scale waves with zonal and meridional wavelengths of 10,000 km and a feedback rate of -10^{-6} s^{-1}. In each case the feedback rate is about an order of magnitude less than the external Rossby wave frequency. Thus, for large vertical wavelengths (3.19) applies and, according to (3.21), the Rossby mode growth rate will increase as the vertical wavelength is decreased. For sufficiently small vertical wavelengths, (3.23) rather than (3.19) applies, so that, according to (3.24), the Rossby mode growth rate will decrease as the vertical scale

decreases. For some intermediate vertical wavelength then, the growth rate will peak. Although we cannot demonstrate it analytically, we expect this transition to occur when the internal Rossby mode frequency has decreased sufficiently to match the feedback rate, i.e., when

$$n^2 = -\frac{N^2 k_2^2}{f^2}\left(\frac{\beta k}{\alpha k_2^2} + 1\right) \quad . \tag{4.14}$$

The vertical wavelength at which this occurs is indicated in Figure 4.6. The agreement with the actual vertical wavelength of maximum growth rate is seen to be fair.

A second transition in the dependence of the growth rate on vertical scale occurs when (3.27) is satisfied. Figure 4.7 shows the Rossby mode growth rate as a function of vertical wavelength for two different cases. The horizontal scales are the same as in the previous Figure, but the feedback rates have been increased by a factor of 100 for each case. The feedback rates are now about an order of magnitude greater than the external Rossby wave frequency. Thus, for large vertical wavelengths, (3.25) applies and, according to (3.26), the Rossby mode growth rate will increase as the vertical scale decreases. For sufficiently small vertical wavelengths, (3.23) rather than (3.25) applies, so that, according to (3.24), the Rossby mode growth rate will decrease as the vertical scale decreases. For some intermediate vertical wavelength then, the growth rate will peak, but the transition occurs when (3.27), or equivalently,

$$n^2 = -\frac{N^2 k_2^2}{f^2}\left(\frac{\alpha k_2^2}{\beta k} + 1\right) \tag{4.15}$$

rather than (4.14) is satisfied. The vertical wavelength at which this occurs is indicated in Figure 4.7. The agreement with the actual vertical wavelength of maximum growth rate is seen to be somewhat better than the previous case.

The dependence of the Rossby mode growth rate on zonal scale is even more complicated. For sufficiently small or large zonal wavenumber, the condition (3.25)

is satisfied, in which case the growth rate increases with zonal wavenumber if $k^2 < \ell^2/2$, and decreases with zonal wavenumber if $k^2 > \ell^2/2$. Thus, if condition (3.25) is satisfied for all zonal wavenumbers, then the growth rate of the Rossby mode is largest when $k^2 = \ell^2/2$. This situation is illustrated in Figure 4.8, which shows the Rossby mode growth rate as a function of zonal wavelength for a meridional wavelength of 1000 km, a vertical wavelength of 10 km, $\tau_H = 0$, and a feedback rate of -10^{-4} s^{-1}. As expected, the growth rate is seen to peak at a zonal wavelength of about 1500 km, when $k^2 = \ell^2/2$.

For sufficiently small feedback rates or sufficiently large meridional and vertical scales, the condition (3.19), that the feedback rate be much smaller than the internal Rossby wave frequency, is satisfied for a wide range in zonal scales. For such scales the Rossby mode growth rate decreases with increasing zonal wavenumber, in contrast to the case in which condition (3.25) is satisfied but $k^2 < \ell^2/2$, or the case in which condition (3.23) is satisfied but $k^2 < \ell^2 + f^2n^2/N^2$. Thus, as the zonal wavenumber is increased from values much smaller than the meridional wavenumber, the increase in growth rate with zonal wavenumber will change to a decrease with zonal wavenumber, not because $k^2 > \ell^2/2$ or $k^2 > \ell^2 + f^2n^2/N^2$, but because the internal Rossby wave frequency increases enough to dominate the feedback rate, i.e., condition (3.19) is satisfied. This might suggest that for sufficiently small feedback rates or sufficiently large meridional and vertical scales the peak growth rate occurs when the internal Rossby wave frequency equals the magnitude of the feedback rate. However, the maximum internal Rossby wave frequency for given meridional and vertical scales occurs when $k^2 = l^2 + f^2n^2/N^2$, so that the Rossby wave frequency can only dominate the feedback rate if the transition between conditions (3.23) and (3.19) occurs at a zonal wavenumber $k^2 \ll \ell^2 + f^2n^2/N^2$. For such small zonal wavenumbers, the dependence of the growth rate on zonal scale

according to (3.21) is much weaker than that according to (3.24) or (3.26). Although the approximate expressions (3.21), (3.24) and (3.26) are not formally valid when the internal Rossby wave frequency equals the feedback rate, the comparison of the scale depedence for the approximate expressions does suggest that the growth rate peaks not when the internal Rossby wave frequency equals the feedback rate, but when it is much larger. Thus, for conditions in which the Rossby wave frequency dominates the feedback rate, the growth rate of the Rossby mode peaks at zonal scales substantially smaller than that at which the Rossby wave frequency equals the feedback rate. Such zonal scales can, for sufficiently weak feedback, far exceed that implied when the conditions (3.23) or (3.25) apply. This case is illustrated in Figure 4.9, which shows the Rossby mode growth rate as a function of zonal wavelength for a meridional wavelength of 1000 km, a vertical wavelength of 10 km, $\tau_H = 0$, and a feedback rate of 10^{-8} s^{-1}. For such meridional and vertical scales, the zonal wavelength for which $k^2 = \ell^2 + f^2 n^2/N^2$ is 700 km, and the zonal wavelength for which $k^2 = \ell^2/2$ is 1400 km, both smaller than the zonal scale 8000 km at which the growth rate actually peaks. For comparison, the zonal scale for which the internal Rossby mode frequency equals the feedback rate is the implausible 120,000 km.

When the wave is shallow, i.e., when $f^2 n^2 \gg N^2 \ell^2$, condition (3.23) is satisfied for a wide range in zonal scales. For such waves the Rossby mode growth rate peaks at zonal wavenumber $k^2 = \ell^2 + f^2 n^2/N^2$. Figure 4.10 shows the growth rate as a function of zonal wavelength for a meridional wavelength of 10,000 km, a vertical wavelength of 10 km, $\tau_H = 0$, and feedback rates of -10^{-4}, -10^{-6}, and -10^{-8} s^{-1}. For the strong feedback case, condition (3.25) is nearly satisfied for all zonal scales. The peak growth rate therefore occurs at a zonal wavelength, 6000 km, which is much larger than that corresponding to $k^2 = \ell^2 + f^2 n^2/N^2$, i.e., 1000 km, but is also somewhat smaller than that corresponding to $k^2 = \ell^2/2$,

i.e., 14,000 km. For the weak feedback case, condition (3.19) is satisfied for a wide range in zonal scales; for the reasons outlined above, the growth rate for the case of weak feedback therefore peaks at a large zonal scale, i.e., at about 12,000 km (the correspondence between this value and that corresponding to $k^2 = \ell^2/2$ is purely coincidental, for the conditions required for such a correspondence are not satisfied). For the moderate feedback case, the feedback rate is near the maximum internal Rossby wave frequency and hence satisfies the conditions (3.23) for which the zonal wavelength at peak growth rate is predicted to correspond to $k^2 = \ell^2 + f^2 n^2/N^2$, or 1000 km; the actual zonal wavelength at which the growth rate is largest is seen to be about 2000 km.

The dependence of the Rossby mode growth rate on the meridional scale is much simpler: for all parameter regimes, the growth rate increases as the meridional scale of the perturbation increases. Thus, waves with the largest meridional scale consistent with the horizontal domain of the radiative-dynamical feedback will grow fastest in the linear stage.

We have so far only considered the scale dependence of the growth rate for each dimension separately. A more general question is: for which three-dimensional wave vector is the Rossby mode growth rate largest? According to the analysis of Chapter 3, the Rossby mode growth rate is much less than the feedback rate when conditions (3.23) or (3.25) are satisified, but can be as large as the feedback rate when condition (3.19) is satisfied. When (3.19) is satisfied, the feedback rate is largest for waves that are shallow and long, i.e., $f^2 n^2 \gg N^2 k_2^2$. However, if the waves are too shallow, the internal Rossby wave frequency won't exceed the feedback rate, so that condition (3.19) is not satisfied. Thus, the growth rate is largest for waves that are very long and deep enough to satisfy (3.19). This is illustrated in Figure 4.11, which shows the Rossby mode growth rate contoured as a function of zonal and vertical wavelength for a meridional wavelength of 10,000

km, $\tau_H = 0$, and a feedback rate of -10^{-5} s^{-1}. The growth rate is seen to increase as the zonal and vertical scales are progressively increased.

For many problems the zone of strong radiative dynamical feedback may be somewhat restricted. For example, a layer of strong absorber gradient may span only a few kilometers. In that case the vertical wavelength of the unstable modes should not exceed the vertical span of strong feedback. The zonal scale of the fastest growing Rossby mode would then be limited somewhat.

The analysis of the primitive equations on a mid-latitude β-plane has so far been based on (4.12), which admits nontrivial solutions if the meridional velocity is nonzero. If, on the other hand, the meridional velocity is identically zero, the primitive equations can be reduced to a single wave equation for the vertical velocity,

$$D^3 \frac{\partial}{\partial z} \frac{1}{\rho_0} \frac{\partial}{\partial z} (\rho_0 w) + N^2 (D - \alpha) w_{xx} = 0 \quad . \tag{4.16}$$

Substituting solutions of the form (3.14) yields the algebraic relation

$$n^2 D^3 + N^2 (D - \alpha) k^2 = 0 \quad . \tag{4.17}$$

This cubic equation is identical to the corresponding equation for the primitive equations on an f-plane, except that the two-dimensional wavenumber k_2^2 has been replaced by the zonal wavenumber k^2, and the Coriolis parameter is absent. Thus, in the absence of radiative-dynamical feedback, it describes an advective mode and two gravity (rather than inertia-gravity) modes. The Rossby mode is missing because the meridional velocity is identically zero.

In the presence of the radiative-dynamical feedback, the analysis of section 4.1 applies, but with the two-dimensional and three-dimensional wavenumbers replaced by the zonal wavenumber. Thus, for positive radiative-dynamical feedback, the advective mode is unstable in the absence of dissipation and the gravity modes are damped, while for negative feedback the advective mode is damped and the gravity

modes are unstable. For weak radiative-dynamical feedback (i.e., $|\alpha| \ll Nk/n$), the growth rates are, in the absence of dissipation, proportional to the feedback rate, while for strong feedback ($|\alpha| \gg Nk/n$) the growth rate is proportional to the cube root of the feedback rate. The maximum growth rate of the advective mode is the feedback rate, which occurs for all wavenumbers such that $|\alpha| \ll Nk/n$. The maximum growth rate of the gravity modes is one half the feedback rate, which again occurs for all wavenumbers such that $|\alpha| \ll Nk/n$. In no instance does the advective mode propagate, while the frequency of the gravity modes dominates the growth rate except when $|\alpha| \gg Nk/n$.

Finally, let us consider cases for which $\tau_H \neq 0$. If τ_H is large and perturbations are deep ($2mH \ll 1$), (2.7) reduces to (2.11), and the perturbation heating and absorber concentration are 180° out of phase, rather than in phase as in the case $\tau_H = 0$. One therefore expects the mode of instability to change as τ_H is increased from zero to large values. Figure 4.12 shows the growth rate of the advective, Rossby, and inertia-gravity modes as a function of τ_H for $\alpha = 10^{-5}$ s^{-1}, zonal and meridional wavelengths of 1000 km, and a vertical wavelength of 10 km (note that the requirement that $2mH \ll 1$ cannot be strictly satisfied for any reasonable perturbation, for it requires vertical wavelengths much larger than 100 km). For small τ_H, $\alpha_e \simeq \alpha$ so the advective mode is unstable while the Rossby and gravity modes are damped. For larger τ_H the radiative heating is less strongly coupled to the absorber concentration, so that the effective radiative dynamical feedback is reduced (it is important to note here that because α has been held constant in Figure 4.12, we have neglected the dependence of the basic state transmissivity on optical depth; the magnitude of α_e would be expected to decline exponentially with increasing optical depth if this effect were accounted for). For $\tau_H = 2n^2H^2$ (= 51 for a 10 km vertical wavelength and a density scale height of 8 km), where n^2 is defined by (3.16), the radiative heating and absorber concentration are uncorrelated

(at zero lag) even for shallow perturbations, and the growth rate of all modes is exactly zero (in the absence of dissipation). For larger τ_H, the radiative heating and absorber concentration are negatively correlated, and the advective mode is damped while the Rossby and inertia-gravity modes amplify.

Figure 4.13 shows the growth rate of the advective mode as a function of vertical wavelength for $\alpha = 10^{-5}$ s^{-1}, zonal and meridional wavelengths of 1000 km, and for $\tau_H = 0$, 1, and 10. For $\tau_H = 0$, the previous analysis is valid, which concludes that the growth rate of the advective mode is largest for the deepest waves. However, such a case is unphysical, for it does not permit any basic-state absorber. For $\tau_H = 1$ and $\tau_H = 10$, the growth rate of deep waves is smaller than for $\tau_H = 0$. Indeed, when $n^2 = \tau_H/(2H^2)$, which corresponds to vertical wavelengths of 100 km and 23 km for $\tau_H = 1$ and 10, respectively, the growth rate of the advective mode is zero; for deeper waves, the advective mode is damped. Thus, the growth rate of the advective mode is largest at a vertical wavelength that must be smaller than that corresponding to $n^2 = \tau_H/(2H^2)$.

If waves are shallow ($m \gg 1/(2H)$, which is satisfied for vertical wavelengths much less than 100 km) but deep enough that $\tau_m = \tau_H/(mH)$ is large, (2.7) reduces to (2.12). The perturbation heating and absorber concentration are 90° out of phase, with the heating lagging the absorber for downward phase propagation, but leading the absorber for upward propagation. The effective radiative-dynamical feedback, defined by (3.13), is in this case complex. In fact, if $\tau_H = 2n^2H^2$ the feedback is pure imaginary; for other τ_H which are consistent with large τ_m and large mH the imaginary part of α dominates the real part. Then the quasi-geostrophic solution for D becomes

$$D = \frac{i\left(k\beta + \alpha_i k_2^2\right) \pm \sqrt{4k_3^2 k\beta\alpha_i - \left(k\beta + \alpha_i k_2^2\right)^2}}{2k_3^2} \quad . \tag{4.18}$$

Here the feedback parameter has been expressed $\alpha_e = i\alpha_i$, where

$$\alpha_i = -\alpha \frac{\tau_H m H}{n^2 H^2} \tag{4.19}$$

is either positive or negative, depending on the sign of the vertical wavenumber m.

If α_i is negative, then from (4.18) we conclude that both roots of D are pure imaginary, indicating propagation but neither growth nor decay. In this case the real part of the feedback, however small, determines the rate of growth or decay.

On the other hand, if

$$\frac{k\beta}{k_2^2} \frac{\left(k_3 - \frac{fn}{N}\right)^2}{k_2^2} < \alpha_i < \frac{k\beta}{k_2^2} \frac{\left(k_3 + \frac{fn}{N}\right)^2}{k_2^2} \tag{4.20}$$

then the roots of D have real components, reflecting growth and decay of the respective modes. The growth rate can, in fact, be quite strong, with a maximum growth rate of

$$D_r = \frac{k\beta}{k_2^2} \frac{fn}{k_3 N} \tag{4.21}$$

occurring for

$$\alpha_i = \frac{k\beta}{k_2^2} \frac{k_3^2 + \frac{f^2 n^2}{N^2}}{k_2^2} \quad . \tag{4.22}$$

If α is small (i.e., much smaller than the external Rossby wave frequency), the growth rate can actually be much larger than α, but is less than α_i as well as the oscillation frequency, which is that of an external Rossby wave. Thus, the growth rate is bounded by the magnitude of the effective feedback rate, even when α_e is complex.

This analytic result is surprising, as one might intuitively expect the instability to vanish when the real part of the effective feedback is zero. Indeed, Figure 4.12 exhibits just such behavior, with the growth rate of all modes vanishing for $\tau_H = 2n^2H^2$. To explain why unstable modes are possible when the $\mathrm{Re}(\alpha_e)$ is zero and the condition (4.20) is satisfied, consider the phase structure of unstable

solutions illustrated in Figure 4.14 for the two cases arising when α_i is positive, i.e., when α is positive and m is negative, and when α is negative and m is positive.

If α is positive, then the basic state absorber mixing ratio decreases with height, and high absorber concentrations lag upward motion. For negative m phase propagation is upward when (4.20) is satisfied, so that weak heating lags high absorber concentrations by 90°. Thus, cool temperatures lagging the weak heating coincide with downward motion, indicating positive energy conversion, and hence instability.

If α is negative, then high absorber concentrations lag downward motion. For positive m phase propagation is downward when (4.20) is satisfied, so that strong heating lags high absorber concentrations. The warm temperatures following the strong heating coincide with upward motion, indicating instability.

These unstable modes are characterized by roughly 45° phase lags between vertical motion and high absorber concentration and between radiative heating and warm temperatures. The growth rate of these modes can therefore be comparable to the oscillation frequency. Thus, the downward-propagating Rossby mode ($m > 0$), which for the case $\tau_H = 0$, $\alpha < 0$ is characterized by growth rates much less than the oscillation frequency, grows more rapidly for large τ_m and large mH. On the other hand, the upward-propagating Rossby mode ($m < 0$) is rendered neutral for large τ_m and large mH because α_i is negative, and hence (4.20) is not satisfied. For the case illustrated in Figure 4.12, α_i is negative because both α and m are positive; the real part of D therefore vanishes when $\tau_H = 2n^2H^2$.

4.2.2. Equatorial β-plane

In the tropics it is not reasonable to treat the Coriolis parameter as a constant in (4.12). Following the classical theory, we approximate the Coriolis parameter as

a linear function of latitude. Equation (4.12) then becomes

$$\left(D^2+\beta^2y^2\right)D^2\,\frac{\partial}{\partial z}\,\frac{1}{\rho_0}\,\frac{\partial}{\partial z}\left(\rho_0 v\right)+N^2(D-\alpha)\left(D\nabla^2+\beta\,\frac{\partial}{\partial x}\right)v=0\quad . \tag{4.23}$$

Because the coefficients of (4.23) are no longer constant, the simple plane-wave solution form (3.14) is inappropriate. Following the classical theory, we express solutions in the form

$$v=V(y)e^{z/2H}e^{i(kx+mz-\sigma t)} \tag{4.24}$$

which reduces (4.23) to the ordinary differential equation

$$N^2(D-\alpha)DV_{yy}-\beta^2y^2D^2n^2V+\left[N^2(D-\alpha)(\beta ik-k^2D)-D^4n^2\right]V=0\ . \tag{4.25}$$

To reduce (4.25) to canonical form, we introduce the scaling $y=r\phi$ and choose

$$r^4=\frac{N^2(D-\alpha)D}{\beta^2D^2n^2}\quad . \tag{4.26}$$

Then (4.25) reduces to

$$V_{\phi\phi}-\phi^2V+\left[\frac{N^2\left(D-\alpha\right)\left(\beta ik-k^2D\right)-D^4n^2}{r^2\beta^2D^2n^2}\right]V=0\quad . \tag{4.27}$$

We can now expand solutions in a series of Hermite functions,

$$V(\phi)=\sum_{\ell}\bigvee_{\ell}H_\ell(\phi) \tag{4.28}$$

and apply the orthogonality relation

$$H_\ell''-\phi^2H_\ell=-(2\ell+1)H_\ell \tag{4.29}$$

to reduce (4.27) to the algebraic equation

$$n^2D^4+N^2\left(D-\alpha\right)\left(k^2D-ik\beta\right)+\left(2\ell+1\right)N\beta nD\sqrt{D(D-\alpha)}=0\quad . \tag{4.30}$$

Equation (4.30) has eight solutions for D. However, because D determines the meridional scaling (4.26), some of these solutions cannot satisfy the lateral

boundary conditions of boundedness. To see this, consider solutions with zero meridional velocity. Then the β term vanishes and the dispersion relation (4.30) reduces to

$$n^2 D^3 + N^2(D - \alpha)k^2 = 0 \quad . \tag{4.31}$$

Equation (4.31) is very similar to (4.7) without the Coriolis term. The analysis of section 4.1 demonstrates that two of the three solutions correspond to eastward and westward propagating gravity waves, and the third represents the advective mode, which does not propagate at all. From the momentum equations with $v = 0$ we find that

$$\Phi = \Phi_0 \exp\left(-\frac{1}{2}\, y^2\, \frac{k\beta}{iD}\right)\, e^{i(kx+mz-\sigma t)} \quad . \tag{4.32}$$

In order to satisfy the boundedness condition for large y, the imaginary part of D cannot be positive. Thus, only the eastward propagating (Kelvin) mode and the advective mode satisfy the boundary conditions; the westward propagating solution must be rejected. In contrast with the classical theory, in which D is purely imaginary and hence the solution is a Gaussian, D is complex in the presence of feedback, and solutions oscillate in latitude.

Because of the large number of solutions of (4.30), we shall not attempt further investigation of the equatorial β-plane here. Given the ubiquity of unstable modes in midlatitudes for nonzero meridional velocity and in the tropics for zero meridional velocity, we would expect to find additional unstable solutions of (4.30).

Table 4.1. Approximate solutions for the complex eigenfrequency σ. Perturbations in transmissivity are neglected (i.e., $\tau_H = 0$).

Mode	Feedback Rate				
	$\lvert\alpha\rvert \ll \frac{\beta k}{k_3^2}$	$\ll \lvert\alpha\rvert \ll$	$\frac{\beta k}{k_2^2}\frac{k_3^2}{k_2^2} \ll \lvert\alpha\rvert \ll$	$\frac{2Nk_3^3}{\sqrt{3}n\,k_2^2}$	$\ll \lvert\alpha\rvert$
Advective	$\frac{\alpha^2 k_3^2}{\beta k}\frac{f^2n^2}{N^2k_3^2} + i\alpha$	$(1+i)\alpha\left(\frac{\beta k}{2\alpha k_3^2}\right)^{1/2}$	$\frac{\beta k}{k_3^2}\frac{f^2n^2}{N^2k_2^2} + \frac{i\alpha k_2^2}{k_3^2}$		$i\alpha\left(\frac{N^2k_2^2}{\alpha^2n^2}\right)^{1/3}$
Rossby	$-\frac{\beta k}{k_3^2} - \frac{i\alpha f^2n^2}{N^2k_3^2}$	$-(1+i)\alpha\left(\frac{\beta k}{2\alpha k_3^2}\right)^{1/2}$	$-\frac{\beta k}{k_2^2} - \frac{i\beta^2k^2}{\alpha}\frac{f^2n^2}{N^2k_2^6}$		
Gravity			$\pm\frac{Nk_3}{n} - \frac{i\alpha k_2^2}{2k_3^2}$	$-\alpha\left(\frac{i\pm\sqrt{3}}{2}\right)\left(\frac{N^2k_2^2}{\alpha^2n^2}\right)^{1/3}$	

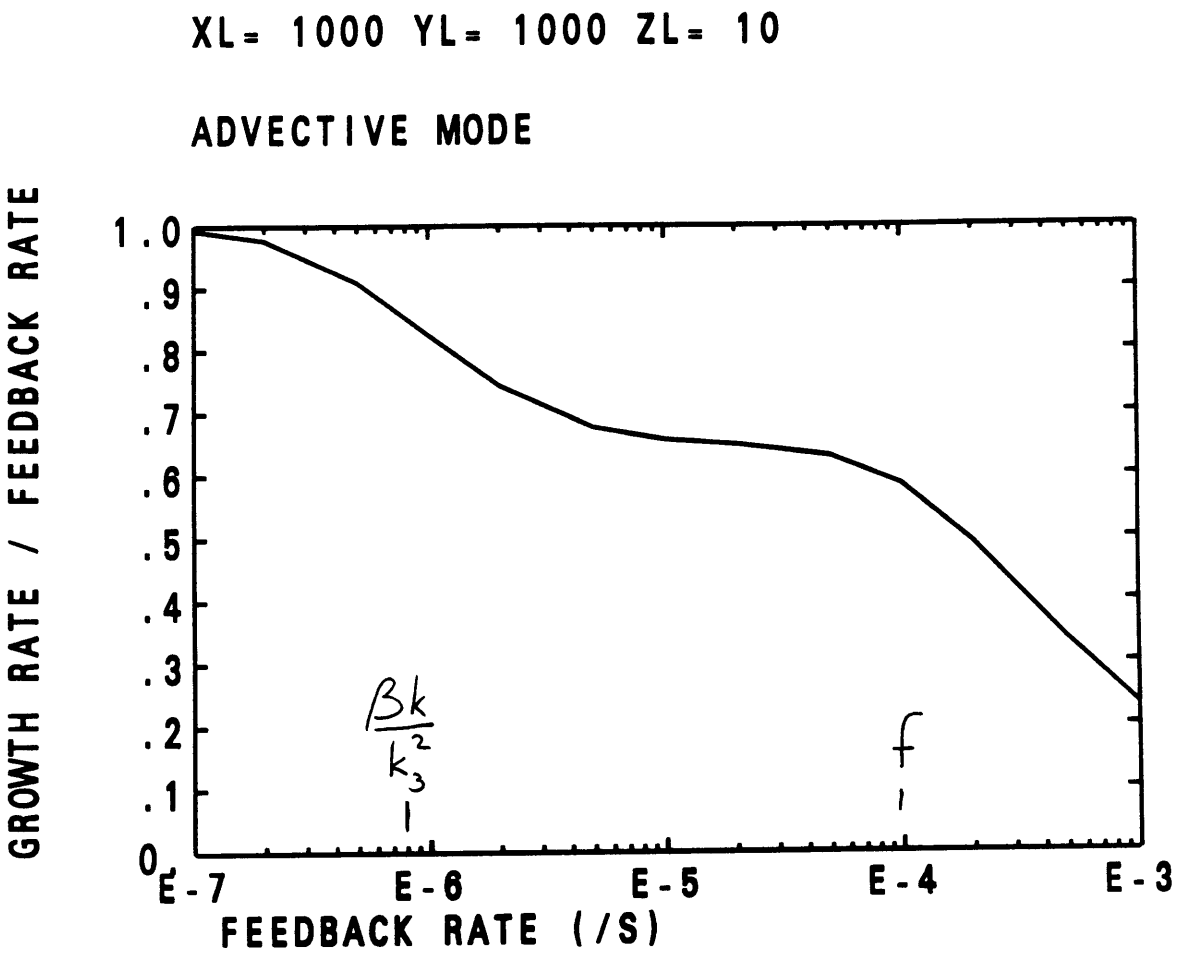

Figure 4.1. Advective mode growth rate normalized by the radiative-dynamical feedback rate, as a function of the feedback rate. Midlatitude beta-plane. The zonal and meridional wavelengths are 1000 km; the vertical wavelength is 10 km. The Brünt-Vaisala frequency is 10^{-2} s^{-1}; the density scale height is 8 km. Perturbations in transmissivity have been neglected ($\tau_H = 0$). The Coriolis and internal Rossby wave frequencies are indicated.

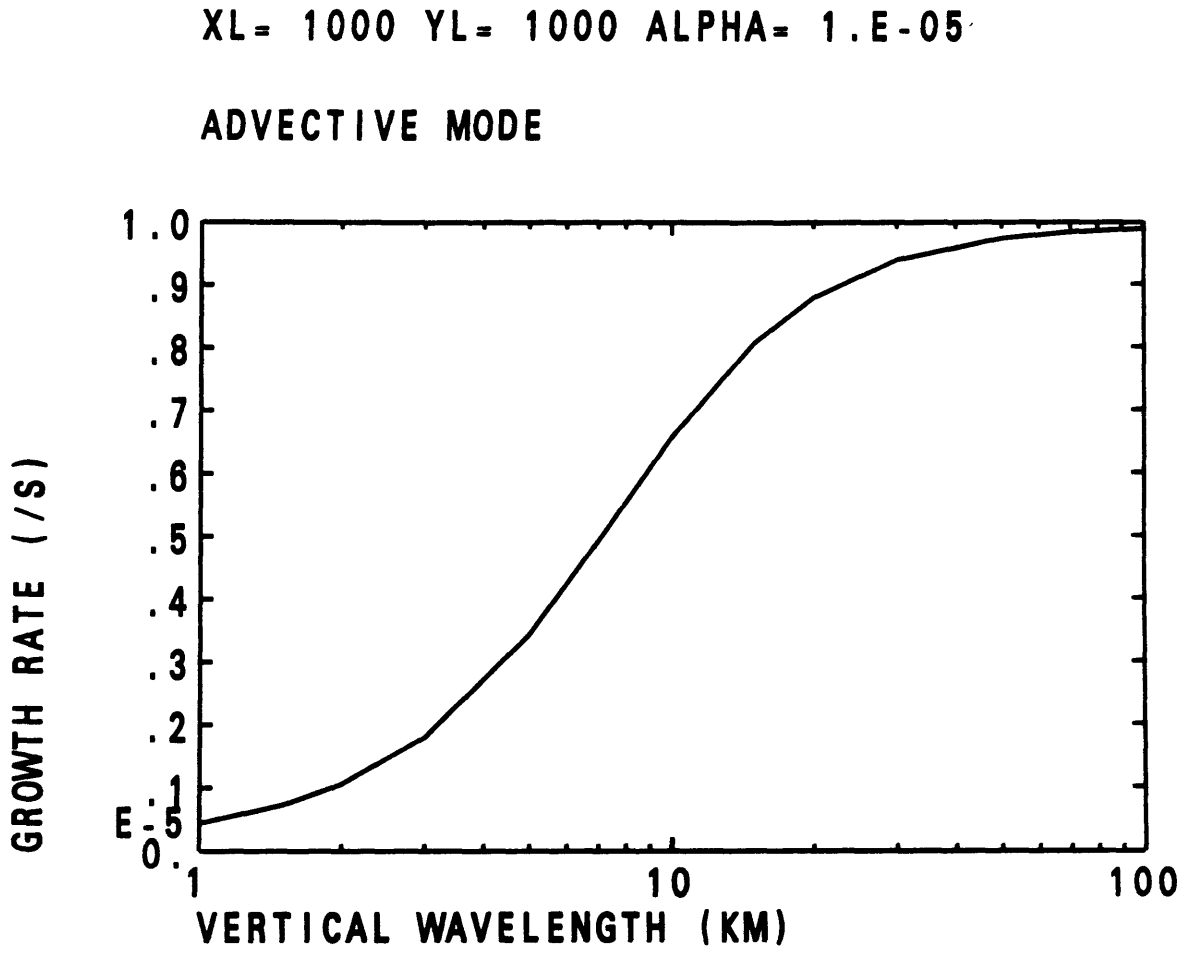

Figure 4.2. Advective mode growth rate as a function of vertical wavelength, for a radiative-dynamical feedback rate of 10^{-5} s^{-1}. Otherwise as in Figure 4.1.

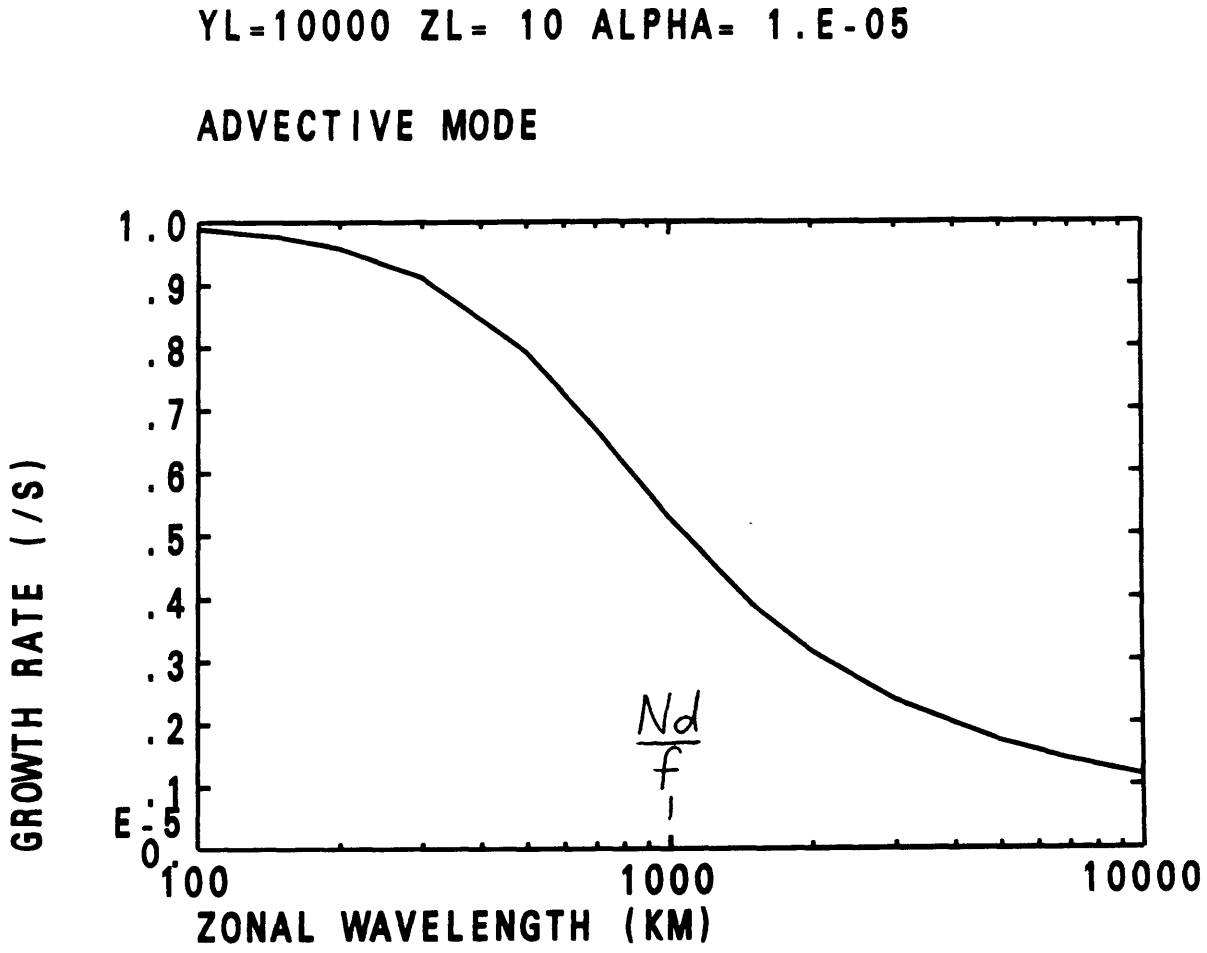

Figure 4.3. Advective mode growth rate as a function of zonal wavelength, for a radiative-dynamical feedback rate of 10^{-5} s^{-1} and a meridional wavelength of 10,000 km. Otherwise as in Figure 4.1. The internal deformation radius is indicated.

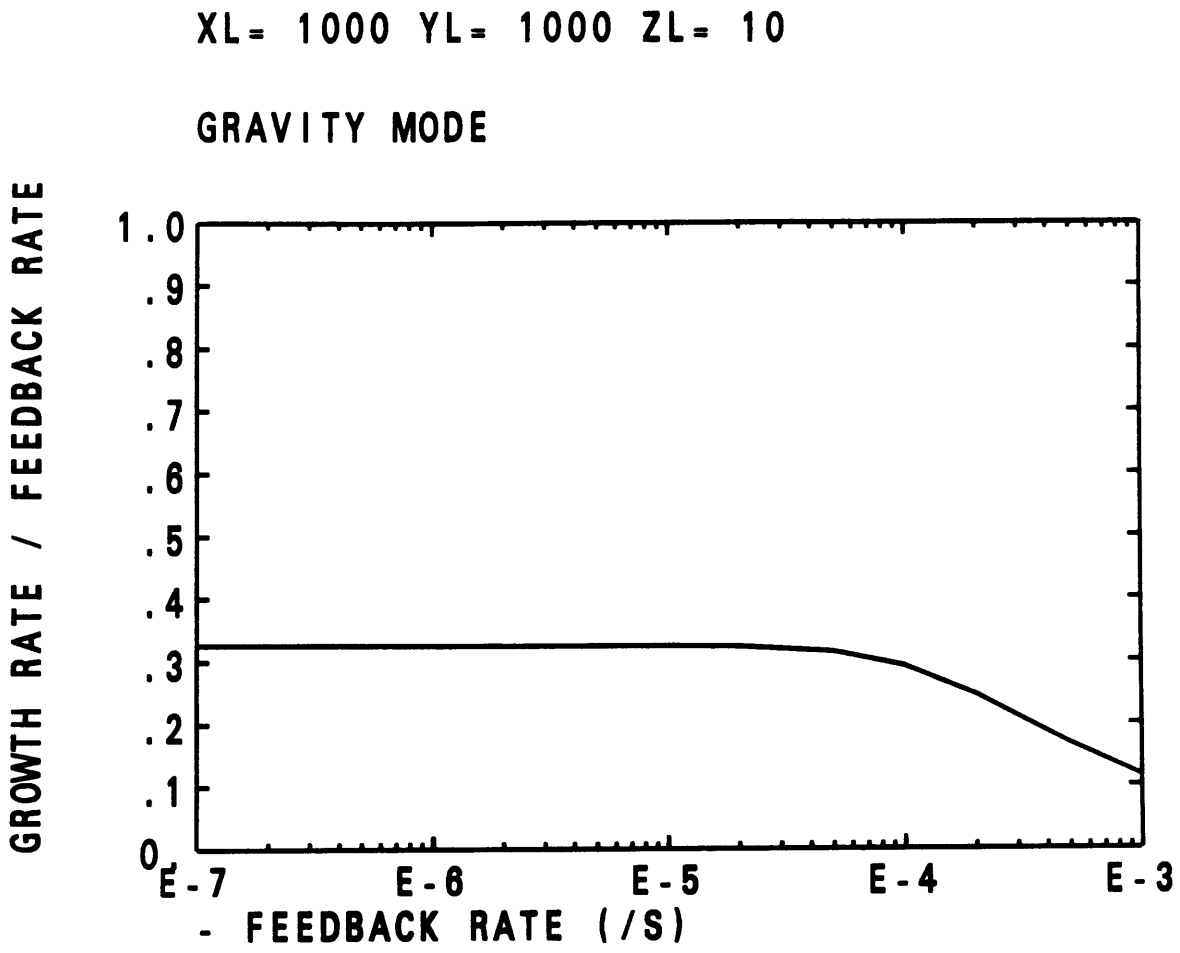

Figure 4.4. Normalized inertia-gravity mode growth rate as a function of the radiative-dynamical feedback rate. Otherwise as in Figure 4.1.

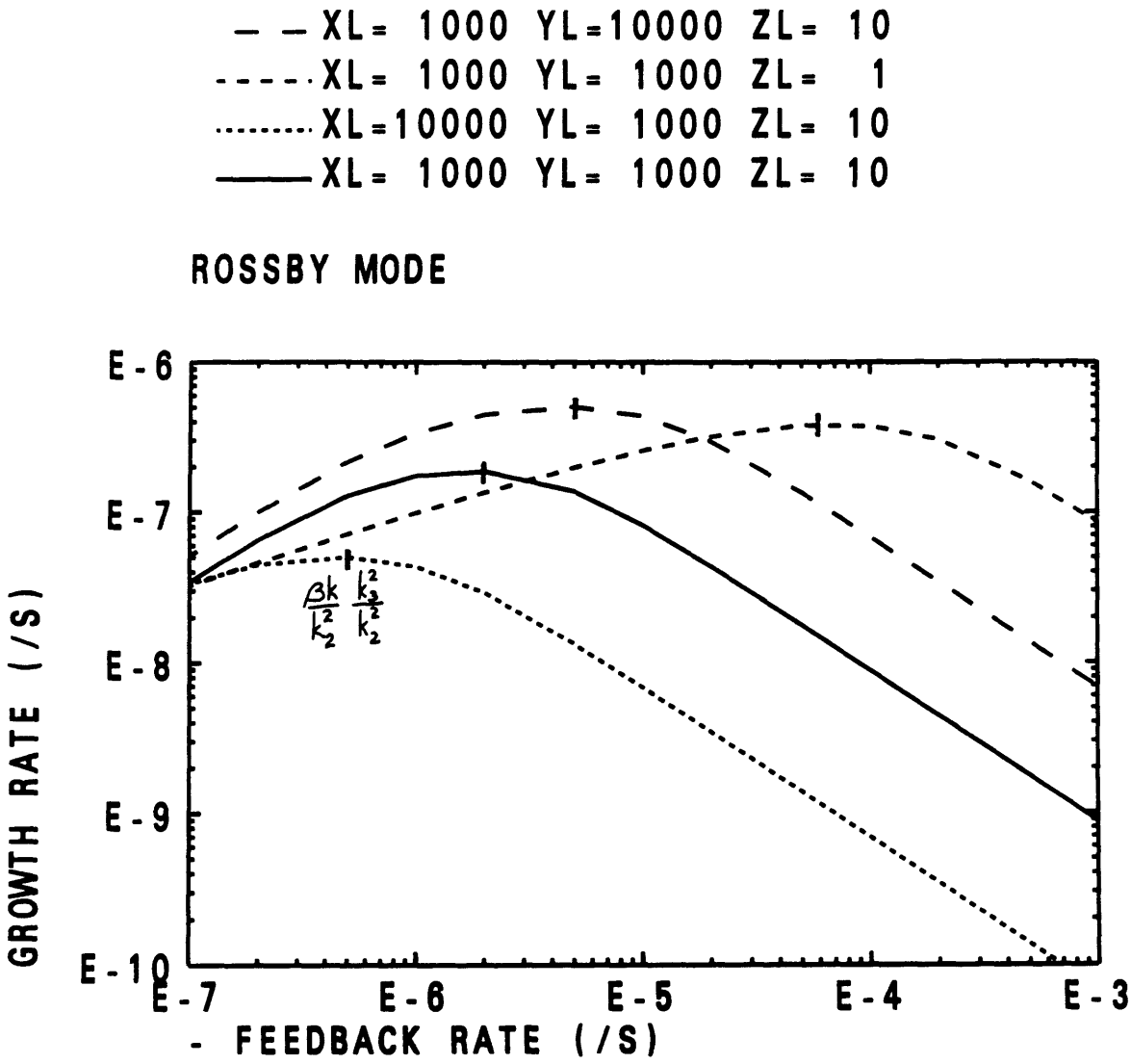

Figure 4.5. Rossby mode growth rate as a function of the radiative-dynamical feedback rate for zonal and meridional wavelengths of 1000 km and a vertical wavelength of 10 km (solid line); for a zonal wavelength of 1000 km, a meridional wavelength of 10,000 km, and a vertical wavelength of 10 km (long dashed line); for zonal and meridional wavelengths of 1000 km and a vertical wavelength of 1 km (medium dashed line); and for a zonal wavelength of 10,000 km, a meridional wavelength of 1000 km, and a vertical wavelength of 10 km (short dashed line). Otherwise as in Figure 4.1.

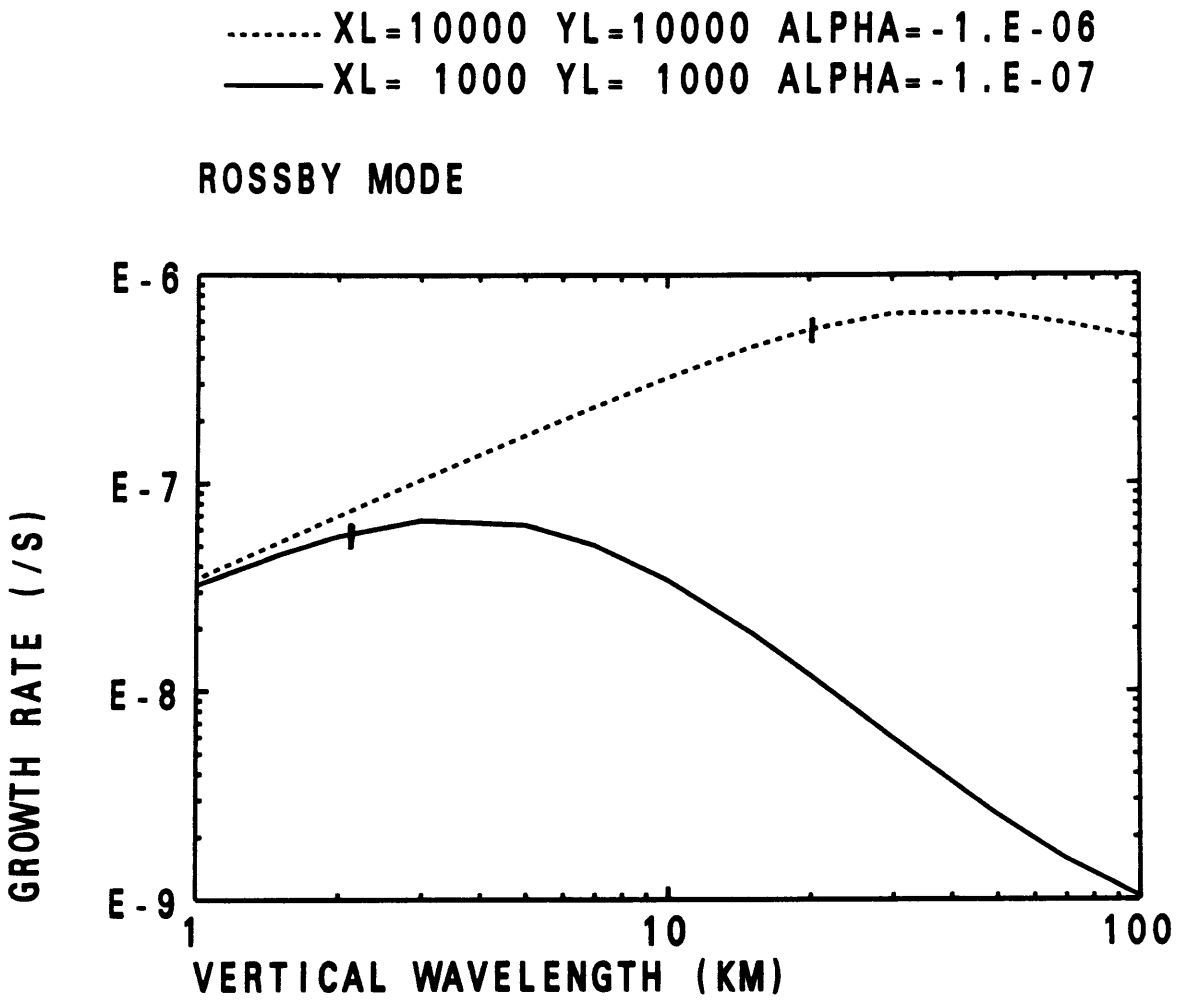

Figure 4.6. Rossby mode growth rate as a function of vertical wavelength for zonal and meridional wavelengths of 1000 km and a radiative-dynamical feedback rate of -10^{-7} s^{-1} (solid line); and for zonal and meridional wavelengths of 10,000 km and a feedback rate of -10^{-6} s^{-1} (dashed line). Otherwise as in Figure 4.1.

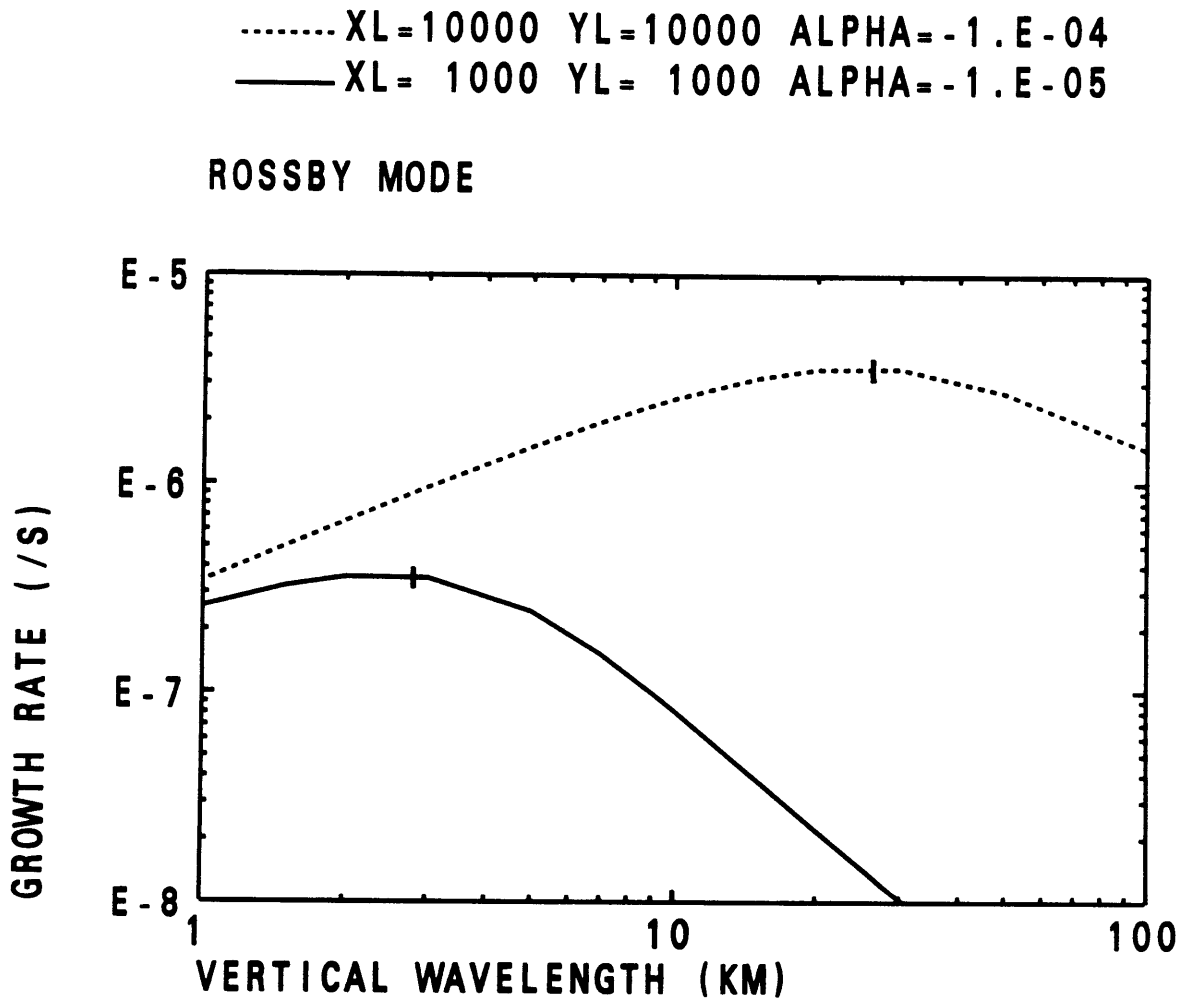

Figure 4.7. Rossby mode growth rate as a function of vertical wavelength for zonal and meridional wavelengths of 1000 km and a radiative-dynamical feedback rate of -10^{-5} s^{-1} (solid line); and for zonal and meridional wavelengths of 10,000 km and a feedback rate of -10^{-4} s^{-1} (dashed line). Otherwise as in Figure 4.1.

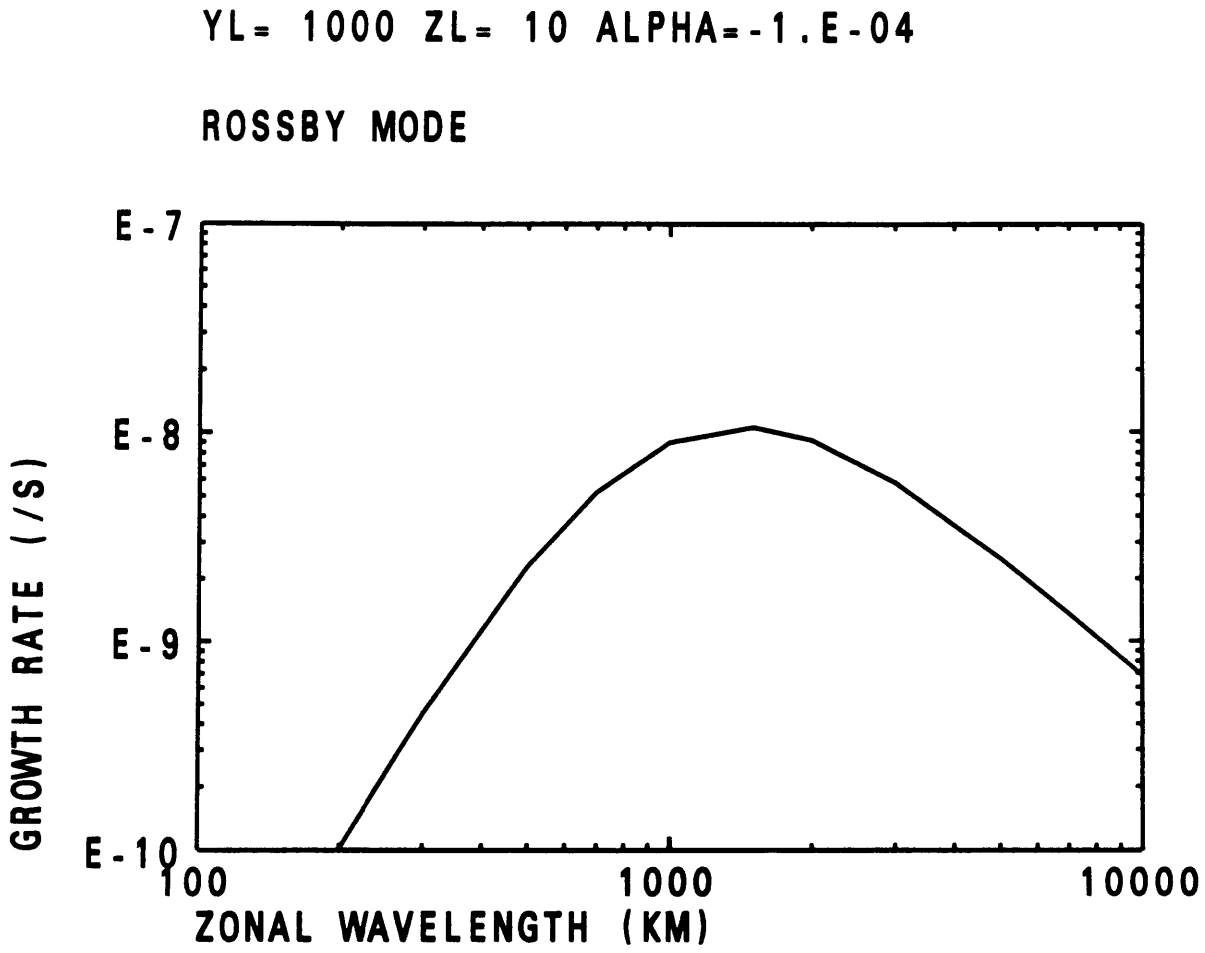

Figure 4.8. Rossby mode growth rate as a function of zonal wavelength for a meridional wavelength of 1000 km, a vertical wavelength of 10 km, and a radiative-dynamical feedback rate of -10^{-4} s^{-1}. Otherwise as in Figure 4.1.

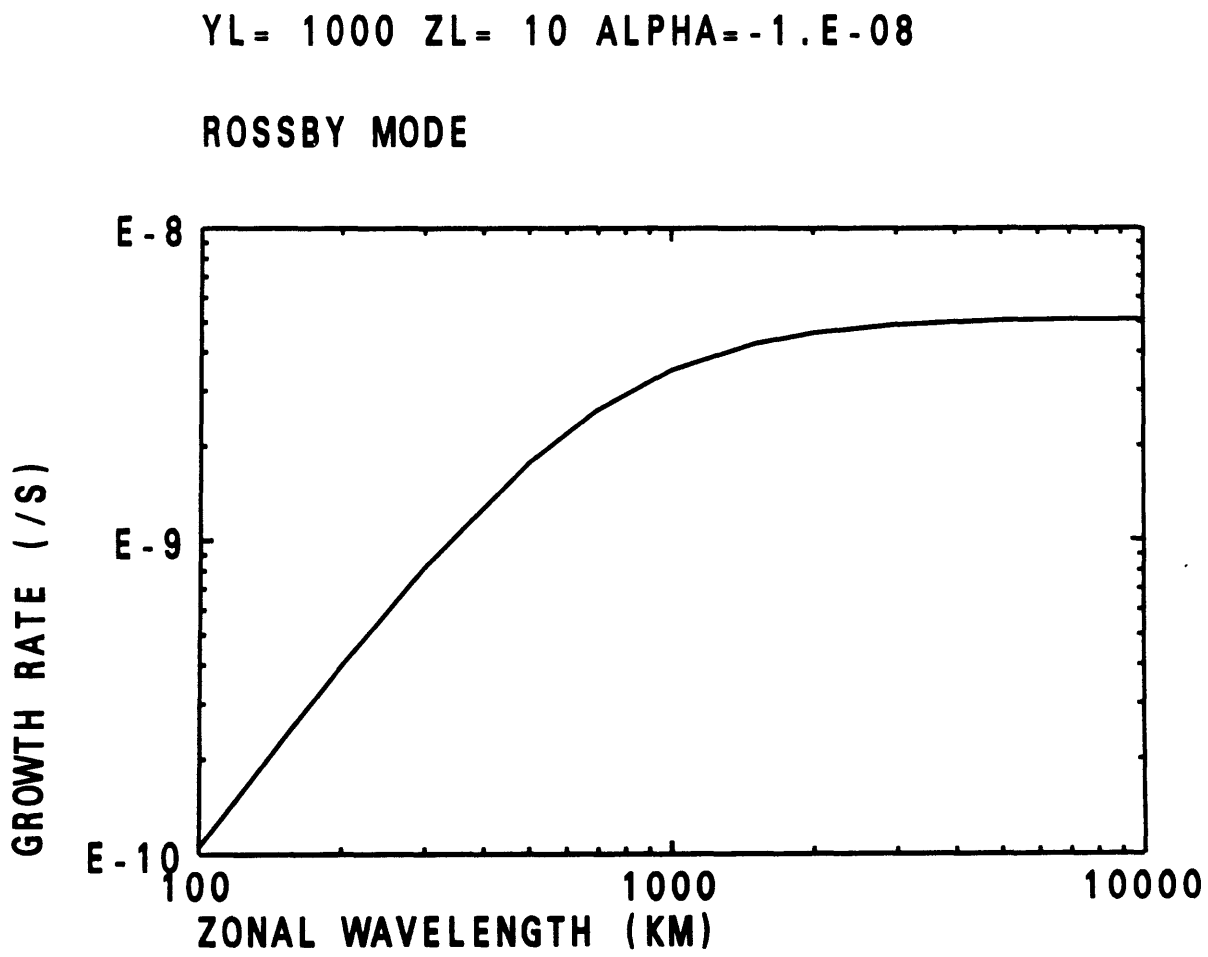

Figure 4.9. As in Figure 4.8, but for a radiative-dynamical feedback rate of -10^{-8} s^{-1}.

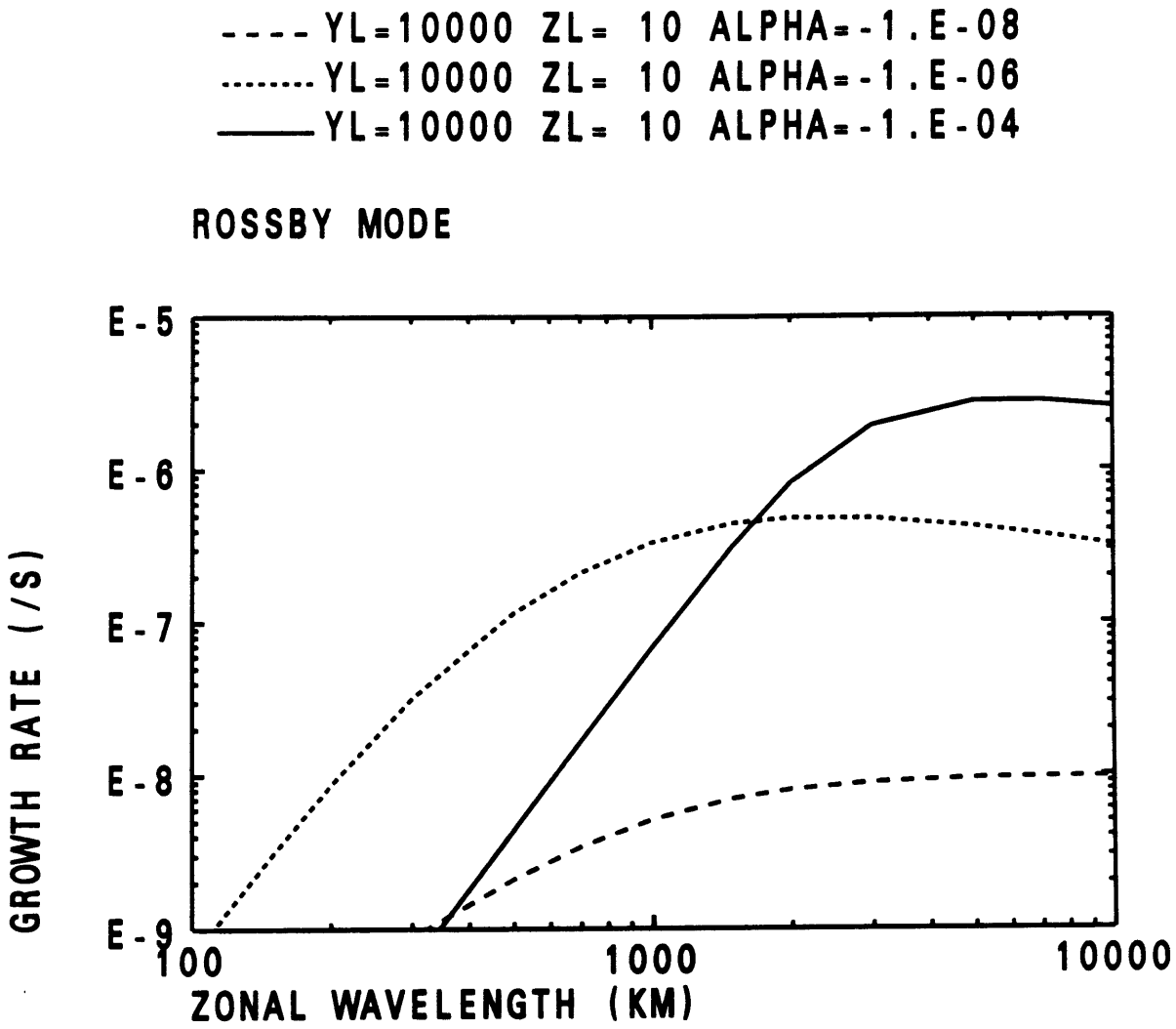

Figure 4.10. Rossby mode growth rate as a function of zonal wavelength for a meridional wavelength of 10,000 km, a vertical wavelength of 10 km, and radiative-dynamical feedback rates of -10^{-4} s^{-1} (solid line), -10^{-6} s^{-1} (short dashed line), and -10^{-8} s^{-1} (long dashed line). Otherwise as in Figure 4.1.

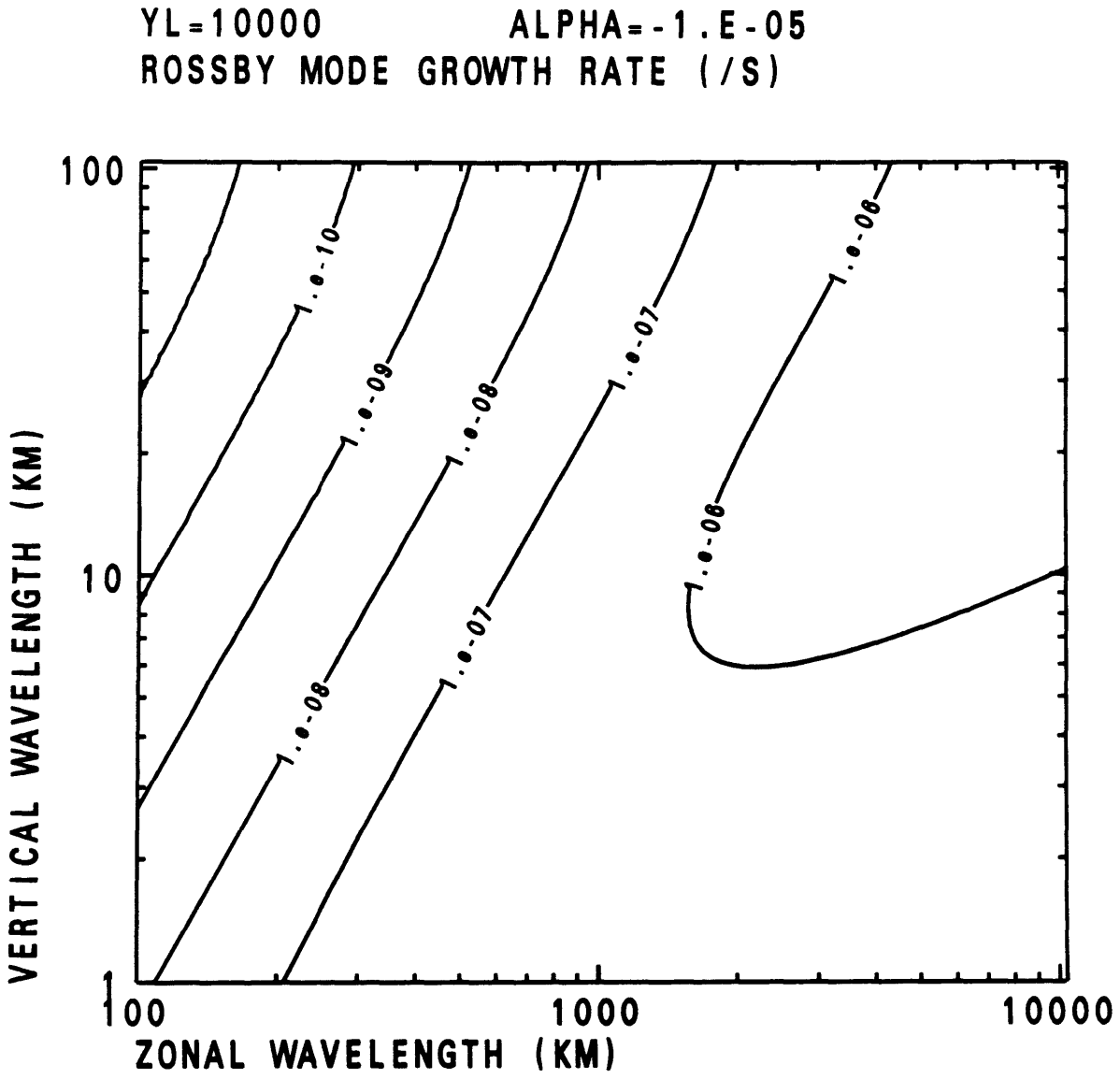

Figure 4.11. Rossby mode growth rate as a function of zonal and vertical wavelengths, for a radiative-dynamical feedback rate of -10^{-5} s^{-1} Otherwise as in Figure 4.1.

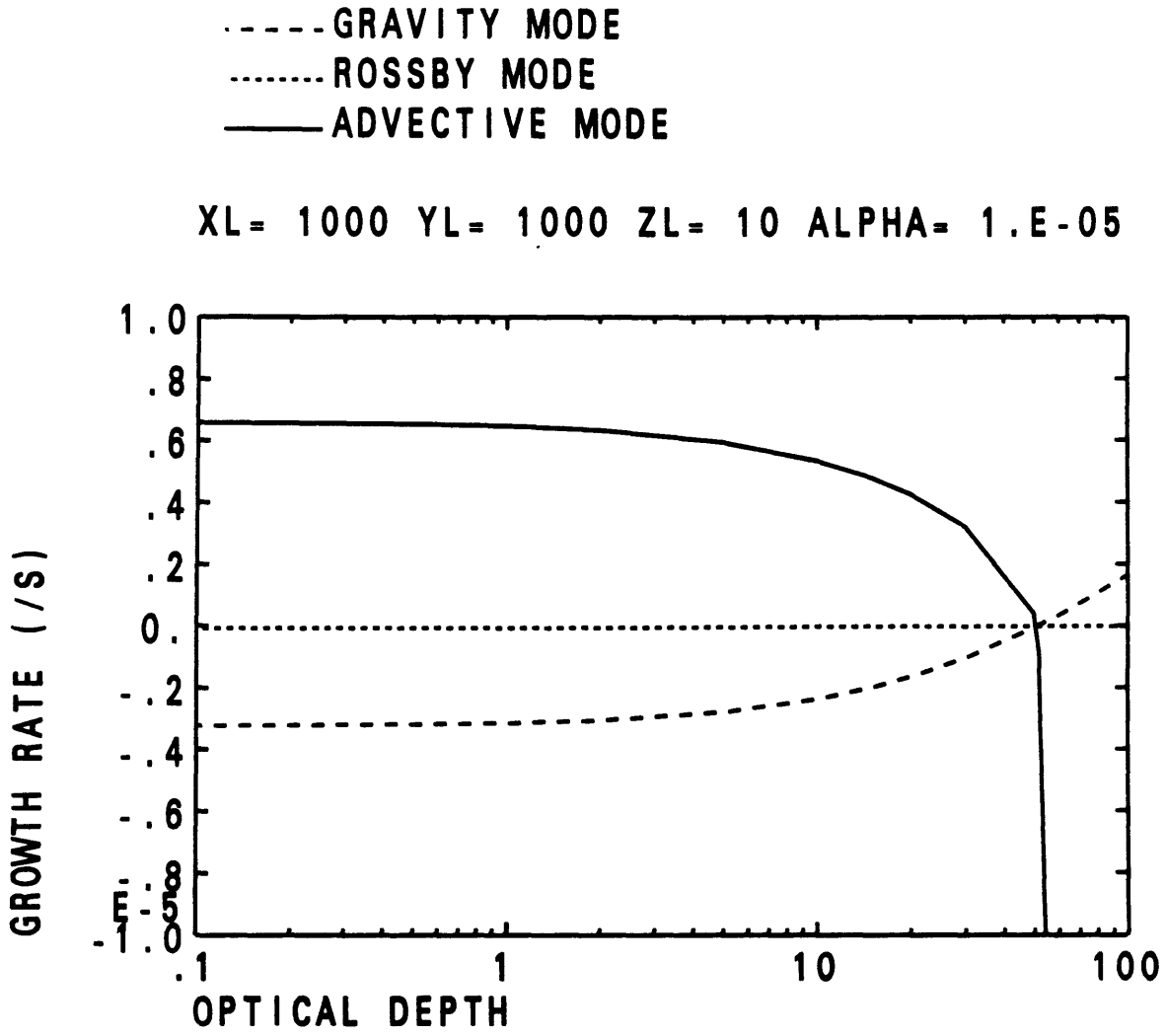

Figure 4.12. Growth rates of the advective mode (solid line), inertia-gravity mode (long dashed line), and Rossby mode (short dashed line) as functions of τ_H for a radiative-dynamical feedback rate of 10^{-5} s^{-1}, zonal and meridional wavelengths of 1000 km, and a vertical wavelength of 10 km. Midlatitude β-plane. The Brünt-Vaisala frequency is 10^{-2} s^{-1}; the density scale height is 8 km.

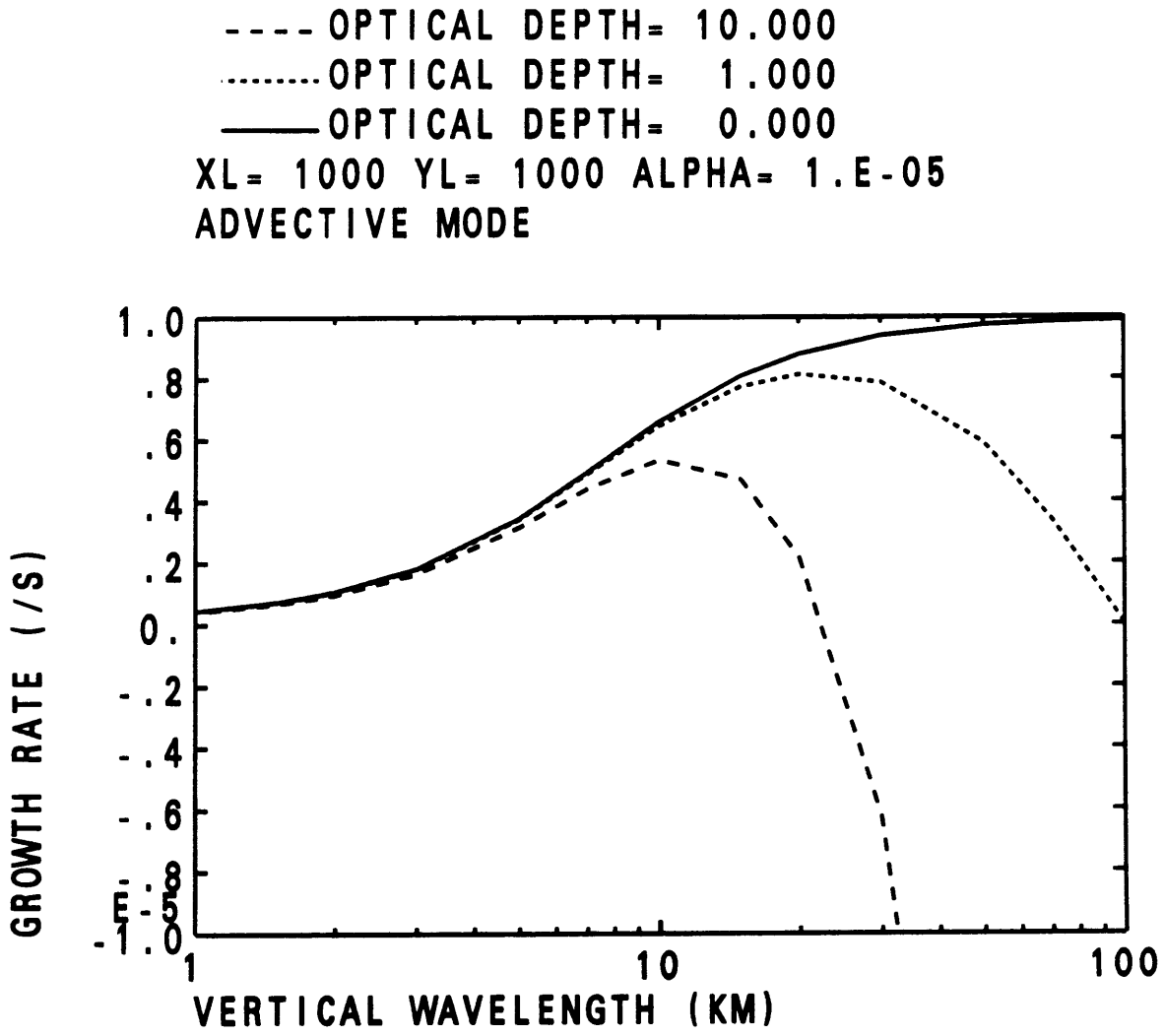

Figure 4.13. Advective mode growth rate as a function of vertical wavelength for $\tau_H = 0$ (solid line), $\tau_H = 1$ (short dashed line), and $\tau_H = 10$ (long dashed line). The radiative-dynamical feedback rate is 10^{-5} s^{-1}. Otherwise as in Figure 4.12.

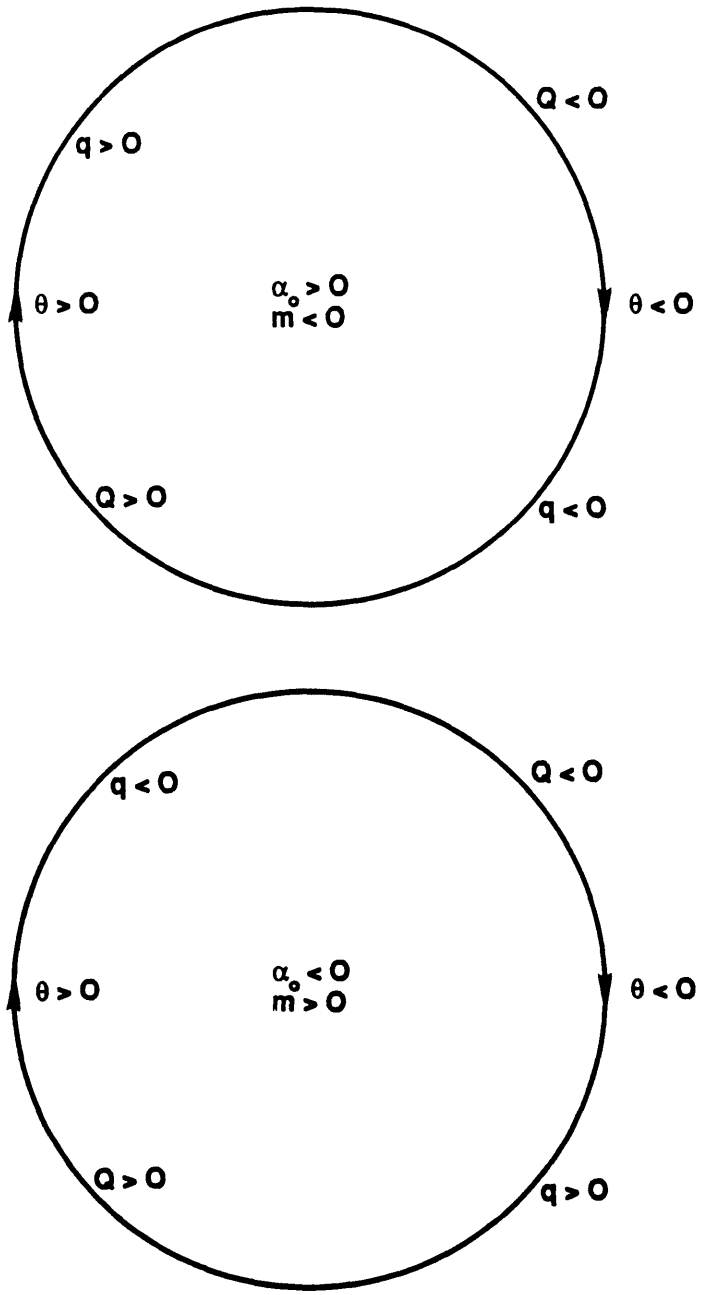

Figure 4.14. Phase structure of unstable modes associated with $\alpha > 0$, $m < 0$ (above) and $\alpha < 0$, $m > 0$ (below) for the case in which the imaginary part of the effective radiative-dynamical feedback parameter dominates the real part.

5. Effect of Dissipation

Until now we have only included the effects of dissipative processes on the unstable modes under the assumption that mechanical, thermal and absorbing damping are linear and equal in magnitude. This makes the treatment of the effects of damping on the growth rate of unstable modes trivial: the damping rate is simply subtracted from the real part of the advective-dissipative operator D to give the growth rate. If the damping rate exceeds $Re(D)$ then the modes decay rather than grow. Because $Re(D)$ is always less than the magnitude of the feedback rate, we conclude that all modes will decay if the damping rate exceeds the magnitude of the feedback rate.

In some instances such a treatment is reasonable. In the troposphere, Ekman pumping of barotropic Rossby waves leads to a decay time of typically 10 days, the radiative relaxation time is about 30 days, and the residence time of aerosols is 10–30 days, depending on proximity to precipitation systems. However, in the stratosphere, mechanical dissipation is less important, radiative damping is more rapid, while the residence time of aerosols is measured in months or years, and the photochemical lifetime of ozone is just a few hours. In the mesosphere, mechanical damping associated with gravity wave drag (Lindzen, 1981) leads to damping times of days. Even in the troposphere, mechanical damping of the advective and inertia-gravity modes is rather weak except in the tropics or near the surface. Thus, a consideration of different damping rates associated with mechanical and thermal dissipation, and with damping of the absorber concentration, is essential. We shall find that the sensitivity of the growth rate to each form of damping is quite different, and that the sensitivity of each wave mode also differs.

To treat different damping rates for momentum, heat, and absorber concentration, we replace the advective-dissipative operator D by $D + \epsilon_i$, where D now

represents only the advective operator, $i = 1$ corresponds to the mechanical damping rate, $i = 2$ to the thermal damping rate, and $i = 3$ to the absorber damping rate. Then (4.13) becomes

$$n^2 (D + \epsilon_3)(D + \epsilon_2)\left[(D + \epsilon_1)^2 + f^2\right] + N^2\left[(D + \epsilon_1) k_2^2 - ik\beta\right](D + \epsilon_3 - \alpha_e) = 0 \quad . \tag{5.1}$$

Once again, although exact analytical solutions to (5.1) have been found, we shall first consider approximate solutions of the quasi-geostrophic version of (5.1),

$$f^2 n^2 (D + \epsilon_3)(D + \epsilon_2) + N^2\left[(D + \epsilon_1) k_2^2 - ik\beta\right](D + \epsilon_3 - \alpha_e) = 0 \tag{5.2}$$

in the limit of strong damping, i.e., $\epsilon_i \gg \alpha$. For simplicity we shall assume $\tau_H \ll 1$, so that $\alpha_e \simeq \alpha$.

Consider first the case of strong mechanical damping ($\epsilon_1 \gg \alpha$) but weak thermal and absorber damping ($\epsilon_2 k_3^2, \epsilon_3 k_3^2 \ll \alpha k_2^2$). Then (5.2) reduces to

$$k_3^2 D^2 + \left(\epsilon_1 k_2^2 - ik\beta - \alpha k_2^2\right) D + \left(ik\beta - \epsilon_1 k_2^2\right)\alpha = 0 \quad . \tag{5.3}$$

If $\epsilon_1 k_2 \gg k\beta$, approximate solutions of (5.3) are

$$D \sim \frac{ik\beta}{k_3^2} - \epsilon_1 \frac{k_2^2}{k_3^2} \quad , \quad \alpha - \frac{ik\beta\alpha^2}{\epsilon_1^2} \frac{f^2 n^2}{k_2^4 N^2} \quad . \tag{5.4}$$

In this case the Rossby mode is strongly damped (the damping rate dominates the frequency), while the growth rate of the advective mode is actually increased by the mechanical damping if $\alpha k_2^2 \gg k\beta$ and $k_2^2 < k_3^2$ (compare with (3.26)). This surprising result can be explained in terms of the quasi-geostrophic vorticity and heat balance on an f-plane. In the absence of dissipation, the dynamical response to a given heating rate Q can be expressed $w = k_2^2 Q / \left(k_3^2 N^2\right)$; the response for a deep circulation $\left(k_3^2 = k_2^2\right)$ is therefore stronger than for a shallow circulation $\left(k_3^2 \gg k_2^2\right)$. In the presence of strong mechanical dissipation, we have found that

the dissipation rate greatly exceeds D for the advective mode because the growth rate is always less than α while ϵ_1 is assumed here to be much larger than α. The response for this case can therefore be approximated by $w = Q/N^2$, which is independent of the aspect ratio of the circulation. In this case the Coriolis acceleration of the divergent part of the circulation is balanced by the drag on the rotational part of the circulation. As the dissipation rate increases, the rotational circulation weakens with respect to the divergent circulation. Because the rotational flow is related through hydrostatic balance to temperature, the temperature perturbation becomes unimportant in the heat balance for strong drag. The heat balance then becomes the simple balance between the diabatic heating and the adiabatic cooling associated with vertical motion; however, if the dissipation rate exceeds the Coriolis frequency, the divergent part of the circulation becomes stronger than the rotational part, and the quasi-geostrophic assumption breaks down (this feature is evident in the solution using the primitive equations). In the absence of dissipation, part of the energy associated with the heating must be used to increase the thermal/rotational part of circulation. Because only the divergent part of the circulation contributes to the local increase in absorber concentration, and hence diabatic heating, the circulation with minimal storage of thermal energy is most efficient at generating eddy available potential energy. While this result contradicts one's intuitive notion that dissipation is an energy sink and hence should reduce growth rates, it is important to note that for quasi-geostrophic flow mechanical dissipation only reduces the intensity of the rotational part of the circulation; the divergent part, which is the circulation mode responsible for the instability, is undamped under quasi-geostrophic conditions.

If $\alpha k_2^2 \ll \epsilon_1 k_2^2 \ll k\beta$, approximate solutions of (5.3) are

$$D \sim \frac{ik\beta}{k_3^2} - \epsilon_1 \frac{k_2^2}{k_3^2} \quad , \quad \alpha - \frac{i\alpha^2}{k\beta} \frac{f^2 n^2}{N^2} \quad . \tag{5.5}$$

Although the frequency of the advective mode for this case differs from that in (5.4), it remains much less than the growth rate, which equals the inviscid growth rate (see (3.21)). The Rossby mode is again damped, but the damping rate is now much less than the frequency.

Consider now the case in which mechanical and absorber damping are weak ($\epsilon_1 k_2^2, \epsilon_3 k_3^2 \ll \alpha k_2^2, k\beta$), but thermal damping is strong ($\epsilon_2 f^2 n^2/N^2 \gg \alpha k_2^2$). Then (5.2) reduces to

$$k_3^2 D^2 + \left(\epsilon_2 \frac{f^2 n^2}{N^2} - ik\beta - \alpha k_2^2\right) D + ik\beta\alpha = 0 \quad . \tag{5.6}$$

If $\epsilon_2 f^2 n^2/N^2 \gg k\beta$, approximate solutions of (5.6) are

$$D \sim \frac{ik\beta}{k_3^2} - \epsilon_2 \frac{f^2 n^2}{k_3^2 N^2} \quad , \quad \frac{\alpha k^2 \beta^2 N^4}{\epsilon_2^2 n^4 f^4} - \frac{ik\beta\alpha N^2}{\epsilon_2 n^2 f^2} \quad . \tag{5.7}$$

As in the case with mechanical damping, strong thermal dissipation strongly damps the Rossby mode, with the damping rate dominating the frequency. In contrast with the case of mechanical damping, the growth rate of the advective mode is strongly reduced, but remains positive (though much less than the frequency) for positive radiative-dynamical feedback.

If $\alpha k_2^2 \ll \epsilon_2 f^2 n^2/N^2 \ll k\beta$, approximate solutions of (5.6) are

$$D \sim \frac{ik\beta}{k_3^2} - \epsilon_2 \frac{f^2 n^2}{k_3^2 N^2} \quad , \quad \alpha - \frac{i\alpha\epsilon_2 f^2 n^2}{k\beta N^2} \quad . \tag{5.8}$$

The approximate Rossby solution is the same as for stronger thermal damping, with damping at a rate much less than the frequency of oscillation. The advective mode growth rate is unchanged from the case without thermal dissipation (see (3.21)), indicating that the instability of the advective mode is not necessarily eliminated when the thermal damping rate exceeds the feedback rate. Unless waves are shallow ($k_3^2 \gg k_2^2$), the thermal damping rate must be much larger than both the feedback rate and the Rossby wave frequency in order to diminish the advective mode growth

rate. For shallow waves, the conditions required by (5.7) for stability are satisfied for thermal damping rates that are less than the feedback rate provided the thermal damping rate also exceeds the internal Rossby wave frequency. Because thermal damping rates generally increase as the vertical scale of the perturbation decreases (Fels, 1982), it is likely that thermal damping is much more capable of reducing the growth rate of shallow perturbations than deep perturbations.

Finally consider the case of strong damping of the absorber mixing ratio ($\epsilon_3 \gg \alpha$), but weak mechanical and thermal damping ($\epsilon_1 k_2^2, \epsilon_2 k_3^2 \ll \alpha k_2^2, k\beta$). Then (5.2) reduces to

$$k_3^2 D^2 + \left(\epsilon_3 k_3^2 - ik\beta - \alpha k_2^2\right) D + ik\beta\left(\alpha - \epsilon_3\right) = 0 \quad . \tag{5.9}$$

If $\epsilon_3 k_3^2 \gg k\beta$, approximate solutions of (5.9) are

$$D \sim \frac{ik\beta}{k_3^2} - \frac{\alpha k^2 \beta^2 f^2 n^2}{\epsilon_3^2 N^2 k_3^6} \quad , \quad -\epsilon_3 + \frac{ik\beta f^2 n^2}{\epsilon_3 N^2 k_3^2} \quad . \tag{5.10}$$

In this case the growth rate of the Rossby mode (for $\alpha < 0$) is greatly reduced by the strong absorber damping, but the instability is not eliminated. The advective mode, on the other hand, is strongly damped, with a westward rather than eastward phase velocity. However, as we shall see, the distinction between the Rossby mode and the advective mode is, despite appearances, not altogether obvious.

If $\alpha k_2^2 \ll \epsilon_3 k_3^2 \ll k\beta$, approximate solutions of (5.9) are

$$D \sim \frac{ik\beta}{k_3^2} - \frac{\alpha f^2 n^2}{N^2 k_3^2} \quad , \quad -\epsilon_3 + i\epsilon_3 \frac{\alpha f^2 n^2}{k\beta N^2} \quad . \tag{5.11}$$

For this more moderate damping the advective mode is again strongly damped and westward propagating, while the Rossby solution is unchanged from the completely undamped case (see (3.21)). Unless the perturbation is shallow, the absorber damping rate must therefore exceed both the magnitude of the feedback rate and the internal Rossby wave frequency in order to reduce the growth rate of the Rossby mode. For shallow perturbations, the Rossby mode instability can be reduced for

absorber damping rates less than the magnitude of the feedback rate provided the damping rate exceeds the Rossby wave frequency.

While the preceeding analysis is revealing, it is restricted by the quasi-geostrophic assumption, which filters out gravity waves, and by the assumption of strong damping. Indeed, some of the most interesting behavior occurs when the damping rate is comparable to the feedback rate. In order to treat the effects of damping on the gravity modes, and to consider more moderate values of the damping rates, we shall now examine graphical illustrations of exact analytical solutions of (5.1).

Figure 5.1 shows the normalized growth rate of the advective mode as a function of the damping rate for a radiative-dynamical feedback rate of 10^{-5} s^{-1}, zonal and meridional wavelengths of 100 km, and a vertical wavelength of 10 km. Separate curves are shown for mechanical, thermal, and absorber damping. Consistent with the preceeding analysis, we see that mechanical damping actually increases the growth rate of the advective mode. However, as the mechanical damping rate exceeds the Coriolis frequency (10^{-4} s^{-1}), drag on the divergent part of the circulation becomes important. The quasi-geostrophic analysis loses validity, and the growth rate begins to decline with increasing mechanical damping. For thermal damping, the normalized growth rate declines to small values as the damping rate increases, consistent with the approximate solution. According to the exact solution, the growth rate becomes negligibly small only for thermal damping rates much larger than the radiative-dynamical feedback rate. Contrary to the approximate solution for absorber damping, the exact normalized growth rate becomes small and negative rather than large and negative as the absorber damping rate becomes much larger than the feedback rate. According to the approximate solution, the Rossby mode growth rate (for $\alpha > 0$) becomes small and negative for strong absorber damping, while the advective mode becomes large and negative. However,

the modes in the approximate solution were identified on the basis of the expressions for the frequency. While both approximate solutions indicate westward phase propagation, we have identified the Rossby mode as that mode which has about the same phase velocity as the Rossby mode in the absence of dissipation. In the exact analytical solution, the modes are identified on the basis of continuity with respect to lesser damping rates. That is, starting with small absorber damping, the advective and Rossby mode are easily identified; by slowly increasing the absorber damping rate, these modes are readily distinguished provided the two solutions of (5.9) remain distinct. However, if solutions intersect, it is not immediately obvious how the modes might be identified.

While the advective mode solution depicted in Figure 5.1 is distinguished from the Rossby mode for all absorber damping rates, under certain conditions the growth rate curves for the two solutions of (5.9) intersect. To determine these conditions, we first express the growth rate as $\mathrm{Re}(D) = D_1 \pm D_2$, where

$$D_2 = \mathrm{Re}\sqrt{h_r + ih_i} = \sqrt{\frac{h_r + \sqrt{h_r^2 + h_i^2}}{2}} \tag{5.12}$$

with

$$h_r = \left(\epsilon_3 k_3^2 - \alpha k_2^2\right)^2 - k^2\beta^2 \tag{5.13}$$

$$h_i = k\beta\left(2\epsilon_3 k_3^2 + 2\alpha k_2^2 - 4\alpha k_3^2\right) \quad . \tag{5.14}$$

The two growth rate curves will intersect if $D_2 = 0$, which occurs when $h_i = 0$ provided $h_r < 0$. The condition $h_i = 0$ determines the damping rate at which the two curves will intersect, namely, when

$$\epsilon_3 = \frac{2k_3^2 - k_2^2}{k_3^2}\,\alpha \quad . \tag{5.15}$$

Substituting (5.15) into (5.13), the condition that $h_r < 0$ becomes

$$\alpha < \frac{k\beta N^2}{2f^2 n^2} \quad . \tag{5.16}$$

Note that because the absorber damping rate is necessarily positive, (5.15) can only be satisfied for positive α.

Figure 5.2 shows the normalized growth rate of the advective and Rossby modes as functions of the absorber damping rate, for a feedback rate (1.2×10^{-6} s^{-1}) that almost satisfies condition (5.16). The two curves are seen to almost, but not quite, intersect; for a slightly smaller feedback rate the curves would intersect. Thus, one possible means of distinguishing which solution corresponds to the Rossby mode and which represents the advective mode would be to choose the same solution branch that corresponds to each mode when the curves do not intersect. That is, assume that the mode corresponds to the same branch independent of whether (5.16) is satisfied. This method, however, yields physically implausible choices for solution modes. For example, if there is no radiative-dynamical feedback, the Rossby mode neither grows nor decays as a result of absorber damping, while the advective mode, since it describes simple advection of the absorber in the absence of feedback, decays at the absorber damping rate. In this case (5.16) is satisfied, and the two solutions intersect at $\epsilon_3 = 0$; the upper branch corresponds to the Rossby mode, while the lower branch represents the advective mode. For larger positive feedback rates, the intersection point shifts toward larger ϵ_3, with the upper branch corresponding to the advective mode for weak damping, but the Rossby mode for strong damping. When the feedback rate is large enough so that (5.15) is no longer satisfied, the growth rate curves no longer intersect. The only possible conclusion then is that the upper branch represents the advective mode for absorber damping rate much less than the feedback rate, and the Rossby mode for absorber damping rate much greater than the feedback rate. For intermediate absorber damping rates, the distinction between the advective and Rossby modes is unclear; indeed, if (5.15) is satisfied and (5.16) is just barely satisfied, both the real and the imaginary parts of the two solutions are identical. For absorber damping rates that

differ substantially from the feedback rate, the physically most reasonable method of distinguishing modes is on the basis of frequency of oscillation: the Rossby mode is westward propagating, with a much higher phase speed than the advective mode.

Regardless of the nomenclature, we can conclude from the approximate solutions that strong absorber damping eliminates the instability if the feedback rate is positive, and greatly reduces it if the feedback rate is negative. From (5.9), one can show that if the absorber damping rate equals the feedback rate, one solution is $D = 0$, while the other solution is damped. Thus, for positive radiative-dynamical feedback there are no unstable solutions if the absorber damping rate exceeds the feedback rate. For moderate absorber damping and negative radiative-dynamical feedback, we must consider the exact analytical solution.

Figure 5.3 shows the normalized growth rate of the Rossby mode as a function of the damping rate for a radiative-dynamical feedback rate of -10^{-5} s^{-1}, zonal and meridional wavelengths of 10,000 km, and a vertical wavelength of 10 km. Separate curves are shown for mechanical, thermal, and absorber damping. Consistent with the preceeding analysis, we see that strong mechanical damping eliminates the instability of the Rossby mode. However, for mechanical damping rates much larger than the Coriolis frequency, the Rossby mode becomes more weakly damped rather than more strongly damped with increasing mechanical damping. This effect must be an ageostrophic effect, for it is neglected in the approximate analysis but included in the exact analytical solution of (5.1). Contrary to the approximate solution for strong thermal damping, the Rossby mode growth rate becomes small and negative rather than large and negative as the thermal damping rate becomes much larger than the magnitude of the feedback rate. This contradiction again reflects the transformation of a solution branch from a solution characterizing a Rossby mode to one characterizing an advective mode as the damping rate increases

from values much less than the magnitude of the feedback rate to values much larger than the feedback rate. In this case the two solutions of (5.6) intercept at

$$\epsilon_3 = -\left(1 + \frac{k_3^2 N^2}{f^2 n^2}\right) \alpha \tag{5.17}$$

if

$$|\alpha| < \frac{k\beta}{2k_3^2} \quad . \tag{5.18}$$

As in the case of absorber damping, the thermal damping rate given by (5.17) marks the transition from solutions that are characteristic of Rossby waves to those representative of advective modes, even if (5.18) is not satisfied, i.e., the two solutions do not intersect. For example, the solution illustrated in Figure 5.3 should be considered an advective mode rather than a Rossby mode for strong thermal damping ($\epsilon_3 \gg \alpha$), even though (5.18) is not satisfied for the wave scale considered. It is therefore impossible to illustrate the growth rate of what one would consider to be Rossby waves for all thermal damping rates without introducing a discontinuity; we have chosen to illustrate the growth rate of the solution that would be considered a Rossby wave for weak thermal damping, but an advective mode for strong thermal damping.

While we have been unable to determine approximate solutions for the growth rate of the inertia-gravity modes, the very large phase speeds of these waves makes the selection of the gravity mode growth rate from the exact solution of (5.1) rather simple. Thus, we can illustrate the exact solutions with confidence that what we are examining is in fact the inertia-gravity mode (although the two different gravity modes do not have identical growth rates in the presence of dissipation, the difference is small for all reasonable parameter values, so that concentrating on the growth rate of the fastest-growing gravity mode introduces little bias into the treatment). Figure 5.4 shows the normalized growth rate of the inertia-gravity mode as a function of the damping rate for a radiative-dynamical feedback rate

of -10^{-5} s^{-1}, zonal and meridional wavelengths of 1000 km, and a vertical wavelength of 10 km. Separate curves are shown for mechanical, thermal, and absorber damping. The gravity mode is seen to be most sensitive to mechanical damping, with the instability eliminated for a mechanical damping rate somewhat less than the magnitude of the feedback rate, and strongly damped for larger mechanical damping rates. Thermal damping is also rather efficient at removing the instability, with decay occurring when the thermal damping rate is somewhat greater than the magnitude of the feedback rate, and strong decay for larger thermal damping rates. Damping of the absorber concentration, however, is evidently inefficient at reducing the gravity-mode growth rate, with little change in the growth rate for absorber damping rates less than the Coriolis frequency.

To summarize, we have found that dissipative processes can damp modes that are otherwise unstable, or simply reduce the growth rates to negligible levels, or even enhance growth rates. Mechanical dissipation is effective at eliminating the instability of the gravity mode, with damping of the gravity mode for mechanical dissipation rates larger than the magnitude of the feedback rate. Mechanical dissipation is less effective for the Rossby mode, with the instability eliminated only when the dissipation rate dominates the feedback rate. For the advective mode, mechanical damping actually enhances the growth rate under certain conditions.

Thermal dissipation is nearly as efficient as mechanical damping in eliminating the instability of the gravity mode. The Rossby mode is also sensitive to thermal dissipation, with the instability eliminated when the thermal dissipation rate exceeds the magnitude of the feedback rate. Thermal dissipation is most efficient at reducing the growth rate of the advective mode for shallow perturbations, for which thermal dissipation rates that are much less than the feedback rate can reduce the instability provided the dissipation rate also dominates the internal Rossby wave frequency.

Absorber dissipation has little effect on the gravity mode growth rate unless the dissipation rate exceeds the Coriolis frequency. The effect of absorber dissipation on the growth rate of the Rossby mode is similar to the effect of thermal dissipation of the advective mode: the growth rate is reduced if the dissipation rate exceeds the internal Rossby wave frequency and the feedback rate, but for shallow waves lower absorber dissipation rates are sufficient to reduce growth rates provided the dissipation rate still exceeds the Rossby wave frequency. The advective mode is also sensitive to the absorber dissipation rate, with decay of the advective mode occurring for dissipation rates larger than the feedback rate.

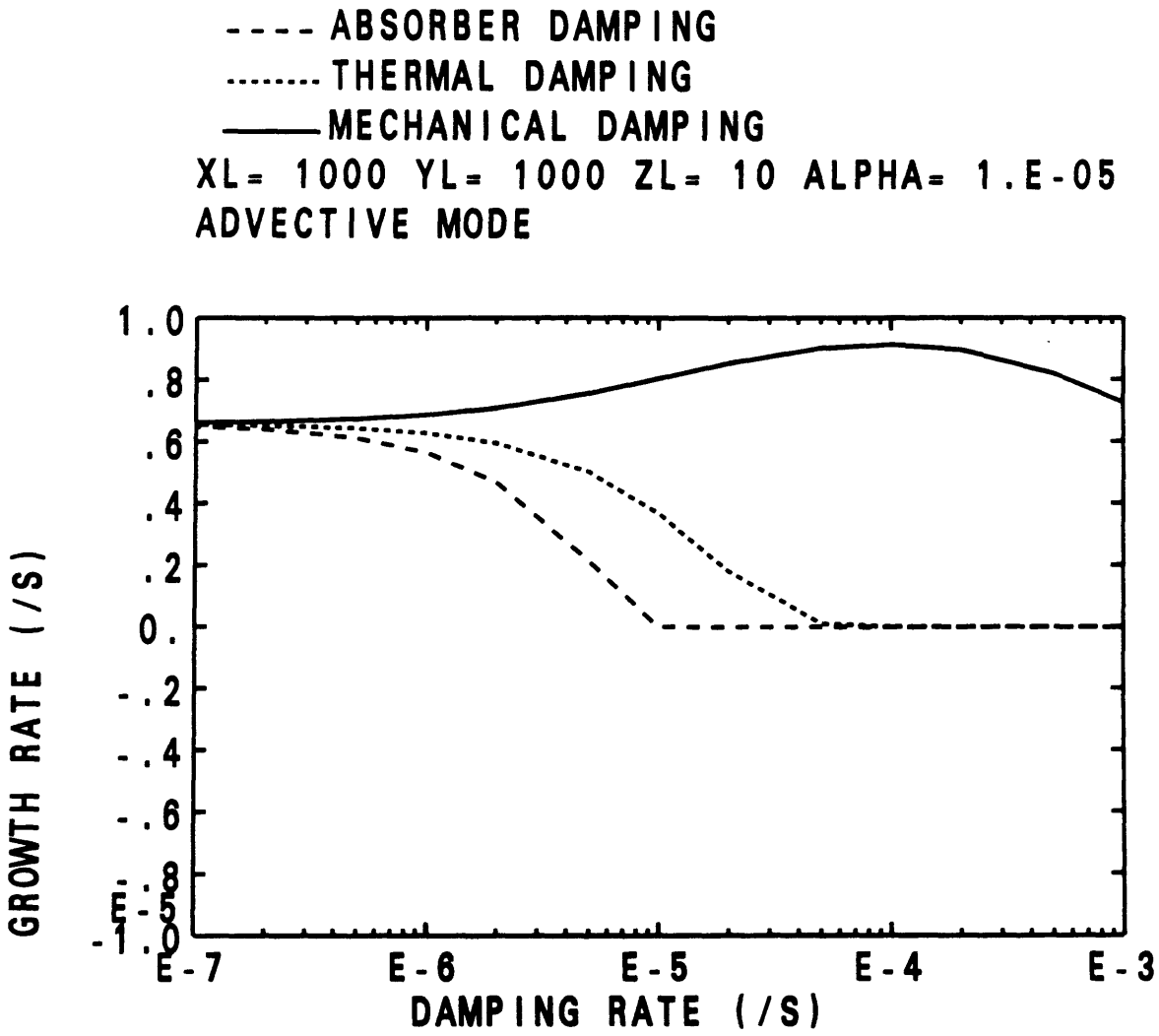

Figure 5.1. Advective mode growth rate as a function of damping rate for mechanical damping (solid line), thermal damping (short dashed line), and for absorber damping (long dashed line). The radiative-dynamical feedback rate is 10^{-5} s^{-1}. Midlatitude β-plane. The zonal and meridional wavelengths are 1000 km; the vertical wavelength is 10 km. The Brünt-Vaisala frequency is 10^{-2} s^{-1}; the density scale height is 8 km. Perturbations in transmissivity have been neglected.

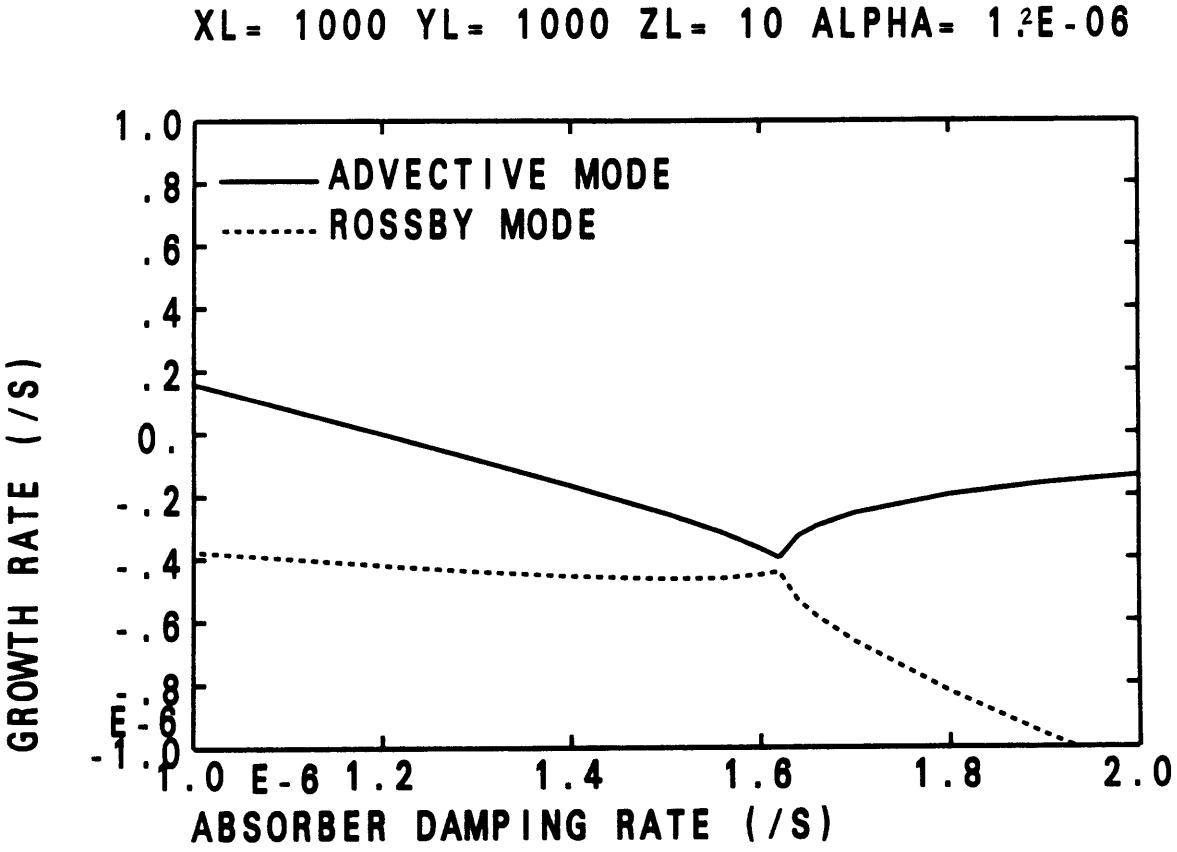

Figure 5.2. Growth rate of advective mode (solid line) and Rossby mode (dashed line) as functions of the absorber damping rate. The radiative-dynamical feedback rate is 1.2×10^{-6} s^{-1}. Otherwise, as in Figure 5.1.

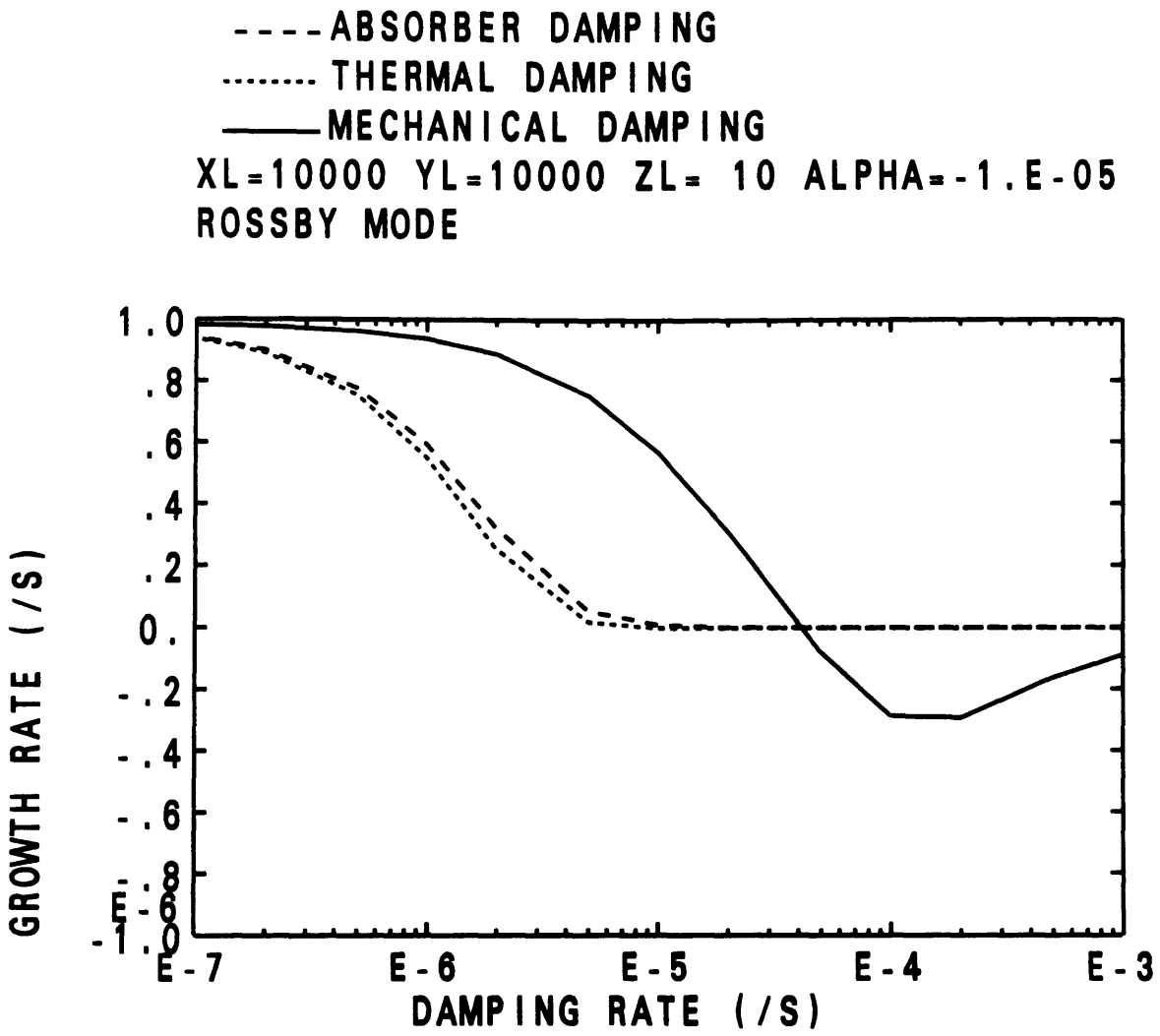

Figure 5.3. Rossby mode growth rate as a function of damping rate for mechanical damping (solid line), thermal damping (short dashed line), and for absorber damping (long dashed line). The radiative-dynamical feedback rate is -10^{-5} s^{-1}. The zonal and meridional wavelengths are 10,000 km. Otherwise as in Figure 5.1.

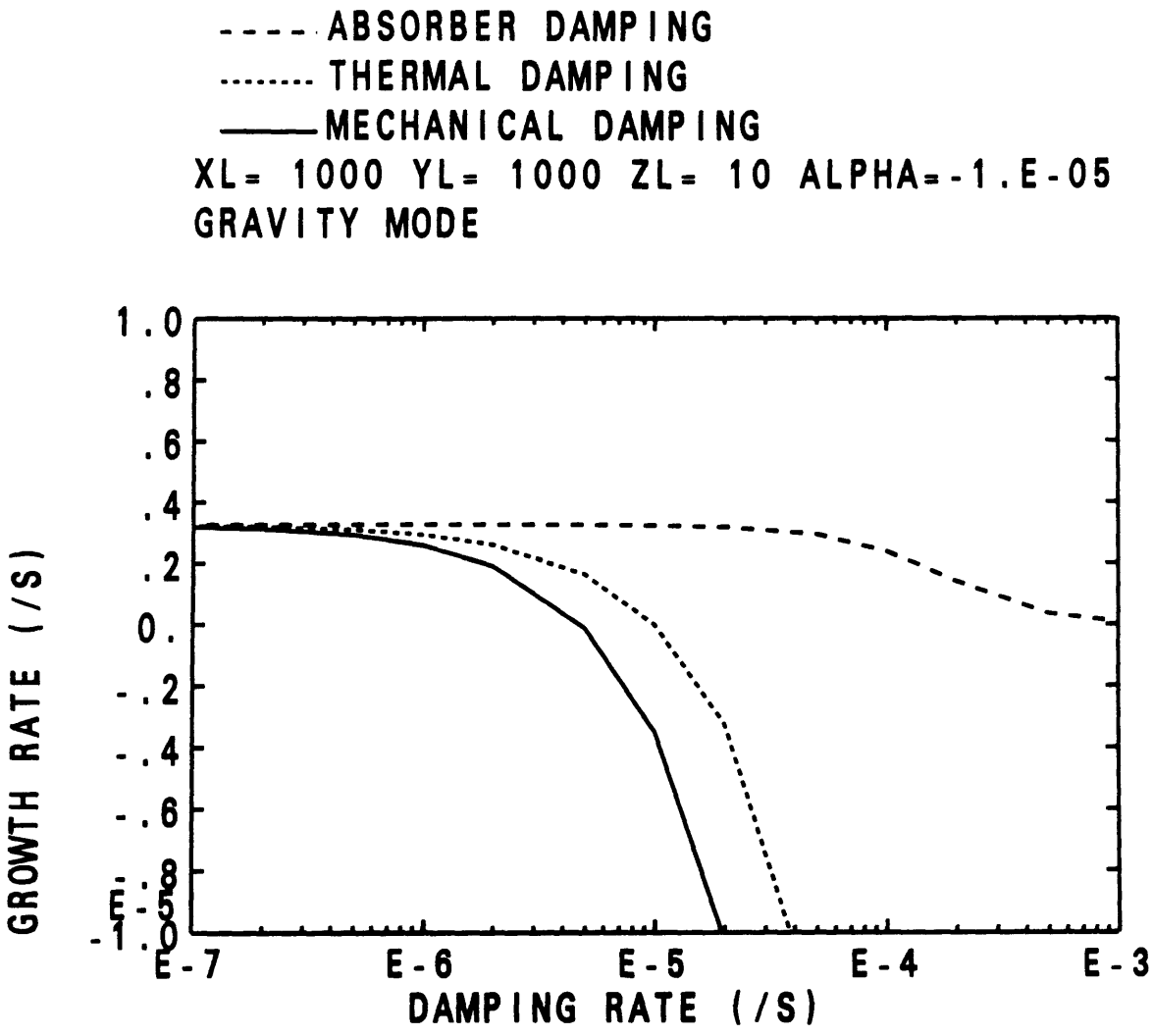

Figure 5.4. Gravity mode growth rate as a function of damping rate for mechanical damping (solid line), thermal damping (short dashed line), and for absorber damping (long dashed line). The radiative-dynamical feedback rate is -10^{-5} s^{-1} Otherwise as in Figure 5.1.

6. Effect of Nonuniform Basic State

The analysis up to this point has relied on the assumption that the basic state parameters of the problem are constant. In particular, the radiative-dynamical feedback rate, defined either with or without accounting for perturbations in the transmissivity, is assumed to be independent of altitude. With this assumption, and the usual assumptions that the density scale height and Brünt-Vaisala frequency are also constant, solutions to (3.12) of the form (3.14) reduce the differential equation to an algebraic relation for the complex eigenfrequency. While much information concerning the nature and parametric dependence of solutions has been derived from such an analysis, the assumption of constant feedback rate is generally valid only for a limited domain. If the radiative-dynamical feedback rate is constrained to be constant, one might expect that at some high altitude the basic state absorber concentration implied by such a constraint must become negative (for positive feedback) or unrealistically large (for negative feedback). This suggests that a more general treatment of the instability problem is required.

Before considering absorber distributions that produce feedback rates that are not constant, it is useful to consider the question of what absorber distributions yield feedback rates that are constant. If the resulting absorber distributions are unrealistic, we have a strong incentive to consider the more general problem. To simplify the problem, we shall neglect perturbations in the transmissivity ($\tau_H \ll 1$), an assumption that is reasonable provided the perturbations are sufficiently shallow or the absorption optical depth is sufficiently low. Assuming that the density scale height and Brünt-Vaisala frequency are also constant, the feedback rate

$$\alpha = -\frac{RS_0 a}{c_p N^2 H}\,\overline{T}\,\frac{d\overline{q}}{dz} \tag{6.1}$$

is constant if

$$\frac{d^2\overline{q}}{dz^2} + \frac{a\rho_0}{\mu}\,\overline{q}\,\frac{d\overline{q}}{dz} = 0 \quad . \tag{6.2}$$

To determine analytical expressions for the absorber distribution that satisfy (6.2), we shall assume that both the specific absorption a and the density ρ_0 are constant. Defining the non-dimensional measure of altitude, $\zeta = a\rho_0 z/\mu$, (6.2) becomes

$$\overline{q}'' = -\frac{1}{2}\left(\overline{q}^2\right)' \tag{6.3}$$

or, upon integration,

$$\overline{q}' = -\frac{1}{2}\,\overline{q}^2 + C \quad . \tag{6.4}$$

There are several possible solutions to (6.4). If $C = -2C_1^2$, then one solution of (6.4) is

$$\overline{q}(\zeta) = 2C_1 \tan\left(C_2 - C_1\,\zeta\right) \quad . \tag{6.5}$$

From (6.4) one finds that the absorber mixing ratio decreases with altitude for this case. However, (6.5) can only apply to finite atmospheres, in which the argument of the tangent varies by less than π. A second solution of (6.4) for $C = -2C_1^2$ is

$$\overline{q}(\zeta) = 2C_1\,\cot\left(C_1\zeta + C_2\right) \tag{6.6}$$

which is identical to (6.5) shifted by $\pi/2$.

If $C = 2C_1^2$, then two other solutions to (6.4) are

$$\overline{q}(\zeta) = 2C_1\,\coth\left(C_1\,\zeta + C_2\right) \tag{6.7}$$

and

$$\overline{q}(\zeta) = 2C_1\,\tanh\left(C_1\,\zeta + C_2\right) \quad . \tag{6.8}$$

Whereas (6.7) yields absorber distributions that again decrease with height, (6.8) applies to absorbers increasing with height. Both (6.7) and (6.8) yield positive absorber concentrations for semi-infinite as well as finite atmospheres, and hence

ought to prove more useful in representing the distribution of absorber mixing ratio. However, a semi-infinite atmosphere requires a realistic representation of density. Because we have assumed density to be constant in solving (6.2), our solutions are only formally valid for relatively shallow atmospheres. We shall now, therefore, consider numerical solutions of (6.2) for density decreasing exponentially with scale height H.

Figure 6.1 shows four vertical distributions of absorber mixing ratio determined from the numerical solution of (6.2), subject to the boundary conditions $\overline{q}(0) = 0$ and $\overline{q}_z(0) = 5 \times 10^{-12}$, 1×10^{-11}, 2×10^{-11} and 5×10^{-11} m^{-1}. The resemblance between the curves and the hyperbolic tangent solution of (6.8) is apparent, suggesting that variations in atmospheric density do not qualitatively alter the solutions. Note that because the hyperbolic tangent is bounded by unity, the solution (6.8) does not produce physically unreasonable distributions of absorber mixing ratio at high altitude. For the sake of quantitative accuracy, however, we shall use the numerical solution of (6.2) in subsequent calculations.

The radiative-dynamical feedback rates (as defined by (6.1)) corresponding to the four absorber distributions illustrated in Figure 6.1 are -1.23×10^{-6}, -1.46×10^{-6}, -1.32×10^{-6}, and -6.81×10^{-7} s^{-1} for the surface gradients $\overline{q}_z(0) = 5 \times 10^{-12}$, 1×10^{-11}, 2×10^{-11} and 5×10^{-11} m^{-1}, respectively, assuming a specific absorption coefficient of 1000 $m^2 kg^{-1}$, a solar constant of 1360 W m^{-2}, a solar zenith angle of 60°, and a Brünt-Vaisala frequency of 10^{-2} s^{-1} (the specific choice for the value of the absorption coefficient, though appropriate for smoke, is arbitrary in that the feedback depends only on the product $a\overline{q}$; the same feedback rates would therefore arise for different absorption coefficients if the basic state absorber mixing ratio is scaled accordingly). The numerical integration of (6.2) was only carried to an altitude of 30 km. Above this level, the mixing ratio is assumed to be constant; given the reduced atmospheric density at altitude, the error incurred by such a

treatment is small because for weak surface gradients in the absorber mixing ratio there is little attenuation of the solar beam, while for strong surface gradients the distribution rapidly approaches the asymptotic limit of the hyperbolic tangent and hence is consistent with the treatment of uniform mixing ratio above the model top. Note that the feedback rate is greatest for the intermediate surface absorber gradient, in which the absorption optical depth from the top of the atmosphere to the surface is roughly equal to the cosine of the solar zenith angle. This result is consistent with the analysis of the exponential distribution of absorber mixing ratio in the introduction, which does not guarantee a constant feedback rate.

According to the analysis for constant density, several solutions that preserve a constant feedback rate are possible when the absorber distribution decreases with altitude. Figure 6.2 shows two vertical distributions of absorber mixing ratio determined from numerical solutions of (6.2), subject to the boundary conditions $\overline{q}(0) = 10^{-6}$ and $\overline{q}_z(0) = -8 \times 10^{-10}$ m^{-1} and $\overline{q}_z(0) = -9 \times 10^{-10}$ m^{-1}. Although the boundary conditions for these two solutions are very similar, the distribution of absorber concentration at high altitudes is qualitatively different. When the surface gradient is weak, the mixing ratio approaches an asymptotic limit at high altitude, a characteristic in common with the hyperbolic cotangent in the analytical solution (6.7). When the surface gradient is sufficiently strong, however, the absorber mixing ratio becomes negative at high altitudes. This is a feature of the cotangent function in solution (6.6).

The radiative-dynamical feedback rates for these two solutions are also quite different. For the solution with the weaker surface gradient, the feedback rate is 4×10^{-8} s^{-1}, while for the stronger surface gradient the feedback rate is 4×10^{-6} s^{-1} (except at those altitudes at which the absorber mixing ratio is zero). These feedback rates differ so much, even at the surface where the surface gradients are

similar, because the transmissivity of the weak feedback solution is reduced by absorption at higher altitudes.

While the sensitivity of solutions illustrated in Figure 6.2 is most apparent when the absorber concentrations are strong, some sensitivity to surface absorber gradient persists for all absorber concentrations. To understand why, let us return to the analytical solution (6.7) for constant density. From (6.7), the absorber gradient is

$$\overline{q}_z = -\frac{2a\rho_0 C_1^2}{\mu} \operatorname{csch}^2 (C_1\ \zeta + C_2) \quad . \tag{6.9}$$

Solving for C_1 and C_2 in terms of $\overline{q}$ and $\overline{q}_z$, we find

$$4a\rho_0 C_1^2 = a\rho_0 \overline{q}^2 + 2\mu \overline{q}_z \tag{6.10}$$

$$C_2 = -C_1\ \zeta + \frac{1}{2} \ln \left(\frac{\overline{q} + 2C_1}{\overline{q} - 2C_1} \right) \quad . \tag{6.11}$$

Because solution (6.7) assumes C_1 is real (and positive), we can conclude from (6.10) that (6.7) is a solution only if

$$a\rho_0 \overline{q}^2 > -2\mu \overline{q}_z \quad . \tag{6.12}$$

Thus, if the boundary conditions of the solution do not satisfy (6.12), then (6.7) cannot be a solution. Rather, (6.6) or, equivalently, (6.5) is the solution, and a positive absorber mixing ratio cannot be guaranteed at all altitudes. From the specific absorption coefficient of 1000 $m^2\ kg^{-1}$ and an atmospheric density of 1 $kg\ m^{-3}$, we find that the transition between solutions (6.6) and (6.7) occurs at an absorber gradient of $-1 \times 10^{-9}\ m^{-1}$ for an absorber mixing ratio of 10^{-6}, in excellent agreement with the numerical solutions of Figure 6.2.

For stronger absorber gradients, the feedback rate is constant for only a finite region of the atmosphere. At those altitudes at which (6.2) predicts negative

absorber mixing ratio, we assume zero mixing ratio, and hence zero radiative-dynamical feedback. Thus, the feedback rate is piecewise uniform in altitude, with different values for two regions of the atmosphere:

$$\alpha = \begin{cases} \overline{\alpha} & z < z_t \\ 0 & z > z_t \end{cases} \quad . \tag{6.13}$$

By matching solutions at the boundary z_t between the two regions, we can determine the solution analytically at all levels. In the region with feedback the solution D is generally complex, and depends on $\overline{\alpha}$ and the horizontal and vertical scales of the perturbation. In the region without feedback the quasi-geostrophic dispersion relation becomes

$$\left(k_3^2 D - ik\beta\right) D = 0 \quad . \tag{6.14}$$

If the solution above z_t is to grow and propagate in phase with the solution below z_t, D must be the same for both regions. However, the vertical wavenumber need not be the same in both zones. Thus, above z_t the vertical wavenumber must satisfy

$$m^2 = \left(ik\beta/D - k_2^2\right) N^2/f^2 - \left(4H^2\right)^{-1} \tag{6.15}$$

with the constraint that the imaginary part of m must be positive to satisfy the upper boundary condition. Thus, solutions in the zone without feedback decay with distance away from the region with feedback. The (complex) amplitude of the solution in the neutral region is related to that of the region with feedback by the requirement that the real part of the solution for the vertical velocity and the pressure perturbation (or, by continuity, the derivative of the vertical velocity with respect to z), are continuous at z_t. The amplitude of the solution below z_t is of course arbitrary because this is a linear problem. It is important to note here that the solution below z_t is unaffected by the absence of feedback above z_t.

The foregoing analysis demonstrates that plausible basic state absorber distributions are consistent with a constant radiative-dynamical feedback rate at all altitudes. However, such ideal absorber distributions may not characterize an actual distribution with sufficient accuracy. Moreover, we have found that the range of possible feedback rates consistent with the ideal absorber distributions is limited if the constant feedback rate is to hold for the entire atmosphere. While stronger feedback rates can be considered over limited domains, the piecewise-continuous absorber distribution implied by such a treatment is probably unrealistic. To address more general problems with arbitrary absorber distributions, we therefore resort to numerical solutions of the eigenvalue problem.

In the previous local analyses with constant coefficients the eigenfunctions of the eigenvalue problem can be prescribed as in (3.14). For the more general problem with nonconstant coefficients, the eigenfunctions must be determined as part of the solution.

In the most general treatment of the problem the basic state would also vary horizontally; the horizontal eigenfunctions as well as vertical eigenfunctions would be determined as part of the solution. However, from the local analysis we have found that the most unstable modes are often those with the smallest horizontal scale. Thus, the most unstable modes of the numerical solution would be dominated by those with the smallest resolved scale, an unsatisfactory situation. To simplify the problem we shall therefore retain the assumption that all parameters of the problem are horizontally uniform. This allows the horizontal eigenfunctions to be prescribed, while the vertical eigenfunctions are determined numerically.

In order to treat the Rossby waves, it is necessary to consider the latitudinal variation of the Coriolis parameter. However, it is not possible to do so in a primitive equation numerical model without resorting to a two-dimensional (latitude-height) representation, with its associated horizontal resolution problems. On the

other hand, while a one-dimensional quasi-geostrophic treatment can treat the Rossby waves, it does not allow inertia-gravity waves and, according to the local analysis of the primitive equations, overestimates the growth rate of the advective mode when the feedback rate exceeds the Coriolis frequency. Thus, a one-dimensional model can either treat Rossby waves or gravity waves, but not both. Two types of one-dimensional models are therefore required, one that is quasi-geostrophic on a β-plane, the other that is based on the primitive equations on an f-plane. Between them, these models can accurately represent the Rossby, inertia-gravity, and advective modes for all feedback rates provided the Rossby wave frequency is less than the Coriolis frequency. In the tropics however, the Rossby wave frequency exceeds the Coriolis frequency, so that a two-dimensional model of the primitive equations on a β-plane or on a sphere is required. Given the horizontal resolution problems of such a model (and the overwhelming number of numerical eigenmodes), we shall not attempt to numerically treat tropical waves. Rather, we shall restrict our numerical solutions to the midlatitude synoptic scales using a one-dimensional model of the quasi-geostrophic equations on a β-plane. Although a model based upon the primitive-equations on an f-plane would also be useful, we shall not construct such a model here.

To solve an eigenvalue problem numerically, the equations with boundary conditions must be cast in the discrete form

$$\mathbf{A}\mathbf{x} = \sigma\mathbf{B}\mathbf{x} \tag{6.16}$$

where σ is the complex eigenvalue and $\mathbf{x}$ represents the corresponding eigenvector. For a model with N levels there are N eigenmodes. Many of these eigenmodes will be sensitive to the resolution of the model; a useful test for robustness is then that the eigenfrequency and eigenvector be insensitive to the resolution. Obviously if the most unstable modes are the shortest modes we have an unsatisfactory situation.

Fortunately, our local analysis in previous chapters indicates that the most unstable modes tend to be either intermediate in vertical scale or the largest resolved scale. While there will be some sensitivity to the model domain if the most unstable mode possesses the largest vertical scale, the sensitivity will be largely confined to the vertical scale, rather than the phase structure, of the most unstable mode.

The quasi-geostrophic numerical model is based upon the linearized quasi-geostrophic conservation equations for vorticity,

$$(D + \epsilon_u)\,\nabla^2\psi + \beta\psi_x = \frac{f_0}{\rho_0}\,\frac{\partial}{\partial z}\,(\rho_0 w) \tag{6.17}$$

potential temperature,

$$f_0\,(D + \epsilon_T)\,\psi_z - f\overline{u}_z\psi_x = -N^2 w + \frac{RQ}{c_p\rho_0 H} \tag{6.18}$$

and absorber mixing ratio,

$$(D + \epsilon_q)\,q = -\overline{q}_z w \tag{6.19}$$

where the radiative heating Q depends linearly on the absorber mixing ratio, either locally or at all altitudes.

To cast the model equations in the form (6.16), it is necessary to eliminate w from (6.17)–(6.19), yielding the quasi-geostrophic potential vorticity equation

$$\begin{aligned}(D + \epsilon_u)\,\nabla^2\psi + \beta\psi_x + D\,\frac{f_0^2}{\rho_0}\,\frac{\partial}{\partial z}\left(\frac{\rho_0\psi_z}{N^2}\right) + \frac{f_0^2}{\rho_0}\,\frac{\partial}{\partial z}\left(\frac{\rho_0\epsilon_T\psi_z}{N^2}\right)\\ -\psi_x\,\frac{f_0^2}{\rho_0}\frac{\partial}{\partial z}\left(\frac{\rho_0\overline{u}_z}{N^2}\right) - \frac{f_0}{\rho_0}\frac{\partial}{\partial z}\left(\frac{RQ}{c_pN^2H}\right) = 0\end{aligned} \tag{6.20}$$

and an absorber-potential temperature equation

$$(D + \epsilon_q)\,q - \frac{f_0\overline{q}_z}{N^2}\,(D + \epsilon_T)\,\psi_z - \frac{f_0\overline{q}_z}{N^2}\overline{u}_z\psi_x + \frac{R\overline{q}_z Q}{c_p\rho_0 N^2 H} = 0 \quad . \tag{6.21}$$

Equations (6.20) and (6.21) constitute the required two equations for the two unknowns ψ and q (the dependence of the heating on the distribution of q is also included of course, but has not been expressed in (6.20) and (6.21)).

Because ψ is twice differentiated with respect to z, two boundary conditions on ψ are required to close the problem. These are the usual boundary conditions employed in adiabatic problems, namely that the thermodynamic balance is satisfied at the surface and at the top of the model atmosphere, with no vertical motion at each boundary. Such a boundary condition at the model top, although convenient, is purely artificial. As discussed at the end of Chapter 3, a lid placed at a finite top restricts the vertical wavenumber m to one of a discrete set. This constraint will be clearly evident in the numerical solutions for uniform radiative-dynamical feedback. It is important to note here that, because the energy source is uniform for uniform feedback (neglecting perturbations in transmissivity), such solutions are identical to solutions for a semi-infinite atmosphere with the same uniform feedback and vertical wavenumber. Indeed, from the analysis earlier in this chapter of an atmosphere with uniform feedback below a level z_t and zero feedback above z_t, we conclude that the region above level z_t affects the vertical structure of the solution above z_t but not the eigenvalue or the vertical structure of the solution below z_t. Thus, for uniform feedback the only problem caused by the artificial lid is the restriction to the discrete set of vertical wavenumbers. This is only a serious problem when the most rapidly amplifying modes are either much deeper than the model domain or much shallower than the model grid spacing.

Assuming solutions of the form $\exp(ikx+ily-i\sigma t)$ and applying (6.20), (6.21), and the boundary conditions on a staggered grid with second-order accurate finite differences, yields the eigenvalue problem of the correct form (6.16). Details are given in Appendix B. Because the only requirement for the perturbation heating is that it depend linearly on the absorber mixing ratio, the restriction to a purely absorbing constituent is no longer necessary. In fact, in Chapter 8 a delta-Eddington model is used to represent the solar heating, thus permitting treatment of the effects of scattering by the absorber.

To lay the groundwork for consideration of arbitrary basic state absorber distributions, and to test the numerical model for accuracy, we first consider numerical solutions for absorber distributions that yield uniform feedback rates. Figure 6.3 shows the most unstable solution for a zonal wavelength of 10,000 km, a meridional wavelength of 1000 km, and an absorber distribution that yields a feedback rate of 1×10^{-6} s^{-1}. The values for the solar constant, solar zenith angle, specific absorption coefficient, and Brünt-Vaisala frequency are the same as above, and vertical shear, damping, and perturbations in the transmissivity have all been neglected. For these parameter values the growth rate is 9.6×10^{-7} s^{-1}, only slightly less than the feedback rate. The frequency is 9.9×10^{-9} s^{-1}, much less than the growth rate, a feature indicative of the advective mode. The absorber amplitude is small near the boundaries (a feature required by the boundary conditions), while the absorber phase is nearly constant with altitude, indicating a standing mode associated with the cancellation of the phases in upward and downward propagating modes of equal amplitude and vertical scale. Consistent with the local analysis, the vertical scale of this most rapidly amplifying mode is clearly the largest that can be resolved by the model (smaller vertical scales would be marked by rapid 180° shifts in the phase at periodic altitudes). The transport of both potential temperature and absorber is upward, so that the absorber gradient is reduced and potential energy is released by the perturbation.

When perturbations in transmissivity are accounted for the effective radiative-dynamical feedback parameter α_e becomes complex. The analysis of Chapter 4 demonstrates that, unless the imaginary part of the effective feedback rate is comparable to the external Rossby wave frequency, the growth rate depends only on the real part of the effective feedback rate. Because the real part of the effective feedback rate decreases to zero as $2n^2H^2$ decreases to τ_H, the growth rate of the deeper modes is reduced by perturbations in transmissivity. The most rapidly amplifying

mode would then be a mode with a somewhat reduced vertical scale. Figure 6.4 shows the most rapidly amplifying numerical solution for the same parameter values as were used for the calculations of Figure 6.3, but this time with perturbations in transmissivity accounted for. For these parameter values α is much greater than the external Rossby frequency, so that if perturbations in transmissivity are important the imaginary part of the effective feedback rate, α_i, will also dominate the external Rossby frequency. Thus, as expected the vertical scale of the most rapidly amplifying solution is reduced by perturbations in transmissivity, in this case to about half of that without accounting for perturbations in transmissivity. Also as expected, the growth rate has been reduced, from 9.6×10^{-7} s^{-1} to 8.0×10^{-7} s^{-1}. The frequency, on the other hand, has been greatly increased, from 1×10^{-8} s^{-1} to 1.2×10^{-7} s^{-1}, reflecting the strong influence of the imaginary part of the effective feedback rate on the propagation of the advective mode. In addition, the phase structure has changed from that of a standing mode to that dominated in the interior by a single upward and eastward propagating mode. This occurs because, according to (4.19), the sign of the imaginary part of the feedback parameter depends on the sign of the vertical wavenumber. Because the eigenfrequency of the advective mode is strongly influenced by the imaginary part of the effective feedback rate when perturbations in transmissivity are important, only one vertical wavenumber is consistent with a given eigenfrequency. Standing modes are not, therefore, consistent solutions in this case. The vertical structure of the phase is dominated, at least in the interior, by that of the mode with vertical wavenumber consistent with the eigenfrequency. Although it is unclear how a single mode can satisfy the boundary conditions, it is equally unclear how two modes, both of which propagate upward (which is the case for the advective mode when perturbations in transmissivity are important), can also satisfy the boundary conditions.

According to the local analysis, the Rossby mode growth rate for negative radiative-dynamical feedback is greatest for intermediate vertical scales. Figure 6.5 shows the most rapidly amplifying solution for an absorber distribution that yields a uniform feedback rate of -1.4×10^{-6} s^{-1}, and zonal and meridional wavelengths of 3000 km. Vertical shear, damping, and perturbations in the transmissivity have again all been neglected. The growth rate for the numerical solution is 5.3×10^{-7} s^{-1}; the frequency is -1.6×10^{-6} s^{-1}, comparable to the feedback rate, but greater than the growth rate. The vertical wavelength is evidently about 15 km, with negligible vertical variations in the phase except at the nodes of the amplitude. According to local theory, the growth rate and frequency of the Rossby mode with these spatial scales are 5.5×10^{-7} and -1.6×10^{-6} s^{-1}, respectively, in excellent agreement with the numerical solution. Consistent with local theory, vertical absorber transport is downward (i.e., down the basic-state absorber gradient), while potential temperature transport is upward for release of potential energy. Because the optical depth through one vertical wavelength of this mode is small, the most unstable solution that accounts for perturbations in the transmissivity is nearly identical to that illustrated in Figure 6.5. For zonal and meridional scales that yield most rapidly amplifying solutions that are optically thick, accounting for the transmissivity reduces the vertical scale of the fastest growing mode. Although the local analysis of Chapter 4 concludes that under certain conditions the growth rate of the downward-propagating mode can be enhanced by perturbations in the transmissivity, the growth rate of the corresponding upward-propagating mode is reduced; because solutions satisfying the boundary conditions must include both an upward- and a downward-propagating mode, the growth rate of solutions with the same vertical scale is generally reduced by perturbations in the transmissivity.

Now that we have some confidence in the ability of the model to reproduce the results of the local theory when the coefficients of the problem are constant

with altitude, we shall apply the model to problems in which the coefficients, in particular the radiative-dynamical feedback rate, are nonuniform.

One plausible vertical distribution of absorber is the exponential profile, in which the absorber mixing ratio decreases exponentially with scale height h. As an example of a case in which the feedback rate is strong enough to compete with baroclinic instability, but is largely confined to the lower atmosphere, Figure 6.6 shows the radiative-dynamical feedback rate as a function of altitude, calculated (neglecting perturbations in transmissivity) from an absorber distribution with a surface maximum of 10^{-6} and a scale height of 10 km. The usual values for the solar constant, etc., have been adopted. Perturbations in the transmissivity are accounted for. The maximum feedback rate is about 7×10^{-6} s^{-1}, and occurs at an altitude of about 15 km. Consistent with the analysis of Chapter 1, this is the altitude at which the absorption optical depth equals the cosine of the solar zenith angle. The distribution is seen to be quite broad, with a half-width of about 15 km. Figure 6.7 shows the numerical solution of the most rapidly amplifying eigenmode for the exponential absorber distribution used for Figure 6.6 and for a zonal wavelength of 10,000 km and a meridional wavelength of 1000 km [these spatial scales are chosen to minimize the Rossby wave frequency, and hence maximize the vertical scale selectivity of the solution—see the discussion regarding (3.23)]. The growth rate for this mode is 3.9×10^{-6} s^{-1}, corresponding to an e-folding time of about 3 days. The absorber amplitude is evidently modulated by the feedback distribution, while the phase structure is very similar to the constant feedback solution (see Figure 6.4).

For steeper gradients in the basic state absorber distribution, the maximum feedback rate is larger, but the strong feedback is confined to a narrower region. Figure 6.8 shows the feedback rate for a surface absorber mixing ratio of 3×10^{-6} and an absorber scale height of only 3 km. The maximum feedback rate is now

2.2×10^{-5} s^{-1}, but the half-width of the feedback distribution is less than 10 km. The most rapidly amplifying modes must therefore be quite shallow. Because the maximum feedback rate is much larger than the Rossby frequency for planetary-scale perturbations, the growth rate of such shallow planetary-scale modes must be, according to the local analysis, much less than the maximum feedback rate. Thus, the growth rate of the most rapidly growing mode with zonal wavelength 10,000 km and meridional wavelength 1000 km is only 6.4×10^{-6} s^{-1}, much less than the maximum feedback rate of 2.2×10^{-5} s^{-1}. However, for perturbations with sufficiently small zonal and meridional scales, $k_2^2 \simeq k_3^2$ even for shallow modes. The growth rate for such short, shallow modes can therefore be comparable to the maximum feedback rate. For example, Figure 6.9 shows the numerical solution of the most rapidly amplifying mode corresponding to the feedback rate illustrated in Figure 6.8 and zonal and meridional wavelengths of 100 km. The growth rate for this mode is 2.0×10^{-5} s^{-1}, corresponding to an e-folding time of about 15 hours, and nearly equal to the maximum feedback rate. The phase has little vertical structure near the boundaries where the absorber amplitude is small, but increases rapidly with height at altitudes near the maximum amplitude.

As discussed in Chapter 4, unless the imaginary part of the effective feedback rate is comparable to the external Rossby wave frequency, the growth rate depends only on the real part of the effective feedback rate, while the sign of the eigenfrequency of the advective mode depends on the sign of the imaginary part of the effective feedback rate. Because the sign of the imaginary part of the effective feedback rate depends on the sign of the vertical wavenumber, eigenmodes dominated by vertical wavenumbers of opposite sign will have eigenfrequencies of opposite sign. To illustrate this point, Figure 6.10 shows the solution for the second most rapidly amplifying mode for the same conditions as in Figure 6.9. For these parameter values the imaginary part of the effective feedback rate dominates

the external Rossby wave frequency, so that (4.20) is not satisfied for either positive or negative vertical wavenumber. The growth rate of this mode is nearly as large as that of the most rapidly growing mode, but the frequency is of opposite sign. The phase structure is similar to that illustrated in Figure 6.9, except that at levels of large amplitude the phase decreases rather than increases rapidly with height. Thus, the second most rapidly amplifying solution is dominated by a vertical wavenumber of sign opposite to that of the most rapidly growing solution. The sign of the frequency of these solutions is therefore opposite, while the growth rate is nearly identical. Both modes are characterized by upward phase propagation; one solution propagates westward, while the other propagates eastward.

A second plausible absorber distribution is the Gaussian, which has a local maximum mixing ratio and hence yields regions of positive and negative radiative-dynamical feedback. Such a distribution approximates the distribution of stratospheric ozone mixing ratio, and might apply to injections of aerosols from volcanoes or fires. As an example which yields strong negative and positive feedback confined to the interior of the model atmosphere, Figure 6.11 shows the feedback distribution for a Gaussian absorber distribution with maximum mixing ratio 10^{-7} at 15 km and a standard deviation of 5 km. The usual values of the solar constant, etc., have been used. The feedback is seen to be quite weak near the boundaries. Because of the reduction of the mean transmissivity with depth, the feedback maximum (5.6×10^{-6} s^{-1}) is somewhat larger in magnitude than the feedback mimimum (-4.0×10^{-6} s^{-1}).

Given such a feedback distribution, an obvious question is the following: do unstable modes exist for each region of the atmosphere, or do the regions with positive and negative feedback cancel? Figure 6.12 shows the most rapidly amplifying solution for the feedback distribution of Figure 6.11 and zonal and meridional wavelengths of 1000 km. The amplitudes in the region with positive feedback dominate

those in the region with negative feedback. Absorber transport is upward where the absorber mixing ratio decreases with altitude, and weakly downward where the mixing ratio increases with altitude. Consistent with these features, the growth rate (4.3×10^{-6} s^{-1}) dominates the frequency (1.5×10^{-7} s^{-1}), indicative of an essentially advective mode instability.

Other modes can be characterized as Rossby modes. Figure 6.13 shows the vertical structure of the 15^{th} (of 61) most rapidly amplifying solution for the same case as in Figure 6.12. The amplitudes are largest in the region with negative radiative-dynamical feedback. Absorber transport is primarily downward. Consistent with the Rossby mode of instability, propagation is westerly, with a frequency $\sigma_r = -7 \times 10^{-7}$ s^{-1}, while the growth rate is smaller, $\sigma_i = 3.1 \times 10^{-7}$ s^{-1}. The phase structure is suggestive of energy propagation away from the energy source, i.e., the region of instability. Thus, we conclude that unstable modes exist in both regions, with the structure of each mode consistent with the sign of the local radiative-dynamical feedback.

In summary, while we have found plausible absorber distributions that yield constant feedback rates, these distributions cannot possibly apply to all situations. However, we have found that many of the features of numerical solutions for more general absorber distributions can be explained on the basis of the theory developed for uniform feedback. Thus, the local theory has proven to be a valuable tool in understanding more complex problems involving radiative-dynamical interactions.

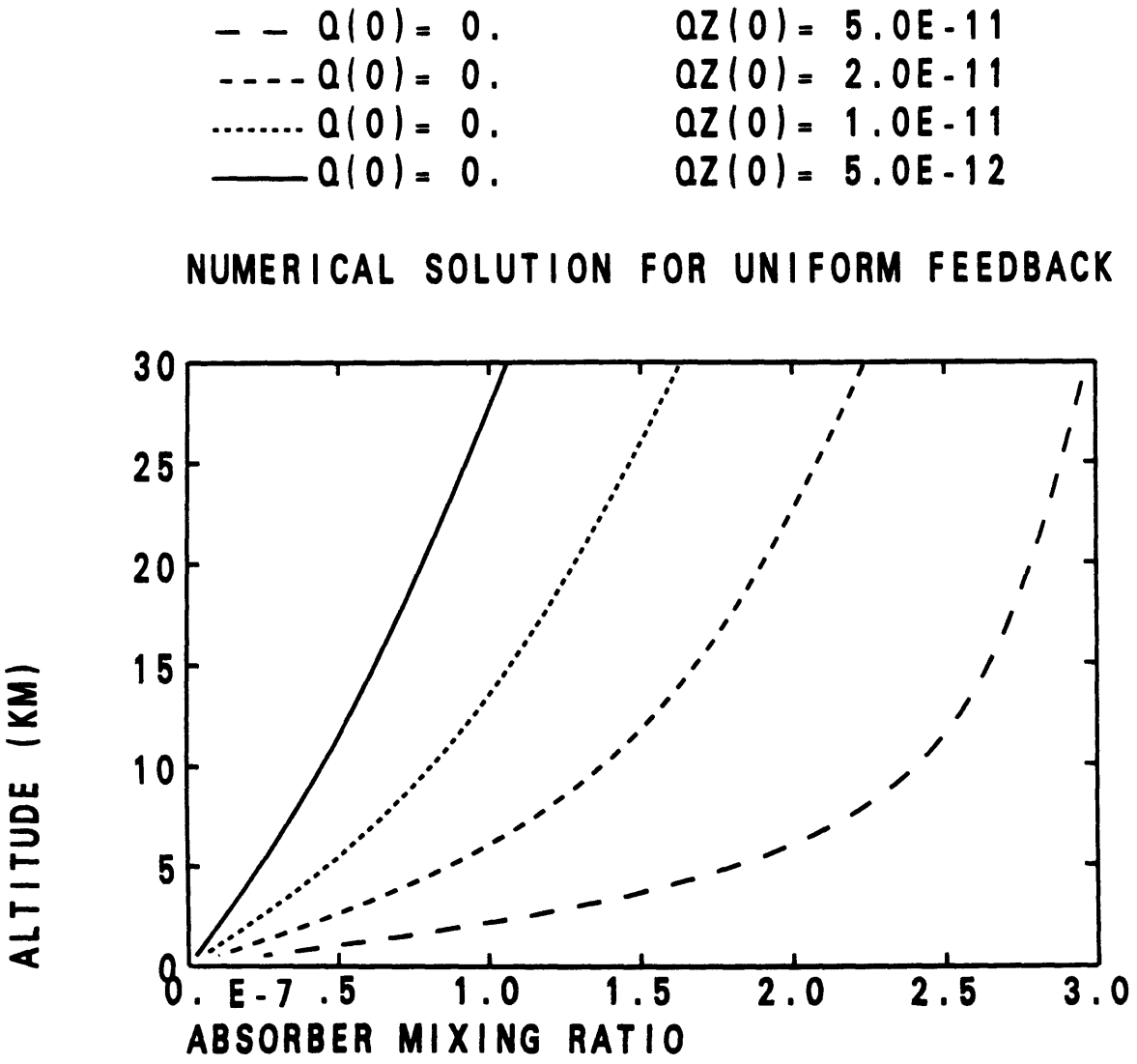

Figure 6.1. Vertical distribution of basic state absorber mixing ratio that yields a uniform radiative-dynamical feedback rate, for a zero surface mixing ratio and vertical gradients at the surface of 5×10^{-12} m^{-1} (solid line), 1×10^{-11} m^{-1} (short dashed line), 2×10^{-11} m^{-1} (medium dashed line), and 5×10^{-11} m^{-1} (long dashed line). The specific absorption coefficient is assumed to be 1000 m^2 kg^{-1}, the solar zenith angle 60°, and the density scale height 8 km.

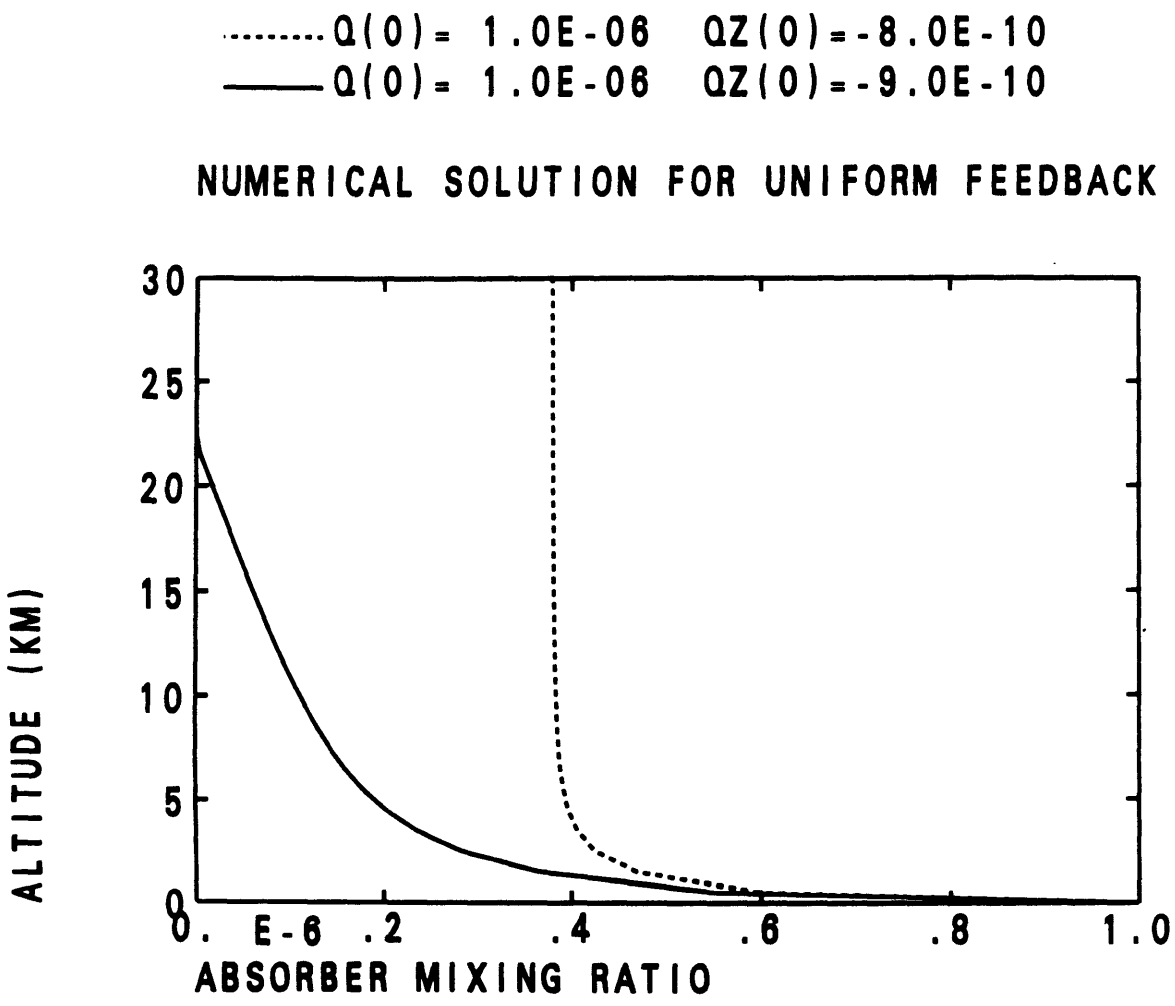

Figure 6.2. Vertical distribution of basic state absorber mixing ratio that yields a uniform radiative-dynamical feedback rate, for a surface mixing ratio of 10^{-6} and vertical gradients at the surface of -9×10^{-10} m^{-1} (solid line) and -8×10^{-10} m^{-1} (dashed line). Otherwise as in Figure 6.1.

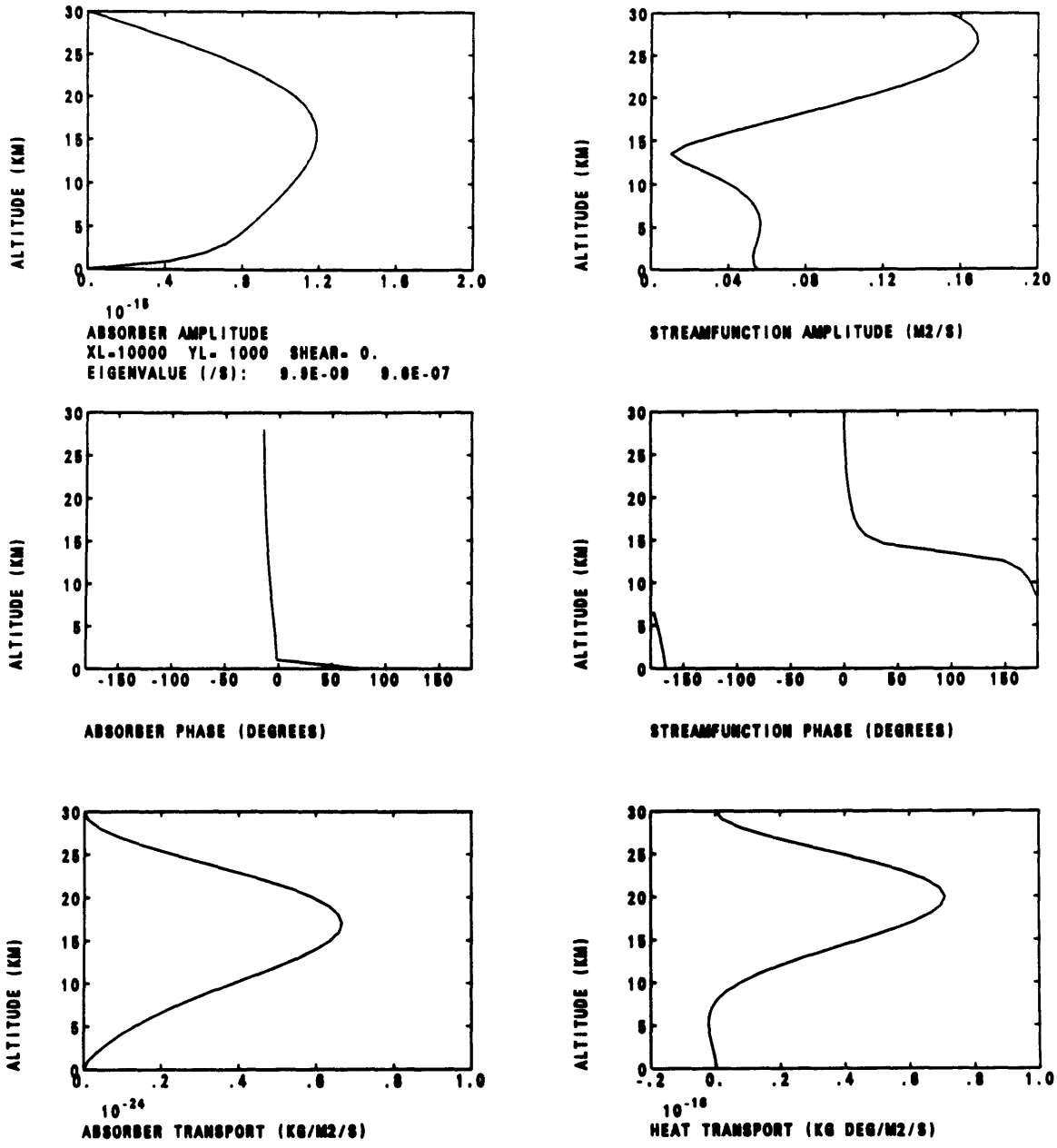

Figure 6.3. Vertical structure of the most rapidly amplifying eigenmode for a zonal wavelength of 10,000 km, a meridional wavelength of 1000 km, and a basic state absorber distribution giving a uniform radiative-dynamical feedback rate of $\alpha_0 = 10^{-6}$ s^{-1}. Based on the numerical solution of the eigenvalue problem for quasi-geostrophic radiative-dynamical interaction. Amplitudes are weighted by $\exp(-z/(2H))$ to account for conservation of wave energy during vertical propagation. Absorber transport is $\rho_0 w^* q^*$; heat transport is $\rho_0 w^* \theta^*$. The solar constant is 1360 W m^{-2}, the solar zenith angle is 60°, the specific absorption coefficient is 1000 m^2 kg^{-1}, and the constant Brünt-Vaisala frequency is 10^{-2} s^{-1}. Vertical shear, dissipative effects, and perturbations in transmissivity have all been neglected.

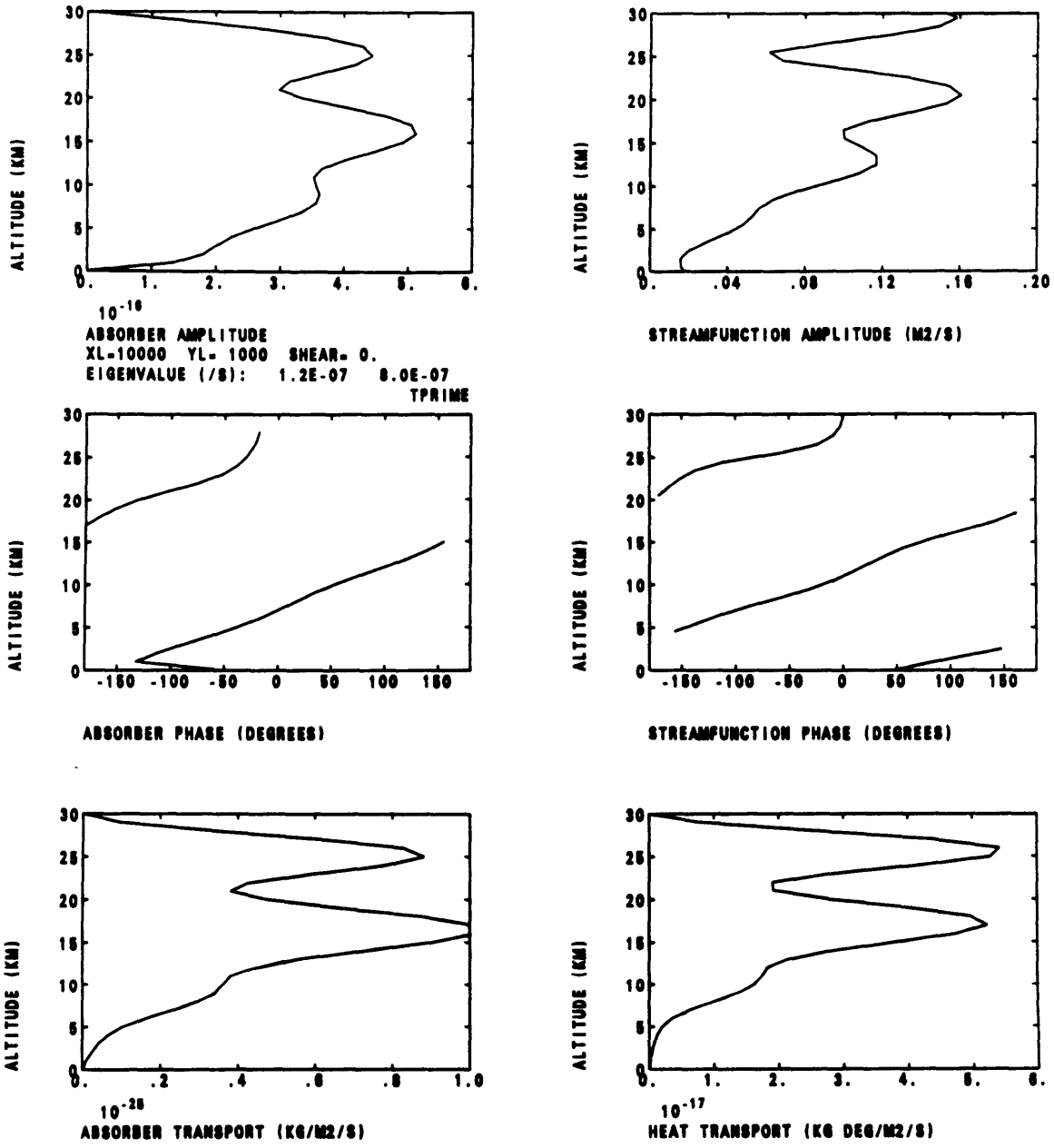

Figure 6.4. As in Figure 6.3, but with perturbations in transmissivity accounted for.

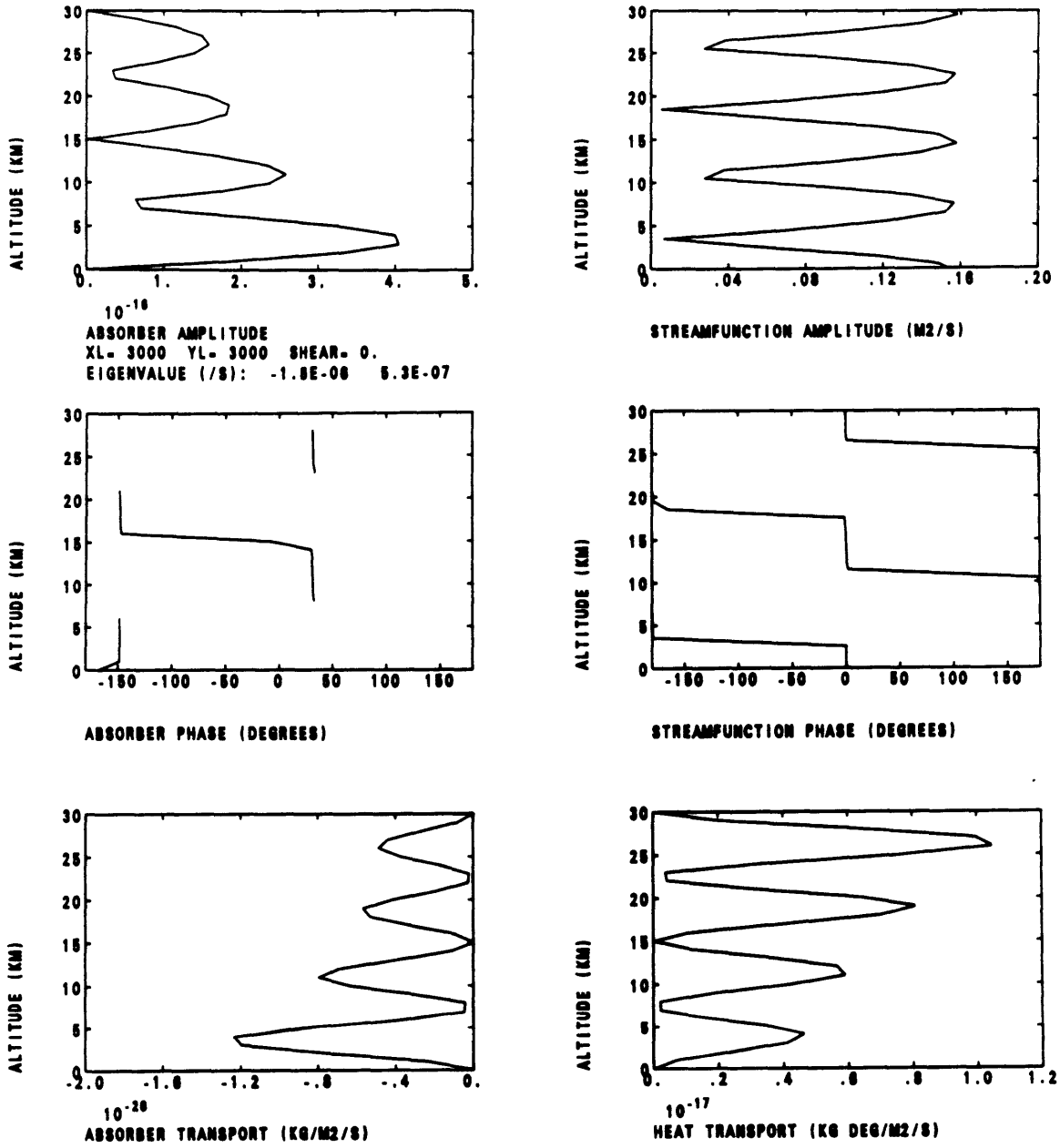

Figure 6.5. Vertical structure of the most rapidly amplifying eigenmode for zonal and meridional wavelengths of 3000 km and an absorber distribution that yields a uniform radiative-dynamical feedback rate of -1.4×10^{-6} s^{-1}. Perturbations in transmissivity are accounted for. Otherwise as in Figure 6.3.

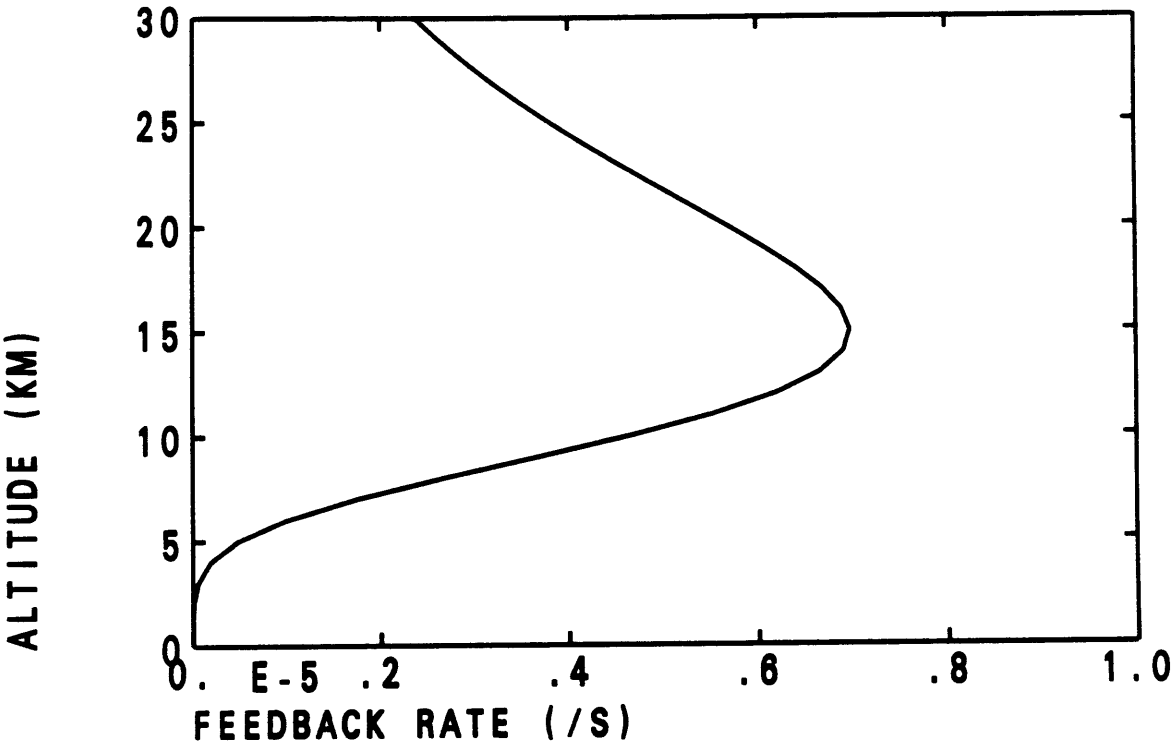

Figure 6.6. Radiative-dynamical feedback rate α_0 as a function of altitude for an exponential absorber distribution with a surface maximum of 10^{-6} and a scale height of 10 km. The solar constant is 1360 W m^{-2}, the solar zenith angle is 60°, the specific absorption coefficient is 1000 m^2 kg^{-1}, and the constant Brünt-Vaisala frequency is 10^{-2} s^{-1}.

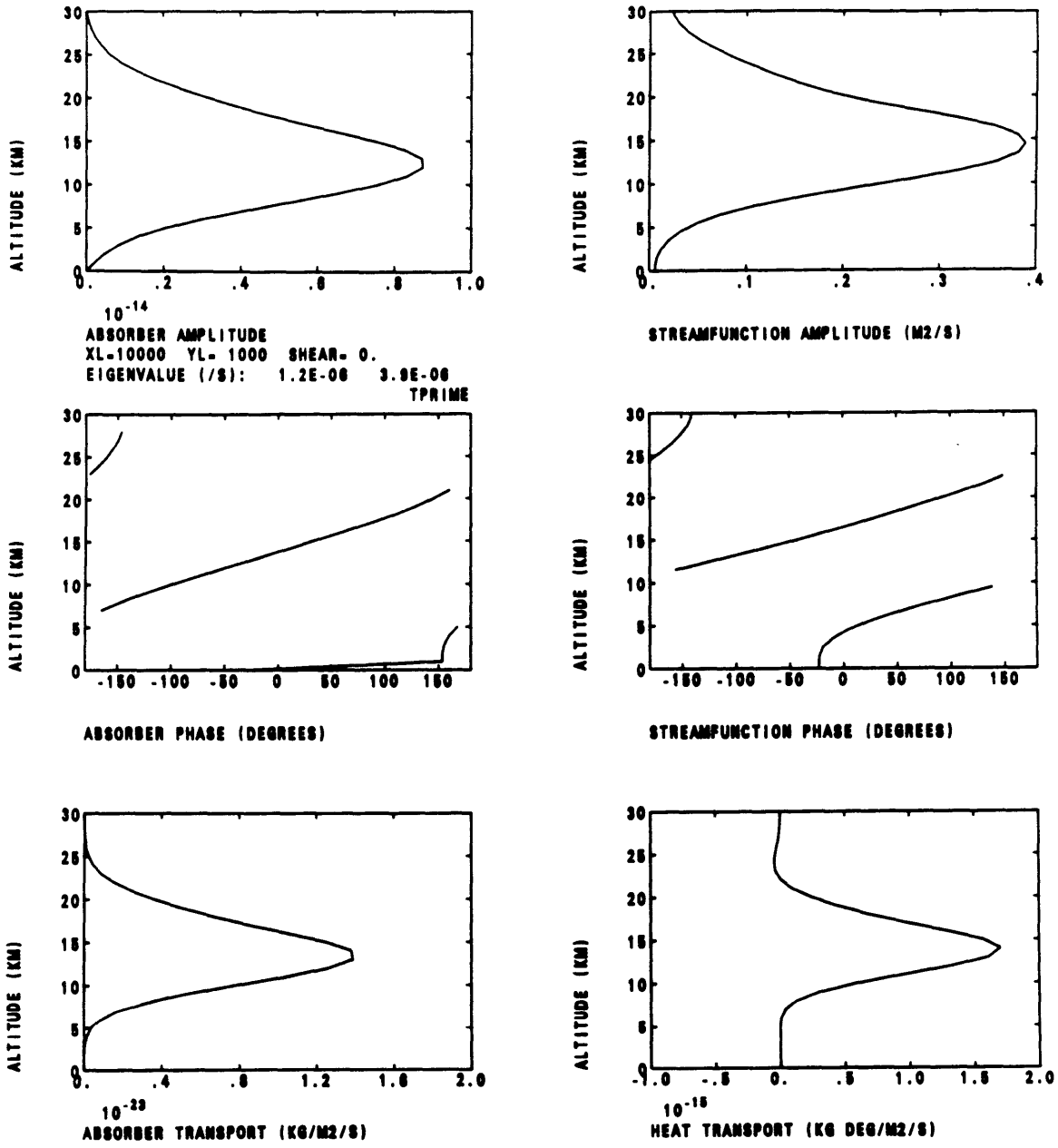

Figure 6.7. Vertical structure of the most rapidly amplifying eigenmode for a zonal wavelength of 10,000 km, a meridional wavelength of 1000 km, and the exponential absorber distribution used in Figure 6.6. Perturbations in transmissivity are accounted for. Otherwise, as in Figure 6.3.

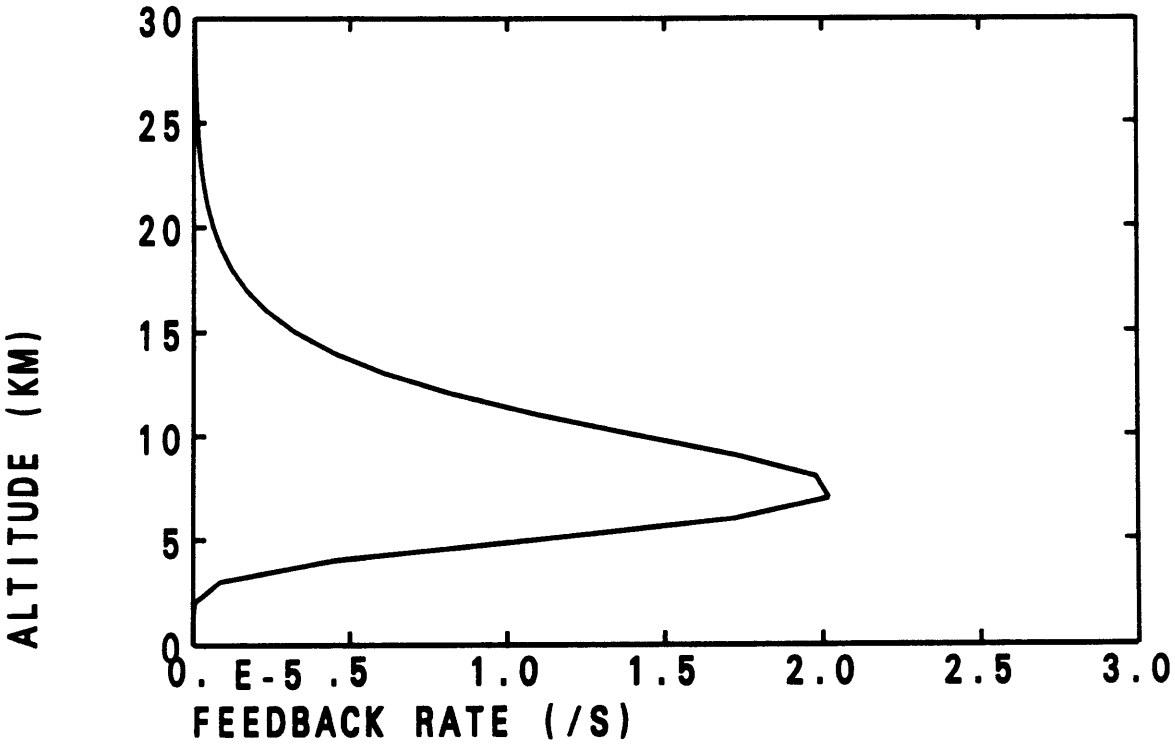

Figure 6.8. Radiative-dynamical feedback rate α_0 as a function of altitude for an exponential absorber distribution with a surface maximum of 3×10^{-6} and a scale height of 3 km. Otherwise as in Figure 6.6.

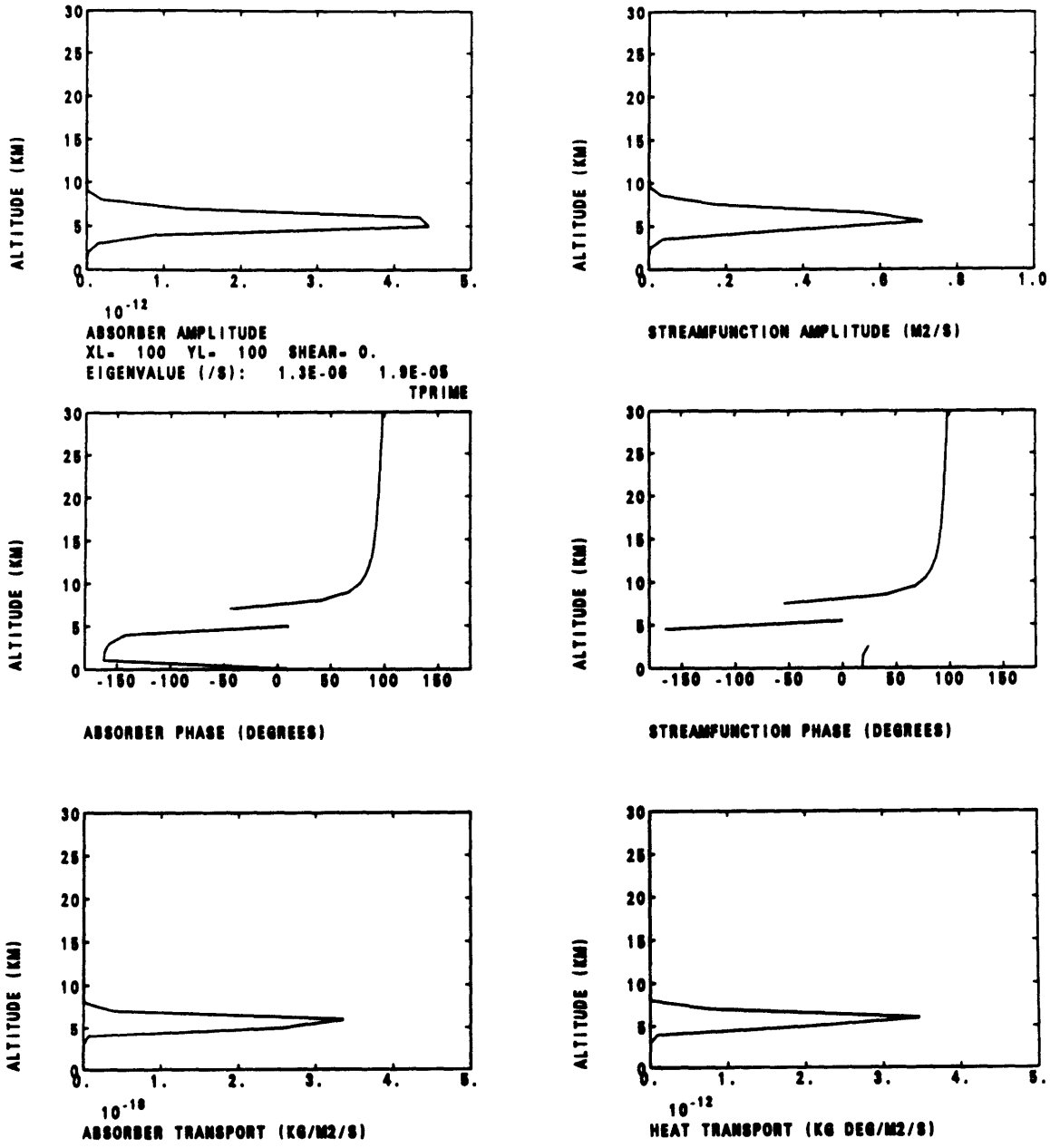

Figure 6.9. Vertical structure of the most rapidly amplifying eigenmode for zonal and meridional wavelengths of 100 km and the exponential absorber distribution used in Figure 6.8. Perturbations in transmissivity are accounted for. Otherwise, as in Figure 6.3.

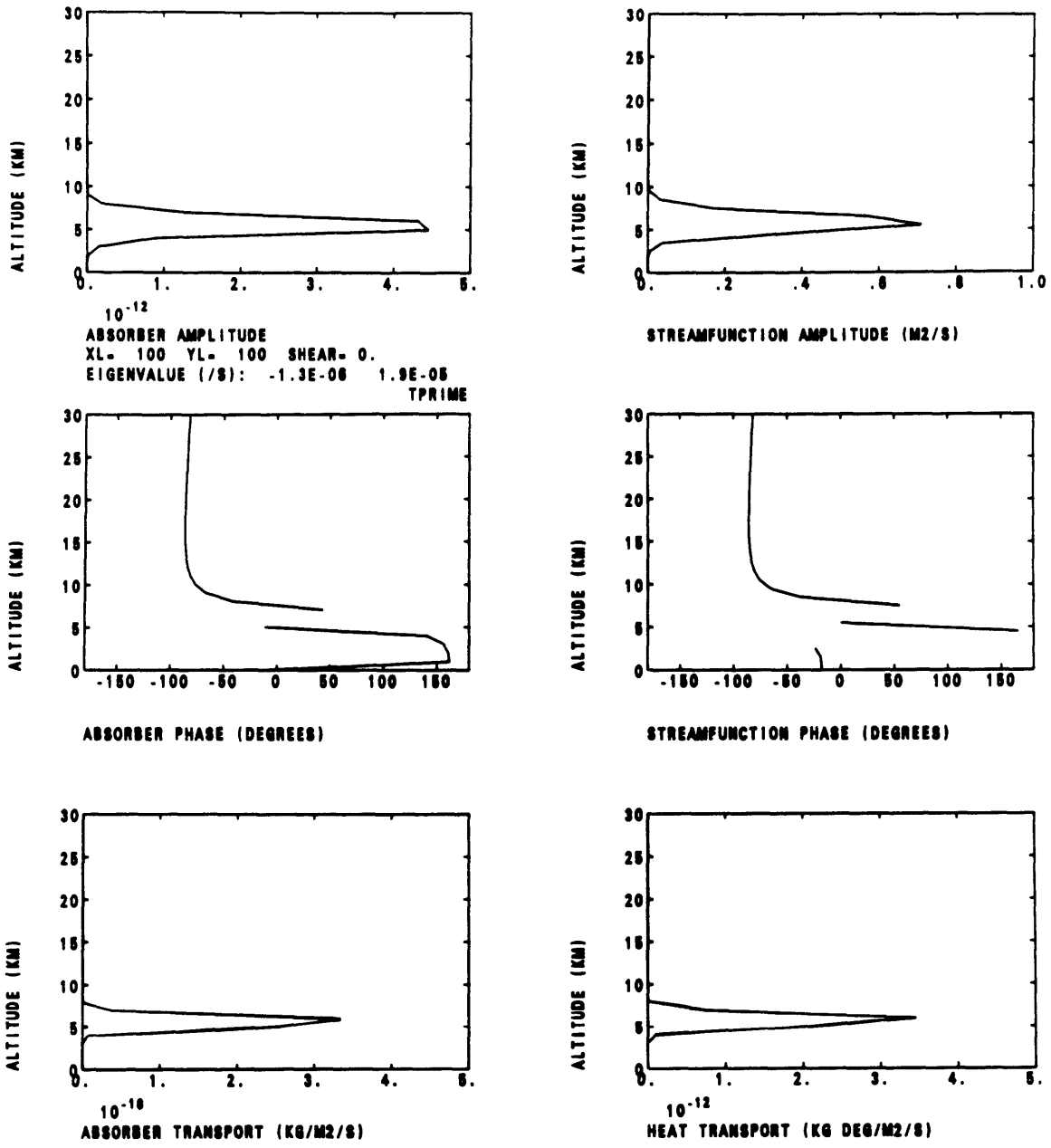

Figure 6.10. Vertical structure of the second most rapidly amplifying eigenmode for zonal and meridional wavelengths of 100 km and the exponential absorber distribution used in Figure 6.8. Perturbations in transmissivity are accounted for. Otherwise, as in Figure 6.3.

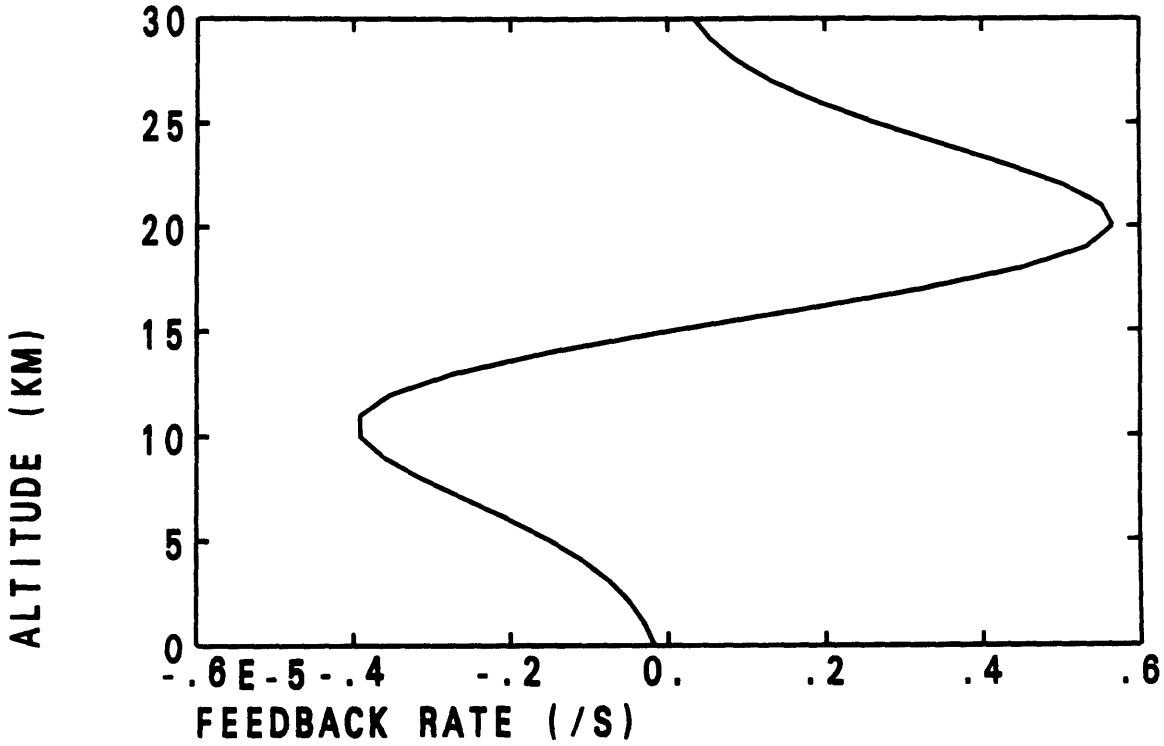

Figure 6.11. Radiative-dynamical feedback rate α_0 as a function of altitude for a Gaussian absorber distribution with a maximum mixing ratio of 10^{-7} at 15 km and a standard deviation of 5 km. Otherwise as in Figure 6.6.

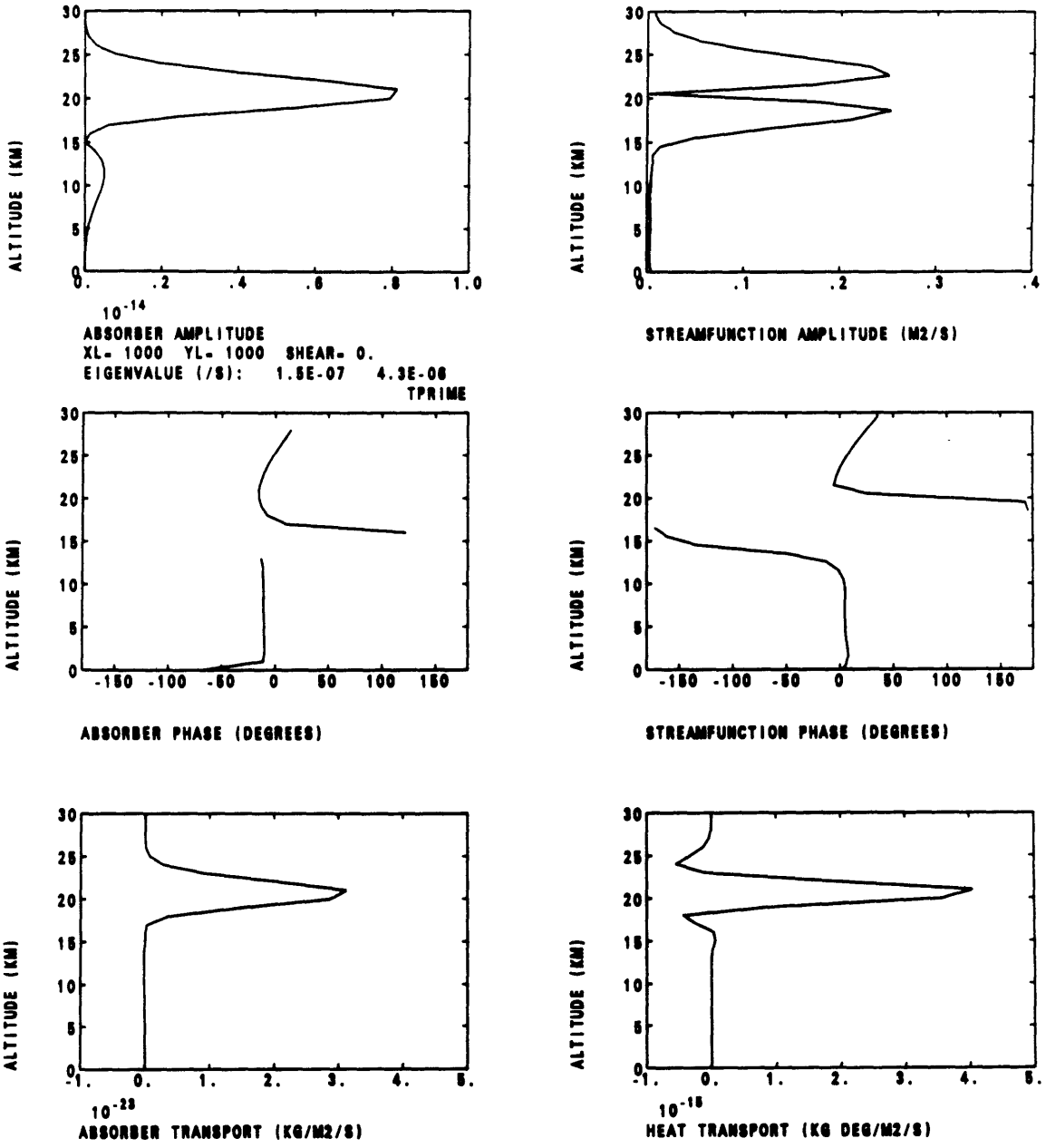

Figure 6.12. Vertical structure of the most rapidly amplifying eigenmode for zonal and meridional wavelengths of 1000 km and the Gaussian absorber distribution used in Figure 6.11. Perturbations in transmissivity are accounted for. Otherwise, as in Figure 6.3.

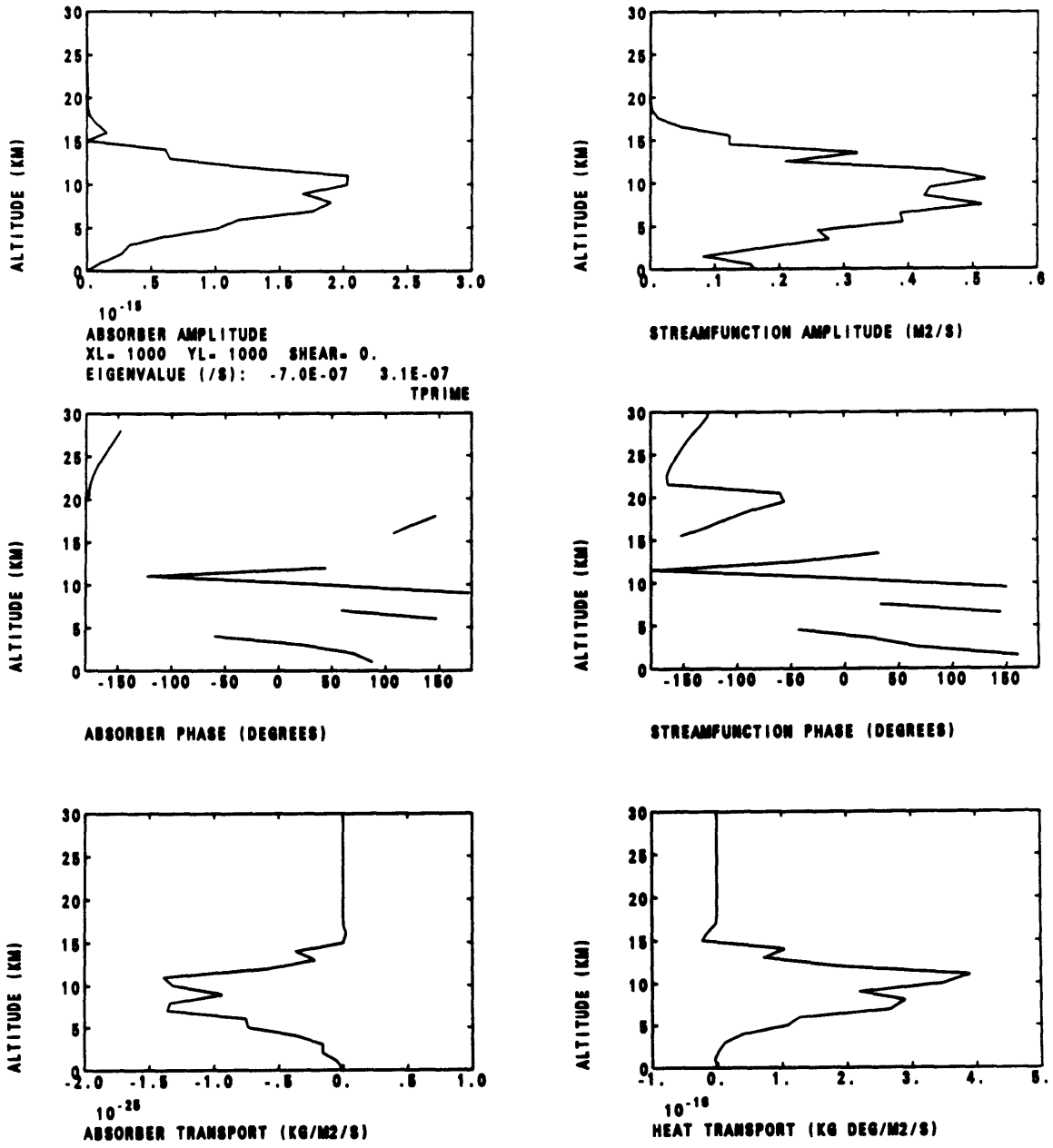

Figure 6.13. Vertical structure of the 15th most rapidly amplifying eigenmode for zonal and meridional wavelengths of 1000 km and the Gaussian absorber distribution used in Figure 6.11. Perturbations in transmissivity are accounted for. Otherwise, as in Figure 6.3.

7. Effect of Vertical Shear

One of the assumptions made in the basic analysis of Chapter 3 is that variations in the basic state zonal flow can be neglected. This simplified the analysis considerably. In fact, such an assumption is a poor approximation unless the radiative-dynamical feedback is strong and vertical shear is weak. In this chapter we shall consider the effects of relaxing that constraint, first in the case of weak shear, and then for strong shear. For weak shear we expect to find a reduction in the growth rate due to a disruption of the vertical structure of unstable modes. For sufficiently strong shear baroclinic instability plays a role. In fact, we shall find that while for sufficiently strong vertical shear the growth rate is enhanced as the shear is increased, for weak shear the growth rate can either increase or decrease with increasing shear. The dependence of the growth rate on the shear is apparently quite complex. Moreover, the growth rate of unstable modes in the presence of both strong vertical shear and strong radiative-dynamical feedback can in some cases exceed that estimated in the absence of either shear or feedback.

Because vertical shear greatly complicates the analysis, we shall restrict the problem to the quasi-geostrophic case (inertia-gravity waves, which are filtered by the quasi-geostrophic approximation, have much larger phase speeds than any realistic zonal velocities, and hence are relatively unaffected by realistic values of the vertical shear). Then the linearized quasi-geostrophic potential vorticity equation

$$D\nabla^2\psi + \beta\psi_x + \frac{f_0^2}{\rho_0} D \frac{\partial}{\partial z}\left(\frac{\rho_0\psi_z}{N^2}\right) - \psi_z \frac{f_0^2}{\rho_0}\frac{\partial}{\partial z}\left(\frac{\rho_0\overline{u}_z}{N^2}\right) = \frac{f_0}{\rho_0}\frac{\partial}{\partial z}\left(\frac{RQ}{c_p N^2 H}\right) \tag{7.1}$$

can be combined with the absorber balance and the relation between the heating and the absorber concentration, to yield the following partial differential equation

for the streamfunction ψ,

$$(D-\alpha)^2\left(D\nabla^2\psi+\beta\psi_x\right)+(D-\alpha)\,D\frac{f_0^2}{\rho_0}\left[D\,\frac{\partial}{\partial z}\,\left(\frac{\rho_0\psi_z}{N^2}\right)-\psi_z\,\frac{\partial}{\partial z}\left(\frac{\rho_0\overline{u}_z}{N^2}\right)\right]$$
$$-\frac{f_0^2}{N^2}\,\alpha\overline{u}_z\left(D\psi_{xz}-\overline{u}_z\psi_{xz}\right)=0 \tag{7.2}$$

where $D=-i\sigma+\overline{u}(z)ik$. To make further progress with this difficult problem, Lindzen (1966c) resorted to the two-level model. We take the alternate approach of restricting the analysis to the case in which vertical shear is weak while feedback is strong; the effect of vertical shear is then considered as a perturbation to the solution in the absence of shear. For simplicity, we also assume as in the Eady (1949) problem of baroclinic instability that the atmosphere is finite with uniform density, and neglect the meridional gradient of the Coriolis parameter. Then (7.2) reduces to

$$\frac{f_0^2}{N^2}\left(D-\alpha\right)D^2\,\frac{\partial^2\psi}{\partial z^2}+\left(D-\alpha\right)^2D\nabla^2\psi-\frac{f_0^2}{N^2}\,\alpha\overline{u}_z\left(D\psi_{xz}-\overline{u}_z\psi_{xz}\right)=0 \tag{7.3}$$

with boundary conditions

$$D\psi_z=\overline{u}_z\psi_x \qquad z=0,H \tag{7.4}$$

at the surface and at the top, H. Expanding D and ψ in powers of the expansion parameter

$$\epsilon\equiv\frac{\overline{u}_zk}{\alpha m} \tag{7.5}$$

(7.3) and (7.4) become, to zeroeth order,

$$\frac{f_0^2}{N^2}\left(D_0-\alpha\right)\;D_0^2\,\frac{\partial^2\psi_0}{\partial z^2}+\left(D_0-\alpha\right)^2D_0\nabla^2\psi_0=0 \tag{7.6}$$

and

$$D_0\frac{\partial\psi_0}{\partial z}=0 \qquad z=0,H \quad . \tag{7.7}$$

Assuming normal modes in x, y, z and t, the streamfunction satisfying the boundary conditions is

$$\psi_0 = a_0 \cos mz \tag{7.8}$$

where the vertical wavenumber m is constrained by the boundary conditions, $m = n\pi/H$, $n = 1, 2 \ldots$.

The solution $D_0 = \alpha$ is a spurious solution, while $D_0 = 0$ represents the Rossby mode on an f-plane. The solution

$$D_0 = \alpha \frac{k_2^2}{k_3^2} \tag{7.9}$$

is the familiar advective mode, which is unstable for positive α. This is the solution about which we shall expand for weak vertical shear.

The first order expansions of (7.3) and (7.4) are

$$\begin{aligned} \frac{f_0^2}{N^2}(D_0 - \alpha)\, D_0^2\, \frac{\partial^2 \psi_1}{\partial z^2} + (D_0 - \alpha)^2\, D_0 \nabla^2 \psi_1 \\ = -\alpha D_0 D_1 \frac{f_0 m^2}{N^2}\, \psi_0 - \frac{i f_0^2}{N^2}\, m^2 \alpha^2 D_0 a_0 \sin mz \end{aligned} \tag{7.10}$$

and

$$D_0 \frac{\partial \psi_1}{\partial z} + D_1 \frac{\partial \psi_0}{\partial z} = i\alpha m\, \psi_0 \qquad z = 0, H \quad . \tag{7.11}$$

Because the right-hand side of (7.10) is independent of ψ_1, (7.10) can be regarded as an inhomogeneous equation for ψ_1. D_1 is evaluated through the application of the boundary conditions. The general solution of (7.10) can be written

$$\psi_1 = a_1 \cos mz + b_1 \sin mz + \psi_p \tag{7.12}$$

where a_1 and b_1 are arbitrary constants determined by the boundary conditions, and ψ_p is the particular solution of (7.10). Note that although there only two boundary conditions, and hence two constraints to the first-order problem, there are three unknowns, namely a_1, b_1 and the complex frequency σ_1. However, the

coefficient a_1 can be arbitrarily set equal to zero with no loss of generality, because cos mz is proportional to ψ_0. The boundary conditions can then be used to determine b_1 and the complex frequency, once the particular solution is known.

Expressing $D_1 = -i\sigma_1 + \alpha\, imz$, the particular solution of (7.10) can be written

$$\psi_p = \frac{ia_0\alpha}{D_0\,(D_0-\alpha)}\left(\frac{\sigma_1 mz}{2}\,\sin\,mz - \frac{3\alpha}{8}\,\sin\,mz - \frac{\alpha m^2 z^2}{4}\sin\,mz + \frac{\alpha mz}{4}\cos\,mz\right)\,. \tag{7.13}$$

Application of the boundary condition at the surface determines b_1, namely

$$b_1 = \frac{ia_0\alpha}{D_0}\left[1 + \frac{\alpha}{8\,(D_0-\alpha)}\right] \tag{7.14}$$

which is proportional to the amplitude of the zeroeth order solution, as it should be. Application of the boundary condition at the top yields the first order perturbation to the complex frequency

$$\epsilon\sigma_1 = \frac{\overline{u}_z kH}{2} \quad . \tag{7.15}$$

Because σ_1 is pure real, the first-order effect of vertical shear is to alter the phase speed but not the growth rate.

For modifications to the growth rate, the second-order problem

$$\begin{aligned}
&\frac{f_0^2}{N^2}\,(D_0-\alpha)\;\; D_0^2\;\frac{\partial^2\psi_2}{\partial z^2} + (D_0-\alpha)^2\, D_0\nabla^2\psi_2 \\
&\quad = -\frac{f_0^2}{N^2}\,(3D_0-2\alpha)\;\; D_0 D_1\;\frac{\partial^2\psi_1}{\partial z^2} - (D_0-\alpha)\,(3D_0-\alpha)\;\; D_1\nabla^2\psi_1 \\
&\quad - \alpha D_0 D_2 \frac{f_0^2 m^2}{N^2}\;\psi_0 + D_1^2\left(k_2^2 - \frac{f_0^2 m^2}{N^2}\right)\alpha\psi_0 \\
&\quad + \frac{f_0^2}{N^2}\;\alpha^2 im\left(D_0\frac{\partial\psi_1}{\partial z} + D_1\frac{\partial\psi_0}{\partial z} - \alpha im\psi_0\right)
\end{aligned} \tag{7.16}$$

and

$$D_0\frac{\partial\psi_2}{\partial z} + D_1\frac{\partial\psi_1}{\partial z} + D_2\frac{\partial\psi_0}{\partial z} = i\alpha m\psi_1 \qquad z = 0, H \tag{7.17}$$

must be considered. Rather than solve the full eigenvalue problem, we instead invoke the solvability condition. Multiplying (7.16) by ψ_0, integrating over the

depth of the atmosphere, and applying the boundary conditions (7.17), we can solve for the second-order perturbation to the growth rate without explicitly solving for ψ_2. Although we shall not present the derivation (which is quite complicated), the solution for the perturbation to the growth rate can be written

$$\epsilon^2\sigma_2 = \frac{i\overline{u}_z^2 k^2 N^2}{16 D_0 f_0^2 m^2}\left[H^2\left(\frac{k_2^2}{4} - \frac{f_0^2 m^2}{N^2}\right) - \frac{37k_2^2}{m^2} + \frac{35f_0^2}{N^2} + \frac{24k_2^4}{m^2 k_3^2}\right] \quad . \tag{7.18}$$

Note that because the growth rate depends on the square of the vertical shear, the sensitivity to shear is the same for positive and negative shear. From numerical solutions we shall find that this holds for strong shear as well as weak shear. For deep waves (i.e., $m = \pi/H$), (7.18) reduces to

$$\epsilon^2\sigma_2 = \frac{iu_z^2 k^2 N^2 H^2}{16 D_0 f_0^2 \pi^2}\left[H^2 k_2^2\left(\frac{1}{4} - \frac{37}{\pi^2} + \frac{24k_2^2}{\pi^2 k_3^2}\right) + \frac{f_0^2}{N^2}\left(35 - \pi^2\right)\right] \quad . \tag{7.19}$$

For waves much shorter than the deformation radius, $k_2^2 \sim k_3^2$ and $Im(\sigma_2)$ is by (7.19) negative, so that the total growth rate $Im(\sigma_0 + \epsilon\sigma_1 + \epsilon^2\sigma_2)$ is less than $Im(\sigma_0)$, and weak vertical shear reduces the growth rate. For waves much longer than the deformation radius, $k_2^2 \ll k_3^2$ and $Im(\sigma_2)$ is positive, so that weak vertical shear enhances the growth rate. For horizontal wavelengths comparable to the deformation radius, $k_2^2 \sim \frac{1}{2}k_3^2$ and σ_2 is very nearly zero. Thus, weak vertical shear will reduce the growth rate if

$$k_2^2 > \frac{f_0^2\pi^2}{N^2H^2} = \frac{f_0^2 m^2}{N^2} \tag{7.20}$$

i.e., for waves shorter than the deformation radius, and enhance the growth rate for longer waves. For an atmospheric depth of 9 km, (7.20) predicts the transition to occur at a horizontal wavelength of about 2500 km. For waves shorter than this, vertical shear reduces the growth rate, while for longer waves shear increases the growth rate. However, for such long waves the variation of the Coriolis parameter with latitude cannot be neglected. Moreover, the assumption of a finite atmosphere with constant density is too restrictive to permit application to a realistic

atmosphere. To make further progress, we therefore turn to numerical solutions of the eigenvalue problem.

To extend the above analysis to stronger vertical shears, and to permit the use of a semi-infinite, quasi-Boussinesq atmosphere on a β-plane rather than a finite, Boussinesq atmosphere on an f-plane, we resort to numerical solutions of the eigenvalue problem. In Chapter 6 a one-dimensional numerical model of the quasi-geostrophic radiative-dynamical system is developed. Here we apply that model to the case in which vertical shear is present in the basic state zonal flow. For comparison with the above analysis, we shall first consider the case with uniform feedback for a Boussinesq atmosphere on an f-plane.

Table 7.1 lists the growth rate of the most rapidly amplifying mode determined numerically for various values of the vertical shear and the horizontal scale. The same assumptions adopted in the foregoing analysis, namely a finite atmosphere (9 km top) with constant density on an f-plane, have been employed in the numerical calculations. The basic state absorber distribution has been chosen such that the feedback rate is a constant 3.2×10^{-6} s^{-1}, with perturbations in the transmissivity neglected.

For sufficiently short perturbations, vertical shear has little effect on the instability. Baroclinic instability is not a factor for such waves and, because the growth rate in the absence of shear is insensitive to the vertical scale of short perturbations, shallow modes become increasingly more important as the shear is increased, but the largest growth rate changes little.

For synoptic-scale perturbations (wavelength 1000 km), the growth rate is evidently reduced by small amounts of shear. For stronger shear, the growth rate is enhanced by the shear as baroclinic instability becomes increasingly more important. For comparison, Table 7.2 lists the largest growth rate for the same cases as Table 7.1, but in the absence of any radiative-dynamical feedback. Consistent

with the Eady (1949) model of baroclinic instability, short waves are stable while long waves are unstable, with growth rates proportional to the vertical shear. For synoptic-scale waves, baroclinic effects enhance the radiative-dynamical instability even though such waves are neutral under adiabatic conditions (in the Eady model of baroclinic instability, the horizontal scale at which instability begins depends on the atmospheric depth; for a 9 km atmosphere, the transition occurs at about 3500 km). The amount of vertical shear required to enhance rather than suppress the instability depends on the strength of the radiative-dynamical feedback; for stronger feedback, stronger shear is required. Note that weak feedback can destabilize waves that under adiabatic conditions would be neutral. The growth rate of the synoptic-scale waves for strong shear is larger than that in the absence of either shear or radiative-dynamical feedback.

For planetary-scale perturbations (wavelength 10,000 km), the growth rate is enhanced by the vertical shear for all vertical shears. This is to be expected on the basis of (7.20). Indeed, (7.20) predicts the transition from suppression of the growth rate to enhancement at horizontal wavelength 2500 km (for a model with a top at 9 km), while numerical calculations indicate the transition occurs at about 2000 km. Because of this agreement, we can have some confidence in both the analysis and the numerical calculations.

The problem becomes more complicated when the Boussinesq approximation is relaxed, and variations in the Coriolis parameter and perturbations in the transmissivity are accounted for. Table 7.3 lists the growth rate of the most rapidly amplifying mode for various values of the vertical shear and horizontal wavelengths, and a basic-state absorber distribution such that the feedback rate is a uniform 2.3×10^{-6} s^{-1} in a 30 km atmosphere.

In the absence of vertical shear the maximum growth rates for each horizontal scale are similar to those of Table 7.1, except for the planetary scale waves, for

which the β term enhances the instability (recall that if the feedback rate is much less than the Rossby frequency the growth rate equals the feedback rate, whereas if the feedback rate dominates the Rossby frequency the growth rate is much less than the feedback rate for long shallow waves).

Consistent with the results on the f-plane, the growth rate of the short waves is insensitive to vertical shear. However, the vertical scale of the most rapidly growing mode is restricted under strong shear.

For synoptic-scale waves, we find again that weak shear reduces the growth rate, while strong shear enhances the growth rate. For comparison, Table 7.4 lists the growth rate of the most rapidly amplifying modes in the absence of radiative-dynamical feedback. There is a strong correspondence between those cases in which vertical shear enhances the growth rate of the radiative-dynamical interaction and those cases in which the shear exceeds the adiabatic threshold for instability. For strong shear the growth rate with feedback is stronger than either that without feedback or without shear, indicating that relatively weak feedback can enhance the growth rate of synoptic-scale baroclinic waves. In all cases the growth rate does not exceed the sum of the feedback rate and the adiabatic growth rate.

For planetary-scale waves we find that, contrary to the analysis on the f-plane, weak shear suppresses the radiative-dynamical instability. For sufficiently strong shear, the growth rate increases, but does not exceed that associated with adiabatic baroclinic instability.

In summary, vertical shear is found to have little effect on the growth of radiative-dynamical modes that are both neutral with respect to adiabatic baroclinic instability, and short enough so that the vertical scale can shift without reducing the growth rate. For waves that are baroclinically unstable in the absence of radiative-dynamical feedback, the feedback can, depending on the horizontal scale of the wave, either enhance or reduce the growth rate. In either case the growth

rate with both feedback and shear is less than the sum of the feedback rate and the adiabatic growth rate.

Table 7.1. Vertical shear with uniform feedback on an f-plane.

Growth rate (s^{-1}) of the most rapidly amplifying mode, based on numerical solutions of the eigenvalue problem for a Boussinesq atmosphere of depth 9 km on a midlatitude f-plane, with a uniform radiative-dynamical feedback rate of 3.2×10^{-6} s^{-1}. Perturbations in transmissivity are neglected.

Vertical shear ($m\ s^{-1}\ km^{-1}$)	Horizontal wavelength (km) 100	1000	10,000
0.0	3.266×10^{-6}	2.786×10^{-6}	1.864×10^{-7}
0.01	2.988×10^{-6}	2.777×10^{-6}	1.888×10^{-7}
0.1	2.751×10^{-6}	1.925×10^{-6}	3.037×10^{-7}
1.0	4.024×10^{-6}	1.963×10^{-6}	1.662×10^{-6}
10.0	4.430×10^{-6}	1.091×10^{-5}	1.519×10^{-5}

Table 7.2. Vertical shear without feedback on an f-plane.

As in Table 7.1, but without radiative-dynamical feedback. Equivalent to the Eady (1949) problem of baroclinic instability.

Vertical shear ($m\ s^{-1}\ km^{-1}$)	Horizontal wavelength (km) 100	1000	10,000
0.0	0.0	0.0	0.0
0.01	0.0	0.0	1.503×10^{-8}
0.1	0.0	0.0	1.503×10^{-7}
1.0	0.0	0.0	1.503×10^{-6}
10.0	0.0	0.0	1.503×10^{-5}

Table 7.3. Vertical shear with uniform feedback on a β-plane.

Growth rate (s^{-1}) of the most rapidly amplifying mode, based on numerical solutions of the eigenvalue problem for a quasi-Boussinesq atmosphere of depth 30 km (1 km resolution) on a midlatitude β-plane, with a uniform radiative-dynamical feedback rate of 2.3×10^{-6} s^{-1}. Perturbations in transmissivity are accounted for.

Vertical shear	Horizontal wavelength (km)		
(m s^{-1} km^{-1})	100	1000	10,000
0.0	2.299×10^{-6}	2.042×10^{-6}	1.307×10^{-6}
0.01	2.263×10^{-6}	2.024×10^{-6}	1.283×10^{-6}
0.1	2.338×10^{-6}	1.199×10^{-6}	1.325×10^{-6}
1.0	2.381×10^{-6}	2.945×10^{-6}	5.925×10^{-7}
10.0	2.382×10^{-6}	9.924×10^{-6}	2.303×10^{-5}

Table 7.4. Vertical shear without feedback on a β-plane.

As in Table 7.3, but without radiative-dynamical feedback. Equivalent to the Charney (1947) problem of baroclinic instability.

Vertical shear	Horizontal wavelength (km)		
(m s^{-1} km^{-1})	100	1000	10,000
0.0	0.0	0.0	0.0
0.01	0.0	0.0	0.0
0.1	0.0	0.0	0.0
1.0	0.0	8.387×10^{-7}	6.453×10^{-7}
10.0	0.0	5.750×10^{-6}	2.311×10^{-5}

8. Effect of Scattering

Although absorbers of solar radiation such as ozone and water vapor do not scatter significant amounts of sunlight, aerosols such as those associated with Martian dust storms, volcanic eruptions, and the proposed "nuclear winter" phenomenon typically scatter at least as much sunlight as they absorb (Pollack et al., 1976, Pollack et al., 1979; NRC, 1985). Thus, for applications to aerosols, the effects of scattering on the radiative-dynamical interaction should be considered. Here we do so by generalizing the numerical model of the linear instability problem introduced in Chapter 6. We shall find that scattering can either increase or decrease the radiative-dynamical instability, depending on whether the aerosols scatter sunlight primarily to other particles or to space.

Within the context of a discrete linear model, the perturbation radiative heating can be more generally related to perturbations in absorber concentration according to the Jacobian,

$$\mathbf{Q}' \equiv \mathbf{Q} - \overline{\mathbf{Q}} = \mathbf{J}\mathbf{q}' \tag{8.1}$$

where the vector $\mathbf{Q}$ represents the radiative heating in a set of discrete model layers, the vector $\mathbf{q}$ denotes the absorber mixing ratio at an equal number of discrete levels, and

$$J_{ij} = \frac{\partial Q_i}{\partial q_j}(\mathbf{q} = \overline{\mathbf{q}}) \tag{8.2}$$

is the Jacobian of the heating rate with respect to the absorber distribution. In the absence of scattering, the Jacobian can be defined analytically; the Jacobian is a diagonal matrix if perturbations in the transmissivity are neglected. For the more general case with scattering it is not possible to determine the Jacobian analytically; we therefore resort to numerical means. In particular, we first determine the solar heating rate for the basic state, using an appropriate solar radiation model [here we shall use Wiscombe's (1977) delta-Eddington model, which is accurate even for

scattering that is highly anisotropic]. The Jacobian is then evaluated by separately adding a small amount of absorber in each model layer, calculating the heating in all layers, and subtracting the basic-state heating.

Table 8.1 lists the growth rate of the most rapidly amplifying mode determined in the above manner for several different single-scattering albedos (the ratio of the scattering coefficient to the extinction coefficient) and solar zenith angles. The exponential distribution has been assumed for the absorber mixing ratio, with a surface mixing ratio of 10^{-6} and a scale height of 10 km. The same specific absorption coefficient (1000 m^2 kg^{-1}) has been used in each case, with only the specific scattering coefficient and solar zenith angle altered. Scattering is assumed to be isotropic, and the surface is perfectly absorbing. The zonal and meridional wavelengths have been assumed to be 1000 km.

When the sun is directly overhead ($\mu = 1$), an increase in scattering increases the maximum growth rate. This occurs because the scattering increases the path length, and hence the number of aerosols a photon will encounter. Absorption therefore increases, and the radiative-dynamical feedback is enhanced.

For a 60° solar zenith angle, scattering does not significantly increase the path length. In this case another factor becomes important, namely the effective reduction in the solar constant due to the scattering of energy to space. Absorption is reduced by scattering, and the maximum growth rate decreases with increasing scattering.

Thus, two processes associated with scattering, namely increased path length due to multiple reflections, and reduced insolation due to scattering to space, compete to alter the radiative-dynamical interaction. Which process dominates depends upon the solar zenith angle and the aerosol scattering angle (which in two-stream models is expressed in terms of an asymmetry factor). When the single

scattering albedo of an aerosol is 0.98 (which is appropriate for dust), scattering can either enhance or reduce the growth rate by some 30%.

The calculations of Table 8.1 assume scattering is isotropic. In fact, scattering of sunlight by aerosols is primarily in the forward direction. An asymmetry factor of at least 0.5 is more appropriate for most aerosols. Table 8.2 lists the maximum growth rates for the same cases as in Table 8.1, except with an asymmetry factor of 0.5. In the absence of scattering, the growth rates are independent of the asymmetry factor. When scattering becomes predominant, we find that the growth rates are larger with forward scattering than with isotropic scattering. This reflects the smaller fraction of sunlight that is reflected to space with forward scattering than with isotropic scattering. Thus, with forward scattering the growth rate is increased by scattering for a wider range in solar zenith angles than for isotropic scattering.

The same technique used to treat the effects of scattering can also be applied to infrared radiative processes. The perturbation longwave heating is determined from the difference between numerical solutions of infrared heating for basic state and perturbation temperature and absorber profiles. Unfortunately, we have found that because of the presence of undamped computational modes associated with the vertical interpolation of temperature, the growth rate of the most rapidly amplifying solution changes little when the effect of infrared heating associated with either temperature perturbation or absorber perturbations is accounted for. Thus, we have been unable to realistically determine the effects of longwave radiative processes on the radiative-dynamical instability.

Table 8.1. Isotropic scattering.

Growth rate (s^{-1}) of the most rapidly amplifying mode, based on numerical solutions of the eigenvalue problem for a mid-latitude β-plane. The basic state absorber mixing ratio decays exponentially with scale height 10 km from a surface mixing ratio of 10^{-6}. The absorption coefficient is 1000 m^2 kg^{-1}. Scattering is isotropic, with no reflection from the surface. The zonal and meridional wavelengths are both 1000 km.

Single-scattering albedo	$\mu = 1$	$\mu = 0.5$
0.0	6.35×10^{-6}	4.67×10^{-6}
0.5	7.20×10^{-6}	4.64×10^{-6}
0.98	8.30×10^{-6}	3.32×10^{-6}

Table 8.2. Forward scattering.

As in Table 8.1, but with an asymmetry factor for scattering equal to 0.5.

Single-scattering albedo	$\mu = 1$	$\mu = 0.5$
0.0	6.35×10^{-6}	4.67×10^{-6}
0.5	7.10×10^{-6}	4.63×10^{-6}
0.98	9.13×10^{-6}	3.63×10^{-6}

9. Application to Smoke Lofting

Simulations of the so-called "nuclear winter" by GCMs have indicated substantial lofting of smoke caused by the absorption of sunlight and consequent warming. This result is consistent with the upward absorber transport by the advective mode of instability in the present theory of radiative-dynamical instability. There are however, several reasons to believe that the lofting mechanism simulated in the GCM experiments may not be the same as the theoretical advective mode.

First, the vertical gradient of smoke mixing ratio in the simulations is large only for a very limited range in altitude, so that the range of strong radiative-dynamical feedback is quite narrow. The most unstable modes would therefore, according to the theory, also be quite shallow. Also according to the theory, the growth rate is largest for waves for which the three-dimensional and two-dimensional wavenumbers squared are similar, i.e., for waves that are short and deep. Because waves must be shallow to experience maximum feedback, they must also be extremely short to amplify rapidly. It is therefore unlikely that the GCM simulations, with horizontal grid sizes of typically 500–1000 km, are resolving much of the lofting predicted by theory.

Because the GCM simulations do in fact exhibit substantial lofting, the natural question to ask is, by what mechanism? Why does the theory of radiative-dynamical instability fail to predict rapid lofting on the large scales evident in the GCM simulations? Although the theory in its present form has several shortcomings, the outstanding deficiency is its reliance on the assumption of a horizontally uniform basic state. In all GCM simulations of "nuclear winter," the initial smoke distribution is confined to one or several continental-scale regions. The heating gradients that develop from such inhomogeneous conditions produce pressure gradients that drive convergence beneath the smoke plume and lofting of the smoke to higher altitudes. Thus, the lofting occurs primarily as a result of the initial horizontal gradients in the smoke distribution (variations in the solar zenith angle

higher altitudes. Thus, the lofting occurs primarily as a result of the initial horizontal gradients in the smoke distribution (variations in the solar zenith angle also contribute to the differential heating). The lofting is not an unstable normal mode of the radiative-dynamical system because advection of the smoke is not necessary for the vertical motion to occur. Thus, even if the theory of radiative-dynamical instability were generalized to treat horizontal inhomogeneities in the initial smoke distribution, it would still fail to predict the smoke lofting mechanism exhibited in the GCM simulations because such lofting is not a modal instability (i.e., growth is not exponential). In this sense the GCM-simulated nonmodal smoke lofting resembles the nonmodal form of baroclinic instability discussed by Farrell (1984).

The remaining question is whether, if the horizontal resolution of a numerical model was fine enough, the small-scale modal form of smoke lofting predicted by the present theory would be evident in simulations initialized with smoke patches. If the initial smoke distribution fills the horizontal domain, then nonmodal lofting would not occur and smoke lofting would be dominated by short horizontal scales as predicted by theory (if the variation of the solar zenith angle is accounted for, nonmodal lofting would occur on planetary scales even for a uniform smoke distribution; we shall neglect this effect as it can be approximated by a planetary-scale smoke patch with a uniform solar zenith angle). If the initial smoke patches are the same size as the dominant unstable modes predicted by theory, then the modal lofting would coincide with the nonmodal lofting; it would be difficult to distinguish the two lofting mechanisms in this case. If the initial smoke patches covered a fraction of the domain but were much larger in horizontal scale than those that amplify as unstable modes, then nonmodal lofting would dominate early in the simulation, but at later times the exponentially growing modes would amplify sufficiently to be observable in the simulations. Thus, it seems that for smoke

patches that are sufficiently small, the modal lofting would probably be indistinguishable from the nonmodal lofting, while for larger smoke patches the small-scale modal lofting would, in the absence of nonlinear effects, eventually dominate the large-scale nonmodal lofting.

It is not obvious for which smoke patch sizes the small-scale lofting predicted by the present theory would be distinguishable from that associated with the lofting of the smoke patches themselves. Moreover, other instabilities (i.e., convective, inertial, or inertio-convective) could be induced as a result of the nonmodal response to the smoke. In order to address this question, numerical simulations of smoke lofting are necessary, using a model with a horizontal grid size sufficiently small to resolve the unstable modes predicted by theory. By varying the horizontal scale of the smoke patch, the patch size separating the modal and nonmodal forms of lofting can be determined.

To properly address these issues a three-dimensional numerical model on a β-plane or preferably on a sphere should be used. But the cost of such a model with fine horizontal resolution would greatly limit the number of experiments that could be performed. However, if one is not concerned with the effect of the differential rate of horizontal advection by vertical shear, and if one considers only horizontal scales which are short enough that the radiative-dynamical feedback rate is much larger than the Rossby wave frequency, then a two-dimensional model should be capable of addressing the issue of the competition between modal and nonmodal lofting, at a small fraction of the cost. Thus, although we recognize that a three-dimensional global model may ultimately be required, we choose to first treat the problem with a two-dimensional slab-symmetric primitive equation model on an f-plane.

For simplicity we shall use a dry model, i.e., a model in which clouds are neglected and water vapor is not a prognostic variable. To treat the stabilizing effects

of water vapor on the lapse rate we shall convectively adjust the lapse rate to that of a moist adiabat if the lapse rate exceeds that of a moist adiabat. Moreover, to treat the additional stabilizing effects of other processes such as baroclinic instability, we also adjust the lapse rate such that the potential temperature always increases with altitude at a rate exceeding 3 K km^{-1}. (This adjustment was implemented mainly to produce a realistic initial state; for the absorber injections considered here the radiative-dynamical feedback is largest in the stratosphere, so that the adjustment does not directly affect the development of the instability). For the radiative effects of water vapor in the atmosphere we assume a constant absolute humidity as a function of height only, using the AFGL midlatitude summer profile. Longwave radiative cooling is treated using the Harshvardhan et al. (1987) broad-band parameterization. Solar heating is simulated with the Wiscombe (1977) delta-Eddington model used in Chapter 8, with a uniform solar zenith angle. Radiative constituents are water vapor, carbon dioxide, ozone and (optionally) smoke for the longwave, and ozone and smoke for the short wave. The surface temperature is prescribed as for an ocean-covered planet, with simple drag laws for the exchange of heat and momentum at the surface. Sub-grid scale horizontal mixing is represented by a Smagorinsky (1963) type parameterization. Details of the numerical model are given in Appendix C.

This simple treatment neglects many aspects of the "nuclear winter" hypothesis. It is not, however, our intention to try to simulate all aspects of the proposed phenomenon. Rather, we are primarily concerned with the possibility that the GCM simulations have not properly resolved the smoke lofting and, implicit in the vertical distributions of the initial smoke concentration, may have neglected substantial smoke lofting that might occur on meso-scales during the first days before the smoke spreads to the scales resolved by the GCMs. Although such

model features as a spatially varying solar zenith angle and treatments of precipitation scavenging and horizontal spreading associated with vertical shear are undoubtedly important in determining the climatic consequences of a nuclear war, they are not necessary to address, in an approximate manner, the specific issue of lofting on small scales. If it is found that the GCM simulations have in fact underestimated smoke lofting, or used inappropriate initial smoke distributions, then further investigation using sophisticated three-dimensional models with relatively fine horizontal resolution is warranted.

The initial conditions for all experiments consist of the appropriate smoke injection plus the radiative-convective equilibrium solution for a uniform distribution of surface temperature. The initial state is therefore at rest, with the vertical distribution of potential temperature illustrated in Figure 9.1. In all experiments the atmosphere is represented by an infinite slab with a total of 30 levels spaced equally in height between the surface and 30 km. To evaluate the effect of varying the horizontal resolution and the smoke patch size, the horizontal domain and the horizontal grid spacing are altered for some experiments.

To simplify comparisons, the same vertical distribution of smoke is chosen for all experiments. This consists of a Gaussian distribution with altitude. The maximum smoke mixing ratio is 10^{-6} at 10 km. The standard deviation is 5 km. The vertically integrated absorber concentration for such a distribution is comparable to concentrations typically employed as initial conditions for global simulations of "nuclear winter" (Covey et al., 1984). The height dependence is similar to that of typical smoke mixing ratio profiles calculated in simulations of the smoke plume that might develop over burning cities (Penner et al., 1986). The resulting distribution of the radiative-dynamical feedback rate is shown in Figure 9.2. To crudely account for the diurnal cycle the solar zenith angle is 60°, which represents the appropriate average for the illuminated half of the globe, while

the solar constant has been reduced by a factor of two, to 680 Wm^{-2}. This same treatment is employed in the numerical simulations. The usual value for the specific absorption, 10^3 m^2 kg^{-1}, is used; although the specific absorption of soot can be as large as ten times this value, it is the product of the absorption coefficient and the smoke mixing ratio that matters, so that the same feedback distribution results for a larger absorption coefficient and a smaller smoke concentration. The Brünt-Vaisala frequency is chosen to be 1.6 x 10^{-2} s^{-1}, which is larger than the value used previously, but is more appropriate for the stratosphere where, according to Figure 9.2, the feedback rate is largest. The maximum feedback rate is nearly 8 x 10^{-6} s^{-1} at about 17 km. Below 10 km the feedback rate is of course negative, but is quite weak due to low transmission of sunlight through the smoke patch.

The first issue which must be addressed is the manifestation of the instability in optimal conditions, i.e., those for which the radiative-dynamical instability is resolved, but nonmodal lofting is prohibited. Figure 9.3 shows the absorber mixing ratio after 20 days of integration following initialization with a uniform horizontal distribution of absorber mixing ratio. The horizontal domain is 1000 km, with a 10 km resolution. Deep rising plumes of high absorber concentration are evident on horizontal scales that are quite short, typically 100 km, but are nonetheless well resolved by the model.

To compare with the theory of radiative-dynamical instability, Figures 9.4 and 9.5 show vertical profiles of absorber transport from the above simulation at 20 days and from the most rapidly amplifying eigenmode calculated for a 100 km horizontal wavelength and the feedback distribution illustrated in Figure 9.2. The theory evidently predicts the altitude of maximum upward absorber transport fairly accurately, but the simulated absorber transport is much broader, with respect to altitude, than the first eigenmode; additional eigenmodes probably also contribute

to the upward absorber transport. Consistent with the analysis of Chapter 6, absorber transport is downward in the simulation below 10 km, the level of maximum absorber mixing ratio; while such transport might be interpreted as being due to unstable propagating modes (in this case inertia-gravity waves), it is more likely that the downward transport is due to numerical diffusion associated with noise on the shortest scales resolved by the model.

We shall now consider smoke patches that are substantially smaller than the model domain. Such a treatment is appropriate even for smoke distributions that are globally uniform because insolation varies on the planetary scale. As discussed above, lofting due to the radiative-dynamical instability can be distinguished from nonmodal lofting only if the smoke patch size is much larger than the horizontal scales expected to be important for the radiative-dynamical instability. Because the plume scales evident in Figure 9.3 are much shorter than the model domain, it may be possible to isolate the two modes of lofting within a 1000 km model domain. Figure 9.6 shows the absorber mixing ratio 10 days following a Gaussian injection with a standard deviation of 300 km, shorter than the model domain, but longer than the horizontal scales expected for radiative-dynamical instability. Rapid nonmodal lofting is evident, such that after 10 days significant absorber mass has reached the 30 km model top, and the experiment must be terminated. No evidence exists of absorber transport on scales other than that of the absorber injection. Although the radiative-dynamical instability might conceivably emerge upon further integration with a larger model domain, other processes are likely to interfere with the interpretation of the simulation results. In particular, Figure 9.7 shows the Ertel potential vorticity (the product of the absolute vorticity with the vertical gradient of potential temperature) 10 days following the absorber injection. A region of negative potential vorticity has developed in the vicinity of a jet formed by the circulation. Slantwise convection (Emanuel, 1983) is likely to arise

in this region. The narrow scale of such circulations could easily be confused with that associated with radiative-dynamical instability. It is therefore unlikely that radiative-dynamical instability can be identified for absorber injections as narrow as 300 km.

For broader absorber injections the likelihood of isolating the radiative-dynamical instability increases. Figure 9.8 shows the absorber mixing ratio 30 days after a Gaussian injection with a 3000 km standard deviation. The model domain has been extended to 10,000 km, while the grid spacing has been increased to 33 km. In this case nonmodal lofting is greatly reduced due to the broad absorber injection. Modal lofting associated with radiative-dynamical instability is clearly evident, with mesoscale perturbations in absorber concentration protruding upward from the top of the absorber patch. Although the potential vorticity at 30 days is reduced nearly to zero in pockets within the vicinity of the mesoscale circulations, the circulations develop before the low potential vorticity arises, so that the low potential vorticity is more likely a result than a cause of the mesoscale circulations.

The horizontal scale of the mesoscale circulations, about 500 km, is somewhat shorter than the deformation radius but certainly not as short as might be expected on the basis of the modal theory. The shorter scales have been damped by horizontal mixing parameterized in the model to prevent the accumulation of energy on the shortest resolved scales. Without such mixing inertial instabilities develop before the circulations are strong enough to transport a significant amount of absorber upward.

To compare the modal versus nonmodal lofting, Figure 9.9 shows vertical profiles of the absorber transport at days 10 and 30 following the injection. At day 10 the mesoscale circulations have not yet developed, so that the absorber transport is principally of the nonmodal type. Note the strong correspondence between the vertical profile of the absorber transport at day 10 and the vertical distribution of

the absorber. This is due to the deep vertical scale of the nonmodal circulation, which arises as a result of convective mixing of the radiative heating throughout the troposphere. The fact that the transport is greatest near the altitude of maximum absorber mixing ratio, where the radiative-dynamical feedback rate is zero, is unmistakable evidence that the transport at day 10 is not associated with the modal instability. By day 30 the absorber transport in the troposphere has decreased somewhat, probably due in part to spurious numerical diffusion of absorber mass below the level of maximum absorber mixing ratio. Absorber transport at higher altitudes has increased substantially. Because the absorber distribution has actually shifted very little in 30 days, it is unlikely that this increase in absorber transport is due to nonmodal lofting. Rather, we can ascribe the increase in transport to the modal form associated with radiative-dynamical instability. It is evidently comparable to the nonmodal transport which dominates early in the simulation.

The final question is the effect of model resolution on the absorber transport. If the transport is dominated by the modal type, which is most rapid on mesoscales, then we expect the total transport to be reduced in a model with much coarser horizontal resolution. Figure 9.10 shows vertical profiles of the absorber transport 30 days following the same absorber injection (the 3000 km Gaussian distribution) and model domain (10,000 km) but for two different horizontal resolutions, namely 33 km and 330 km. The absorber transport 30 days post injection is, as expected, significantly greater for the high resolution experiment, with a factor of two difference in the maximum transport rate (nonmodal transport limits the effect of model resolution on total transport). It should be noted, however, that this result is dependent upon the treatment of horizontal mixing. In these experiments the horizontal mixing length for the coarse resolution model is, following Smagorinsky (1963), 10 times as large as that for the fine resolution model. If, instead, the

same mixing length used for the fine resolution model (10 km) is also used for the coarse model, the absorber transport for the two experiments is quite comparable. This occurs because the strong mixing of the shortest scales in the fine resolution model damps all scales shorter than 500 km (see Figure 9.8), so that the vertical transport is accomplished by the same scales in each experiment. Because such scales are not as small as those expected to dominate in the radiative-dynamical instability, we would expect the absorber transport associated with the instability to be greater yet in a model with sufficiently fine resolution that the mesoscales need not be subjected to mixing. Such a model is, however, impractical for such a large domain even for two-dimensional flow.

To understand the parametric dependence of these results, let us compare the nonmodal vertical velocity with the modal vertical velocity. Neglecting the β term, the Rossby wave equation (3.9) for perturbations of the form (3.14) reduces to

$$w = \frac{k_2^2}{k_3^2} \frac{RQ}{c_p \rho_0 N^2 H}. \tag{9.1}$$

Here k_2^2 and k_3^2 are the squared wavenumbers consistent with the spatial scales of the heating. Note that vertical motion for a given heating rate is greatest for heating with horizontal scales much less than the internal deformation radius, with the adiabatic cooling of ascent exactly balancing the diabatic heating. For larger horizontal scales some of the diabatic heating is used to change the temperature distribution, so that vertical motions are less vigorous. We shall now apply (9.1) to both the modal and nonmodal circulations.

For the nonmodal circulation, $Q = S_0 a \rho_0 q T$ and (9.1) becomes

$$w = \frac{k_2^2}{k_3^2} \frac{RS_0 aqT}{c_p N^2 H} \tag{9.2}$$

Here the squared wavenumbers k_2^2 and k_3^2 and the absorber mixing ratio q and transmissivity T are taken to be consistent with the spatial scales and density of the absorber patch.

For modal circulations we assume that an initial mesoscale perturbation absorber mixing ratio $q'(0)$ almost immediately produces a perturbation vertical velocity which amplifies exponentially with time,

$$w'(t) = \frac{RS_0 a\overline{T}q'(0)}{c_p N^2 H}\ e^{\sigma_i t} \tag{9.3}$$

Here $q'(0)$ can be taken as the projection of the initial smoke patch onto horizontal modes much smaller than the internal deformation radius (i.e., $k_2^2 \sim k_3^2$).

Comparing (9.2) and (9.3), we find that the ratio

$$\frac{w'}{w} = \frac{k_3^2}{k_2^2}\frac{q'(0)}{q}e^{\sigma_i t} \tag{9.4}$$

is initially small provided the horizontal scale of the absorber patch is comparable to or smaller than the internal deformation radius (i.e., $k_2^2 \sim k_3^2$) and provided the initial mesoscale absorber perturbation is much smaller than the absorber mixing ratio at the level of maximum heating. Under such conditions the modal circulation will not be evident until the instability has amplified sufficiently. Even then it will be difficult to identify modal circulations unless their horizonal scales are much shorter than that of the absorber patch. However, for absorber patches much broader than the internal deformation radius ($k_2^2 \ll k_3^2$) the modal circulation, though perhaps initially weaker than the nonmodal flow, will rather quickly overcome the relatively weak nonmodal circulation. At this point the linearization probably breaks down, and the amplification no longer continues exponentially.

To summarize, we have been able to distinguish between modal and nonmodal forms of smoke lofting when the smoke patch scale is much larger than the mesoscales expected to dominate modal lofting. In this case the nonmodal lofting dominates initially, but modal lofting eventually exceeds the nonmodal lofting. If the smoke patch size is comparable to the mesoscale then it is unlikely that the modal and nonmodal forms of lofting can be distinguished.

The fact that we have only been able to identify the modal form of lofting in simulations in which absorber transport is actually quite slow does not necessarily imply that the radiative-dynamical instability is of minor importance. We have assumed quiescent initial conditions in all of our simulations, whereas in reality ambient perturbations associated with orographic and convective forcing would accelerate the emergence of the mesoscale radiative-dynamical instability. The growth rates predicted by the theory are quite rapid for the absorber profile chosen in the above experiments (the e-folding time for the mode illustrated in Figure 9.5 is about 2 days), so that the delay in the emergence of the modal lofting is mainly due to the weakness of mesoscale absorber perturbations in the initial conditions (small perturbations associated with the projection of the mesoscale modes onto the initial absorber distribution are probably what eventually emerge as the modal instability). If we had chosen to initialize the experiments with arbitrary mesoscale perturbations of absorber and vertical velocity the radiative-dynamical instability might have become evident more rapidly, but the results would have been dependent on the magnitude of the initial perturbations. We have chosen the more conservative quiescent initial state to avoid such ambiguities.

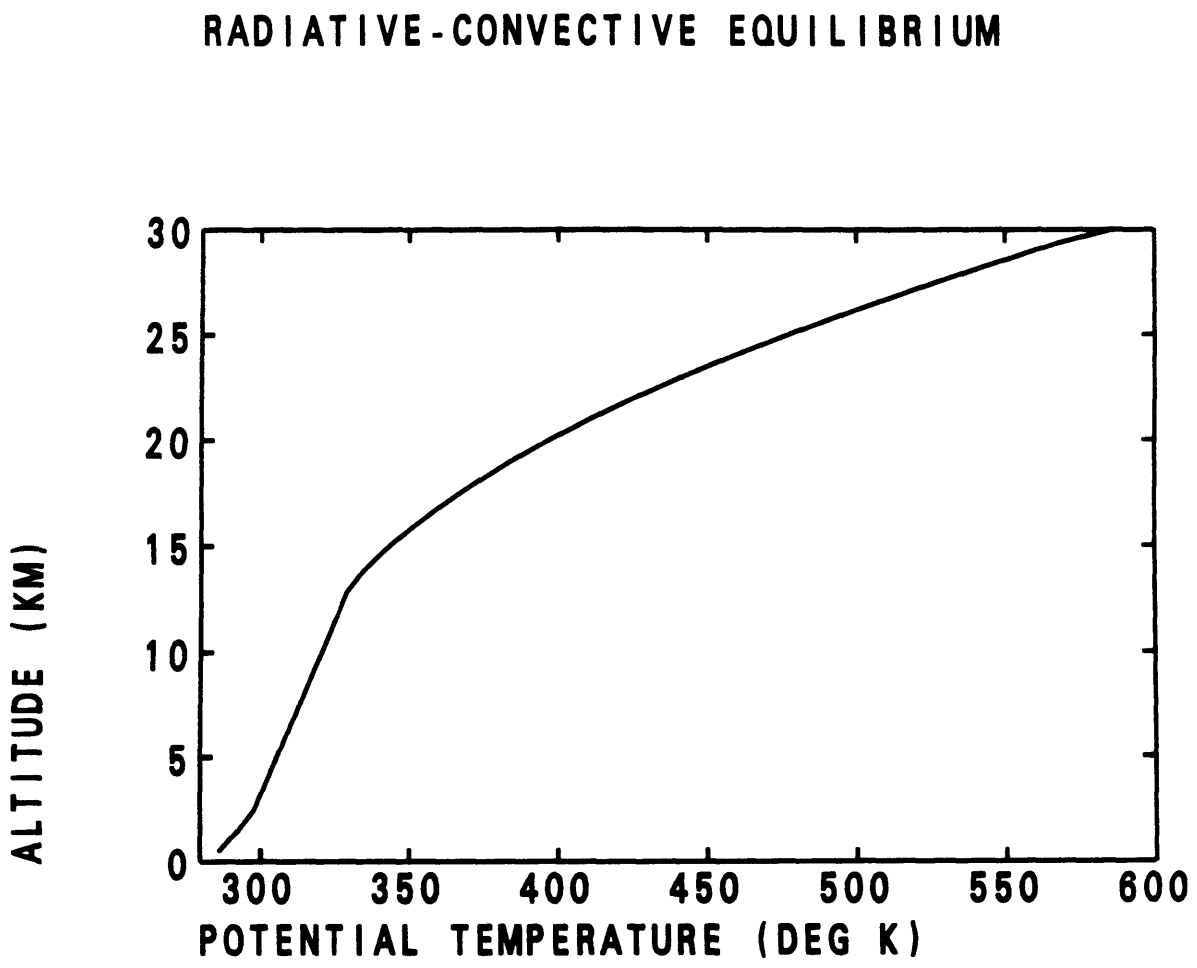

Figure 9.1. Vertical distribution of potential temperature at radiative-convective equilibrium for a uniform surface temperature of 300 K and midlatitude summer profiles of water vapor and ozone.

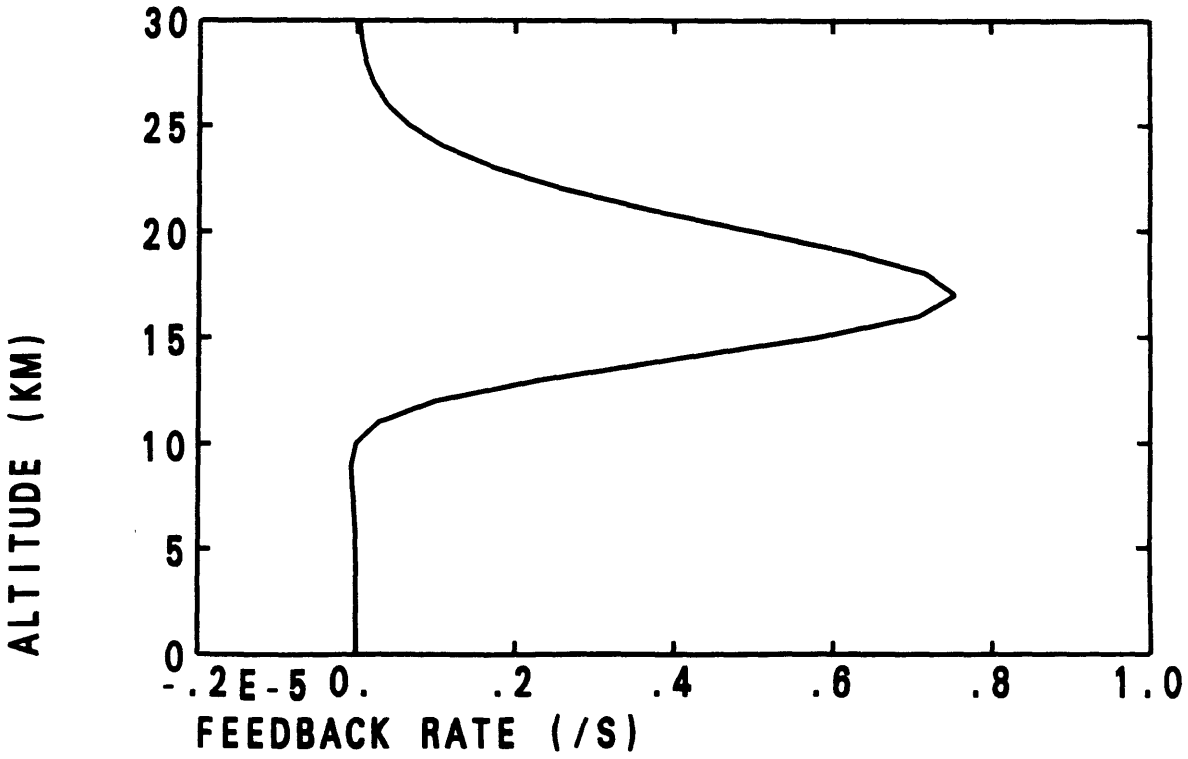

Figure 9.2. Vertical distribution of radiative-dynamical feedback corresponding to a Gaussian absorber distribution with a maximum absorber mixing ratio of 10^{-6} at 10 km and a standard deviation of 5 km. The solar zenith angle is 60°, the solar constant 680 W m^{-2}, the static stability $N = 1.6 \times 10^{-2} s^{-1}$, and the specific absorption is 10^3 m^2 kg^{-1}.

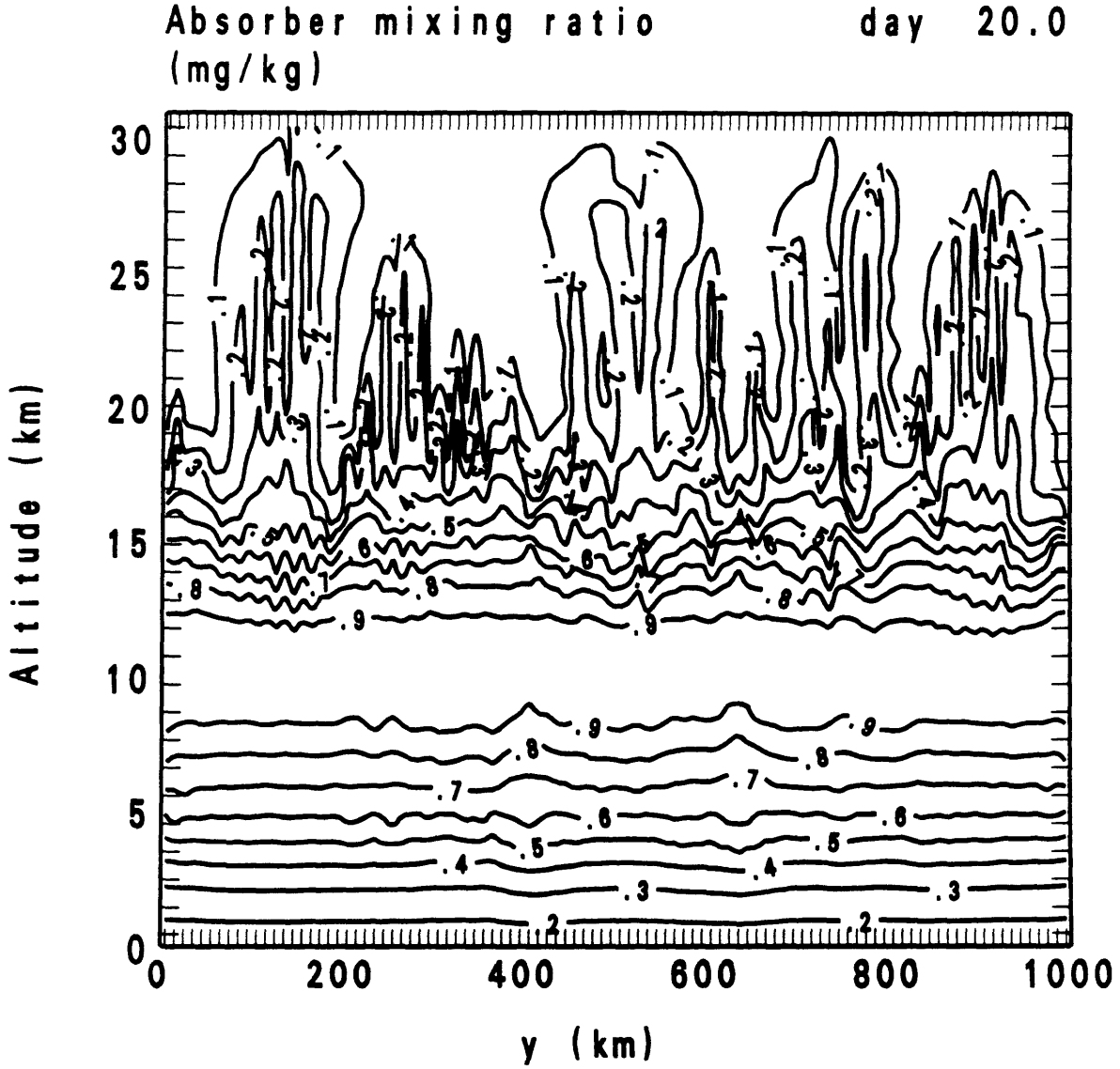

Figure 9.3. Absorber mixing ratio (mg/kg) 20 days following a horizontally uniform injection of absorber with the vertical distribution given by that used for Figure 9.2. The model resolution is indicated by the tic marks.

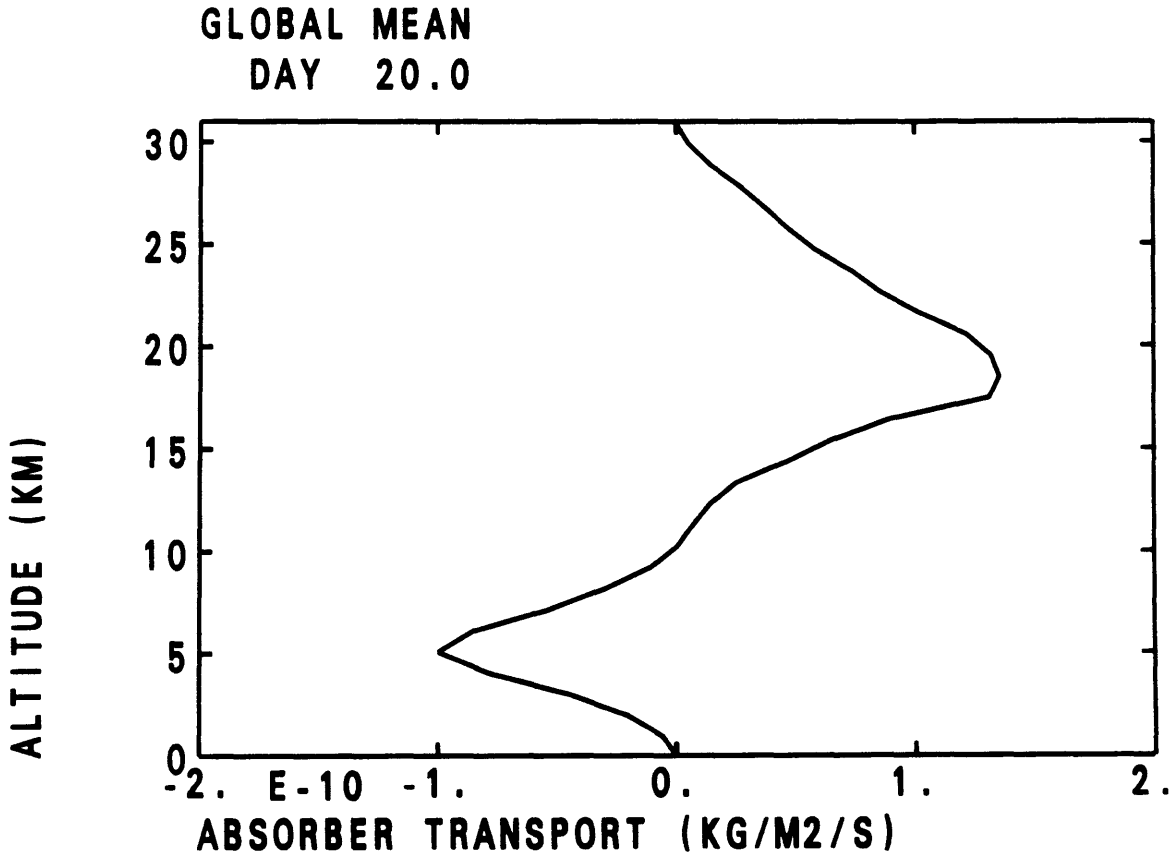

Figure 9.4. Vertical distribution of horizontal mean upward absorber transport 20 days following a horizontally uniform injection of absorber with the vertical distribution given by that used for Figure 9.2.

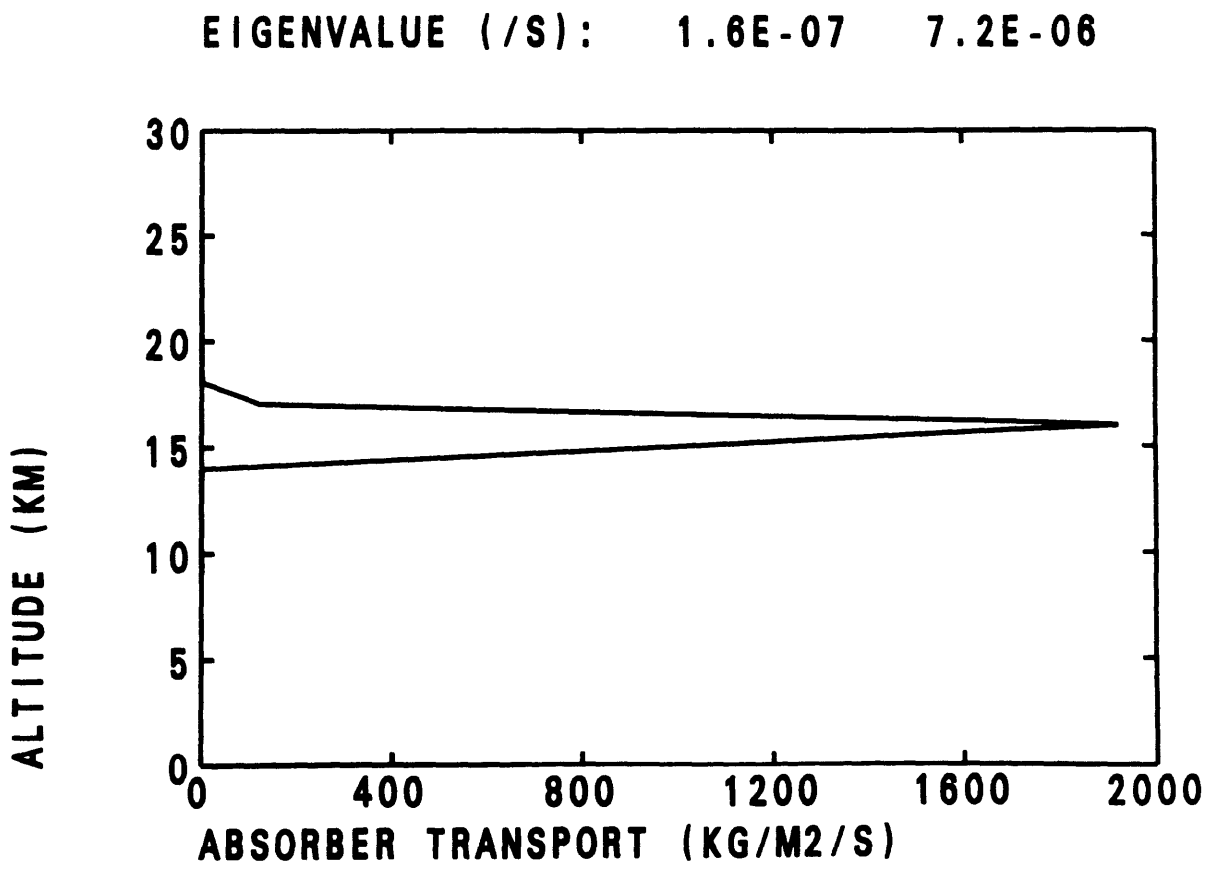

Figure 9.5. Vertical distribution of upward absorber transport for the most rapidly amplifying eigenmode corresponding to zonal and meridional wavelengths of 100 km and the feedback distribution illustrated in Figure 9.2. Based on numerical solution of the eigenvalue problem as described in Chapter 6 and Appendix B. Perturbations in transmissivity are accounted for; the β term is not.

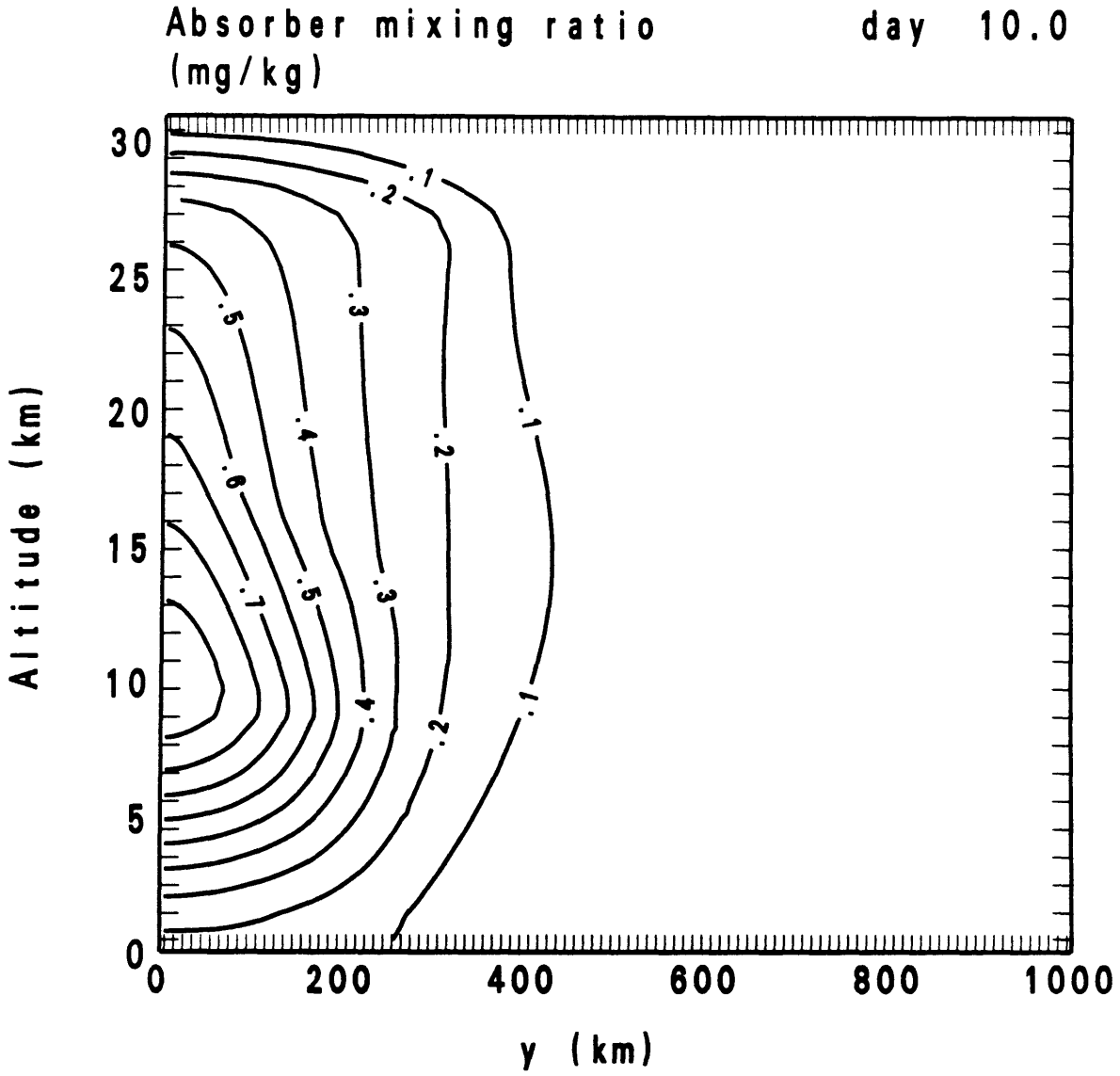

Figure 9.6. Absorber mixing ratio (mg/kg) 10 days following an absorber injection with a Gaussian horizontal distribution (standard deviation 300 km) and the vertical distribution given by that used for Figure 9.2.

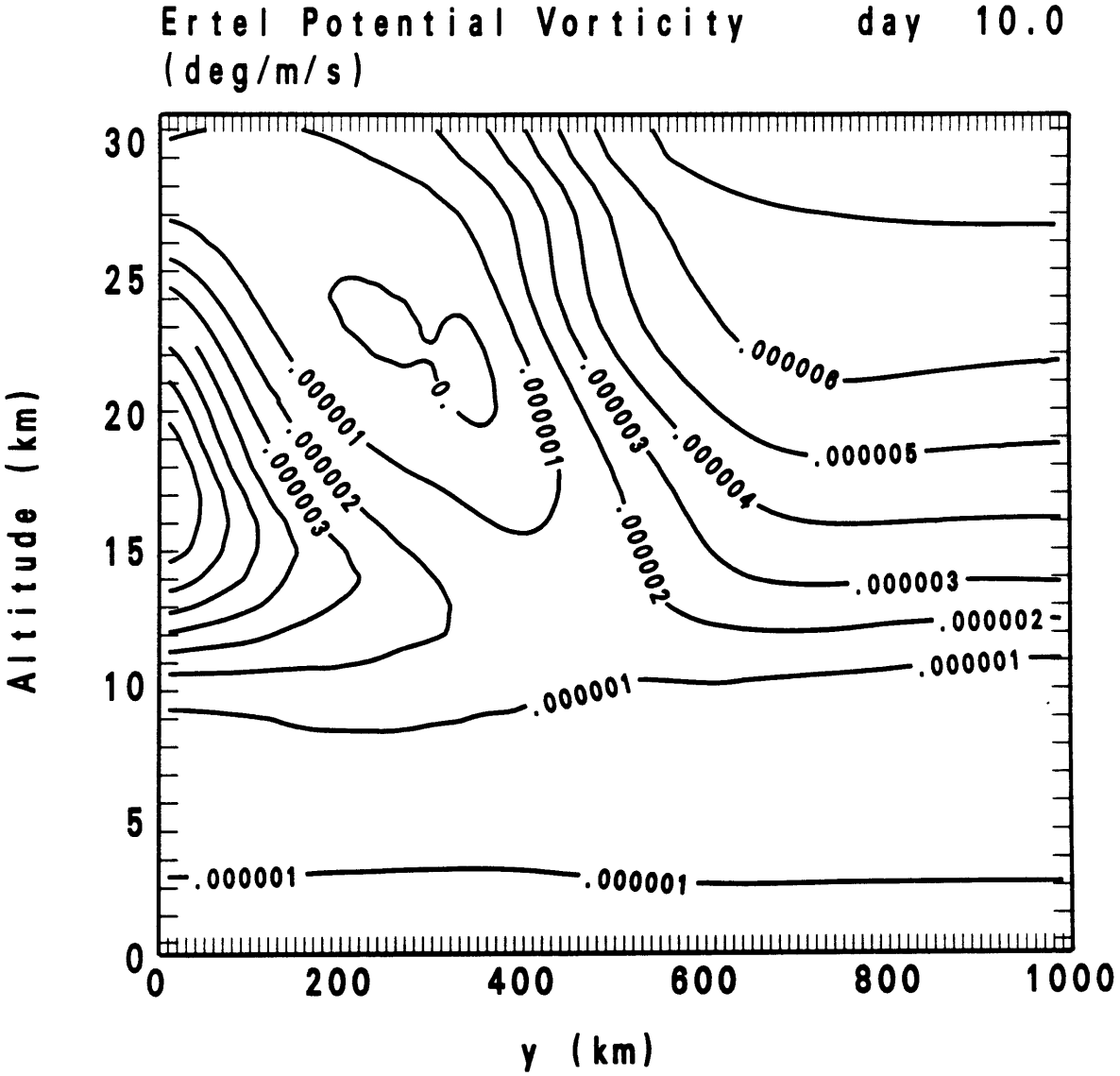

Figure 9.7. Ertel potential vorticity (K m^{-1} s^{-1}), defined as the product of the absolute vorticity and the vertical gradient of potential temperature, 10 days following the absorber injection described for Figure 9.6.

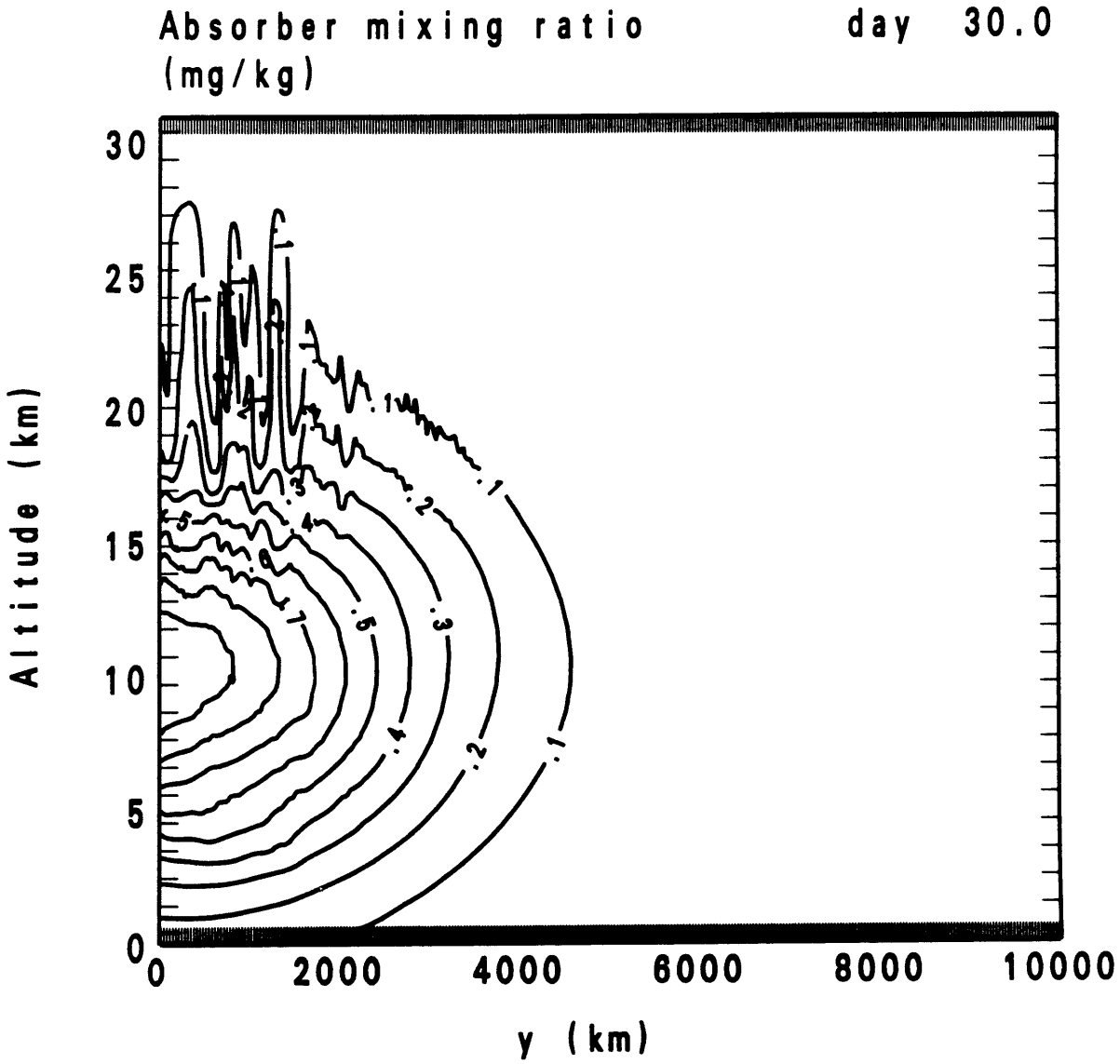

Figure 9.8. Absorber mixing ratio (mg/kg) 30 days following an absorber injection with a Gaussian horizontal distribution (standard deviation 3000 km) and the vertical distribution given by that used for Figure 9.2. The model domain is 10,000 km, with a horizontal grid spacing of 33 km.

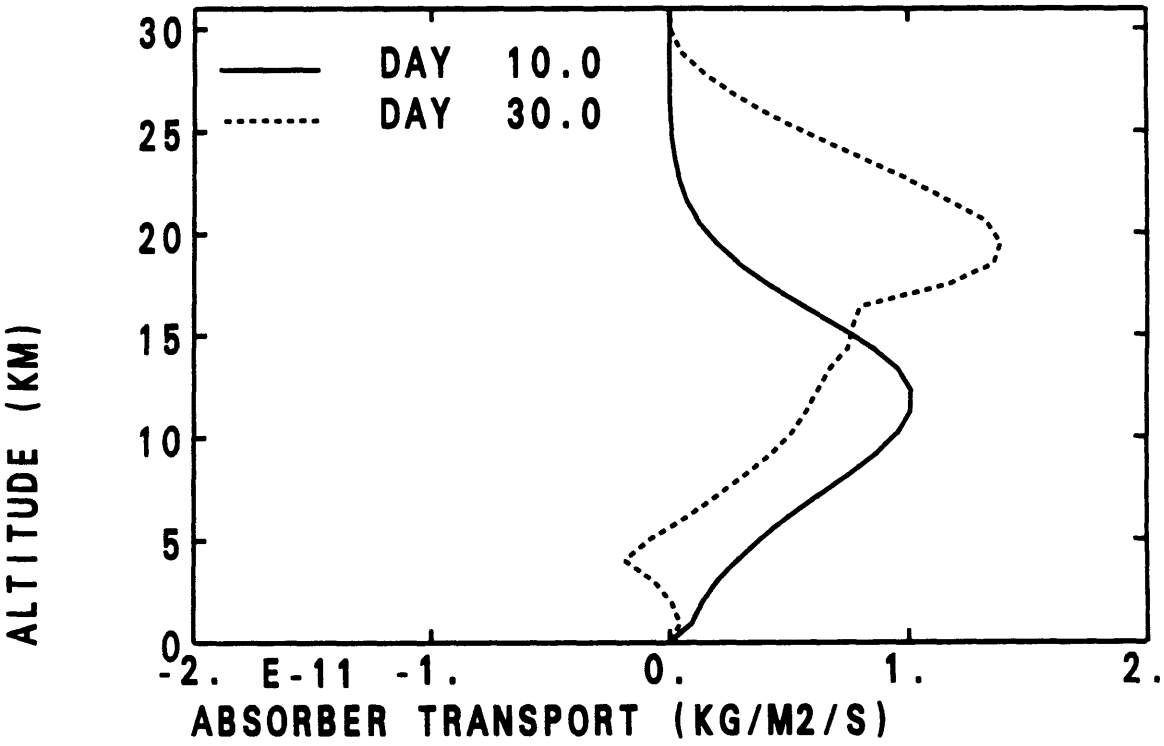

Figure 9.9. Vertical distribution of horizontal mean upward absorber transport 10 (solid line) and 30 (dashed line) days following the absorber injection described for Figure 9.8.

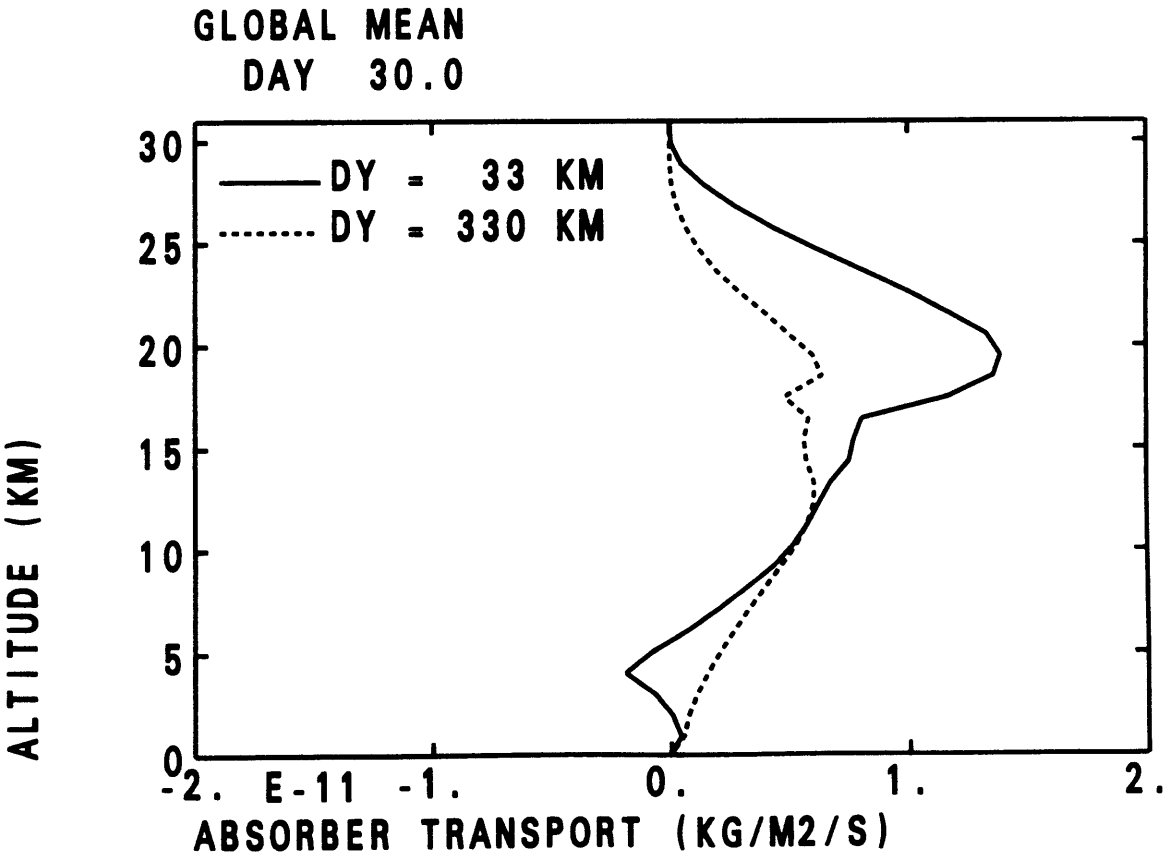

Figure 9.10. Vertical distribution of horizontal mean upward absorber transport 30 days following the absorber injection described for Figure 9.8, for a 33 km model resolution (solid line) and a 330 km resolution (dashed line). The horizontal mixing lengths for the fine and coarse resolution models are 10 km and 100 km, respectively.

10. Application to Morton-Taylor-Turner Theory

One of the underlying assumptions of the preceding chapters is the hydrostatic approximation, which is valid for perturbations in which the horizontal scale is much larger than the vertical scale. Such an approximation is not a necessary condition for unstable radiative-dynamical interactions to occur. In this chapter we consider the application of radiative heating to a classic theory of nonhydrostatic thermal convection, namely the similarity theory of Morton, Taylor, and Turner (1956, hereafter referred to as MTT). We shall find unstable radiative-dynamical interactions, but by a completely different mechanism.

The MTT theory of convection makes three basic assumptions, namely, (i) "that the rate of entrainment at the edge of the plume or cloud is proportional to some characteristic velocity at that height," (ii) "that the profiles of mean vertical velocity and mean buoyancy force in horizontal sections are of similar form at all heights," and (iii) "that the largest local variations of density in the field of motion are small in comparison with some chosen reference of density, this reference being taken as the density of the ambient fluid at the level of the (buoyancy) source." As originally formulated, the theory also relies on the Boussinesq approximation, which permits application to problems of all kinds of gravitational convection. Because we are concerned here only with thermal convection, we shall cast the problem somewhat differently. To retain accuracy for problems involving ascent through several scale heights, the Boussinesq approximation is replaced by the quasi-Boussinesq approximation. Thus, assumption (iii) is replaced by the assumption that the temperature difference between the plume or cloud and the ambient atmosphere is small compared with the ambient temperature.

The MTT theory considers two cases, namely, (i) that of the equilibrium response to a maintained buoyancy source, and (ii) that of the transient response to

an instantaneous buoyancy source. In the former case the response is characterized as a conical plume, whereas in the latter case the response is described as a spherical cloud, or thermal. We are concerned here with the latter case, in which all of the absorber is contained within the cloud. Because the absorption of sunlight is the buoyancy source, we shall drop the instantaneous buoyancy source of MTT.

Consider a sphere of radius r and potential temperature θ rising at velocity w through an ambient atmosphere of potential temperature $\theta_0(z)$. Then the mass, momentum, heat and absorber balances for the sphere can be written

$$\frac{dM}{dt} = SE \tag{10.1}$$

$$M\frac{dw}{dt} = Mb - SwE \tag{10.2}$$

$$M\frac{db}{dt} = -M\left(N^2 w - \frac{RQ}{c_p \rho_0 H}\right) - SbE \tag{10.3}$$

$$M\frac{dq}{dt} = -SqE \tag{10.4}$$

where

$$M = \frac{4}{3}\pi\rho_0 r^3 \qquad \text{mass}$$

$$S = 4\pi\rho_0 r^2 \qquad \text{surface area}$$

$$E = \epsilon\,|w| \qquad \text{entrainment velocity}$$

$$b = \frac{g}{T_0}\,(T - T_0) \qquad \text{buoyancy}$$

$$N^2 = \frac{g}{\theta_0}\,\frac{d\theta_0}{dz} \quad .$$

Defining the total momentum, buoyancy and absorber mass of the cloud as $W = Mw$, $B = Mb$, and $A = Mq$, respectively, (10.1)–(10.4) can be rewritten

$$\frac{d}{dt}\,M^{\frac{1}{3}} = 4\epsilon\left(\frac{4\pi\rho_0}{3}\right)^{1/3}|W| \tag{10.5}$$

$$\frac{dW}{dt} = B \tag{10.6}$$

$$\frac{dB}{dt} = -N^2 W + \frac{RMQ}{c_p \rho_0 H} \tag{10.7}$$

$$\frac{dA}{dt} = 0 \quad . \tag{10.8}$$

The radiative heating Q is determined from Beer's Law. Noting that absorption by a sphere with uniform absorber mixing ratio is independent of solar zenith angle, the transmission of the solar beam through the sphere is

$$T = e^{-\tau \cos \varphi} \tag{10.9}$$

where

$$\tau = 2a\rho_0 qr \tag{10.10}$$

is the optical depth across the diameter of the sphere, and φ is the angle between the solar beam and the radial position vector. Then the total heating of the sphere is

$$\begin{aligned} MQ &= \rho_0 r^2 S_0 \int_0^{2\pi} \int_0^{\pi/2} \left(1 - e^{-\tau \cos\varphi}\right) \cos \varphi \sin \varphi d\varphi \, d\lambda \\ &= \rho_0 \pi r^2 S_0 \left[1 - \frac{2}{\tau^2} + \frac{2(1+\tau)}{\tau^2} e^{-\tau}\right] \quad . \end{aligned} \tag{10.11}$$

Consider two limiting cases. If $\tau \gg 1$ then $MQ \sim \rho_0 \pi r^2 S_0$, so that total heating increases as the cloud grows by entrainment and adiabatic expansion. This might occur in the initial stages of the problem, when the absorber concentration is very high. Eventually, however, the absorber concentration becomes sufficiently dilluted that $\tau \ll 1$. In this case $MQ \sim S_0 a \rho_0 A$. Because the total absorber mass A is conserved, the total heating of the cloud is constant, independent of cloud diameter.

The behavior of solutions for these two limiting cases is quite different. Rather than immediately using the full expression (10.11) for the heating, we shall first consider the two limiting cases. This should help in understanding the behavior of solutions of the general case (10.11).

Suppose first the cloud is optically thick ($\tau \gg 1$), so that the heat balance becomes

$$\frac{dB}{dt} = -N^2 W + \frac{R\pi r^2 S_0}{c_p H} = -N^2 W + \frac{R\pi S_0}{c_p H} \left(\frac{M}{\frac{4}{3}\pi\rho_0}\right)^{2/3} \quad . \tag{10.12}$$

Then the non-dimensional form of the equations is

$$\frac{dM^{*4/3}}{dt^*} = \delta |W^*| \tag{10.13}$$

$$\frac{dW^*}{dt^*} = B^* \tag{10.14}$$

$$\frac{dB^*}{dt^*} = -W^* + M^{*2/3} \tag{10.15}$$

where

$$\delta = \left(\frac{4\pi}{3}\right)^{2/3} \frac{\epsilon R}{3c_p} \frac{S_0}{\rho_0 H^3 N^3} \tag{10.16}$$

$$M^* = M/\left(\rho_0 H^3\right) \tag{10.17}$$

$$W^* = \frac{\left(\frac{4}{3}\pi\right)^{2/3} N^2 c_p}{\pi R S_0 H} W \tag{10.18}$$

$$B^* = \frac{\left(\frac{4}{3}\pi\right)^{2/3} N c_p}{\pi R S_0 H} B \tag{10.19}$$

$$t^* = Nt \quad . \tag{10.20}$$

The system of equations (10.13)–(10.15) is linearly unstable. To see this, linearize the equations about $M^* = M_0$. Then for solutions of the form $\exp(\lambda^* t^*)$ the characteristic equation is (assuming $W^* > 0$)

$$\lambda^*(\lambda^{*\,2} + 1) = \frac{1}{2} M_0^{-2/3} \delta \quad . \tag{10.21}$$

The sum of the roots of the characteristic equation is zero, indicating that if any modes are damped, at least one amplifies. Using $\epsilon \sim 0.3$ from MTT and typical terrestrial values for R, c_p, S_0, ρ_0, H and N yields $\delta \sim 10^{-4}$. Thus, unless $M_0^{2/3}$ is extremely small we can conclude that $\lambda^* \sim \frac{1}{2}\delta M_0^{-2/3}$, or in dimensional terms

$$\lambda \sim \left(\frac{4\pi}{3}\right)^{2/3} \frac{\epsilon R}{6c_p} \frac{S_0}{\rho_0 H^3 N^2} \left(\frac{\rho_0 H^3}{M}\right)^{2/3} \sim \left(\frac{H}{r}\right)^2 \cdot 10^{-6} \mathrm{s}^{-1} \tag{10.22}$$

which yields e-folding times of a few minutes for $H/r \sim 100$. Note that the factor $RS_0/(c_p \rho_0 N^2 H^3)$ also appears in the modal instability theory (see (1.6)).

The physical mechanism of the instability is quite simple. The cloud grows through entrainment. Because the cloud is optically thick, the larger surface area of the cloud increases energy absorption, which increases buoyancy, and hence total momentum, and hence entrainment. Thus, it appears that entrainment ($\epsilon > 0$) is necessary for the instability. However, because the cloud surface area can also increase through adiabatic expansion, instability is also possible in the absence of entrainment. To see this, consider the mass balance in terms of the cloud volume V,

$$\rho_o \frac{dV}{dt} = \frac{dM}{dt} + \frac{W}{H} \tag{10.23}$$

where $V = \frac{4}{3}\pi r^3$. In the absence of entrainment the total mass is conserved, so that (10.23) reduces to

$$\frac{dV}{dt} = \frac{W}{\rho_o H}$$

which is similar in form to (10.5). When the optical depth of the cloud is large, the resulting non-dimensional set of equations is similar to (10.13)–(10.15), with the parameter δ defined

$$\delta = (\frac{4\pi}{3})^{-2/3} \frac{\pi R S_o}{\rho_o c_p N^3 H^3} \tag{10.25}$$

which differs only slightly from (10.16) with ϵ order unity. The dimensional growth rate is approximately

$$\lambda \sim \frac{1}{2} \frac{RS_o}{\rho_o c_p H^3 N^2} \frac{H}{r} \sim \frac{H}{r} \cdot 2 \times 10^{-6} s^{-1} \tag{10.26}$$

which is considerably slower than the growth rate due to entrainment if the cloud radius is much less than the scale height H.

The underlying assumption here is that all of the absorber is lofted with the cloud. However, such an assumption is probably unreasonable in the optically thick case. Much of the absorber mass would be shielded from sunlight, and hence could absorb no solar energy. Unless there is compelling evidence that the cloud would

remain well mixed, it is more likely to expect only the upper optical depth unity of the absorber mass to be lofted.

The remaining roots of the characteristic equation are approximately $\lambda \sim \pm i\, N$ provided $M_0^{2/3}$ is much larger than δ, which for terrestrial conditions is satisfied if r is much larger than about 50 m. These roots correspond to damped buoyancy oscillations, with the non-dimensional damping rate equal to the growth rate of the amplifying mode, i.e. $1/2\delta M_0^{-2/3}$, which for sufficiently large clouds is much smaller than the oscillation frequency. However, for sufficiently small clouds the damping rate may be as large as the buoyancy oscillation frequency.

For the optically thin cloud ($\tau \ll 1$), the heat balance becomes

$$\frac{dB}{dt} = -N^2 W + \frac{RS_0 aA}{c_p H} \quad . \tag{10.27}$$

From (10.27) and the momentum equation (10.6) we find the particular solution $B_p = 0$, $W_p = RS_0 aA/(c_p H N^2)$, which represents an exact balance between the constant radiative heating and the steady adiabatic cooling. However, because the cloud mass continues to grow through entrainment the vertical velocity $w = W/M$ steadily decreases with time.

The homogeneous solution of (10.27) oscillates at the Brünt-Vaisala frequency. Thus, full solutions are characterized by oscillations in buoyancy and vertical velocity which decay to zero.

The general case in which the cloud begins optically thick but becomes optically thin through dilution by entrainment is illustrated in Figure 10.1, which shows time series of the buoyancy, vertical velocity, cloud radius, cloud altitude, cloud optical depth and total momentum Mw determined numerically for a cloud of initial radius 1 km and initial mass 10^5 kg [which is typical of urban fire simulations for a nuclear war (Penner et al., 1986)]. The usual values for the solar constant,

specific absorption and Brünt-Vaisala frequency have been adopted. For simplicity, we have assumed that all of the absorber mass remains within the cloud.

Initially the cloud is optically thick, so that the total momentum grows exponentially with time. Because the initial cloud radius is much larger than 50 m, oscillations in the vertical velocity and buoyancy are evident in the numerical solutions (integrations initialized with optically thick clouds of radius much less than 50 m do not exhibit such oscillations).

After about one day (of sunlight) the cloud is sufficiently diluted that it is no longer optically thick. The instability mechanism is no longer operative, and the total momentum of the cloud approaches the value of the particular solution W_p. However the cloud continues to grow, with the radius exceeding 7 km after one day. The oscillations in buoyancy and vertical velocity decay, and the vertical velocity steadily decreases as the cloud mass increases.

As discussed previously, it is probably unreasonable to expect all of the absorber mass to remain within the cloud when it is optically thick. Even in the case of the optical thin cloud, however, we find that substantial lofting occurs. For example, for a 1 km cloud containing only 10^3 kg absorber mass, the absorption optical depth is initially only 0.5, but the cloud is lofted to 3 km within one day (of sunlight).

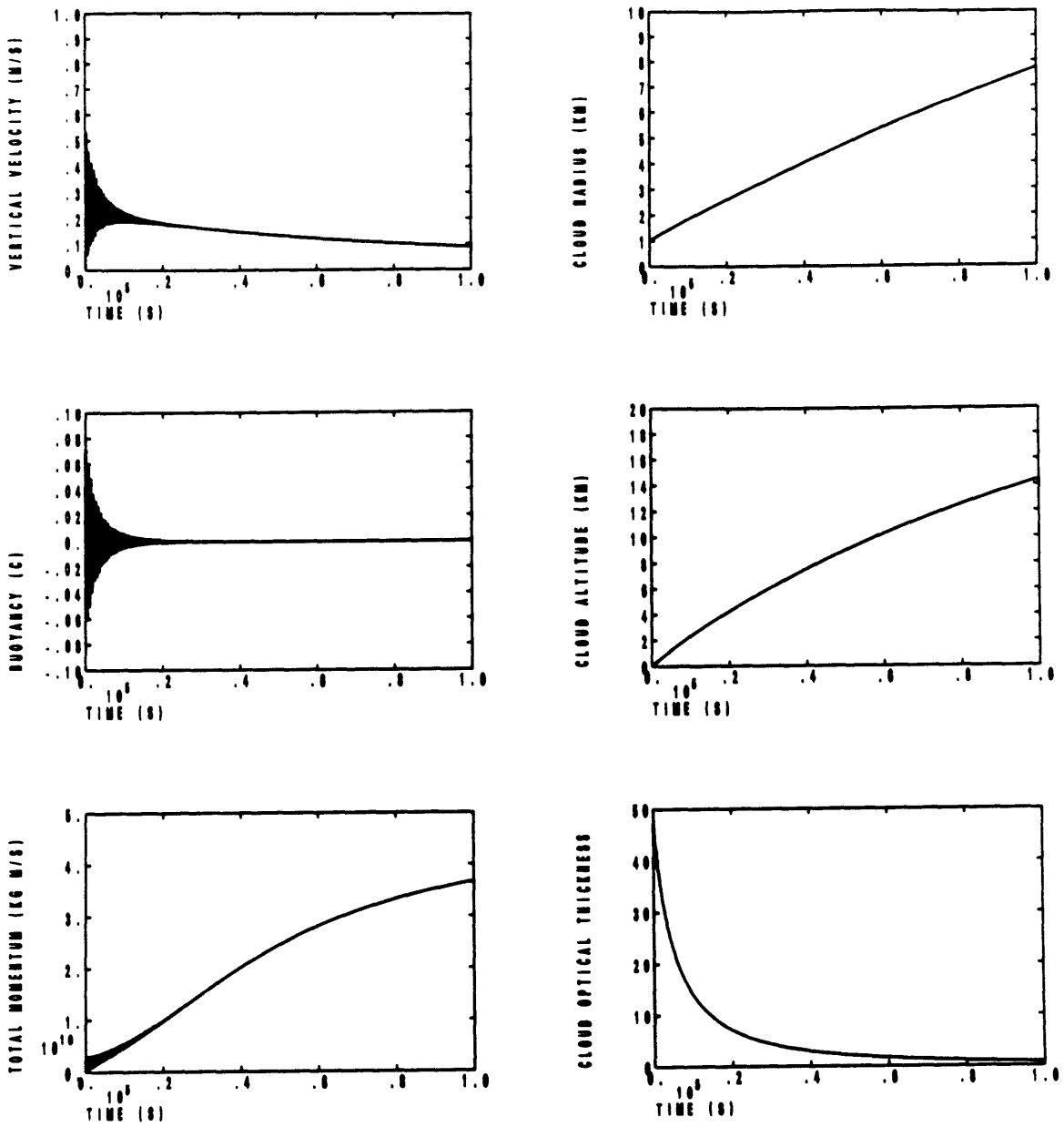

Figure 10.1. Evolution of vertical velocity w, buoyancy $T - T_0$, total vertical momentum W, cloud radius r, cloud altitude z, and cloud optical thickness τ for 10^5 s following the injection of 10^5 kg of absorber mass into a spherical cloud of radius 1 km. The solar constant is 1360 Wm^{-2}, the specific absorption 10^3 m^2 kg^{-1}, and the Brünt-Vaisala frequency is 10^{-2} s^{-1}. The entrainment parameter ϵ is 0.3, and all absorber mass is assumed to remain in the cloud. Rapid buoyancy oscillations are evident in the time series of vertical velocity and buoyancy. Based on the application of radiative heating to the Morton-Taylor-Turner theory of thermal convection.

11. Application to Planetary Atmospheres

The simplicity of the expression (1.1) for the radiative-dynamical feedback rate invites application of the theory to planetary atmospheres. None of the planetary atmospheres are perfectly transparent to solar radiation, so that one might expect the possibility of a feedback between the dynamical circulation and the radiative heating associated with solar absorption. Although scattering dominates absorption for most of the aerosols in planetary atmospheres, we shall assume that the absorption optical depth of each planetary atmosphere exceeds unity at least in certain circumstances. In addition, we shall assume that the longwave radiative effects of such aerosols are less important than the effects of solar absorption (we present arguments in this chapter in support of such an assumption).

For the Venus atmosphere potential absorbers are haze particles at altitudes of 70–90 km and cloud droplets at altitudes between 50 km and 70 km. The layer of haze particles is optically quite thin, with an extinction optical depth of 0.2–1 at 0.6 μm (Esposito, et al., 1983); the absorption optical depth is presumably much smaller. The layer of sulfuric acid clouds is optically thick, with an extinction optical depth of about 40. Moreover, the cloud droplets are much smaller than those on Earth, with mode radii of typically 1 μm. The infrared radiative properties of such aerosols are therefore no more important than the solar properties. Indeed, because the Venus atmosphere is composed primarily of CO_2, clouds have little direct effect on the infrared heating rates. It should be noted, however, that because the cloud droplets primarily scatter solar radiation, the absorption optical depth of clouds on Venus is quite low in spite of the large extinction optical depth.

For the Earth atmosphere extinction optical depths due to aerosols are usually quite small. However, on occasion forest fires, volcanic eruptions, dust storms or perhaps asteroid collisions can generate enough aerosol mass to produce large local

extinction optical depths. The absorption optical depths of all but the most speculative scenarios is usually quite small. A more plausible (but hopefully unlikely) source of strong absorption is smoke generated by urban fires resulting from a nuclear war. In this scenario hemispheric mean absorption optical depths of about one have been projected. Moreover, the infrared absorptivity of such aerosols is typically much less than the solar absorptivity, and scattering is typically of less importance than absorption, so that smoke particles are the ideal aerosol for generating a shortwave radiative-dynamical instability.

The Martian atmosphere is usually free of solar absorbers, but periodically becomes polluted by dust storms that occasionally spread to cover the entire globe. These storms are an excellent test of the radiative-dynamical instability mechanism.

In the absence of atmospheric probes, present knowledge of aerosols in the Jupiter atmosphere is somewhat speculative. The evidence seems to suggest the presence of a layer of small particles in the upper troposphere, with a visible extinction optical depth of several, above an optically thicker layer of larger particles (West, et al., 1986). Whereas the upper layer is believed to be largely transparent in the infrared, the lower layer is not. Given the dominance of scattering over absorption for liquid NH_3 particles it is unlikely that the upper cloud layer absorbs much sunlight. Radiative heating rates in the lower cloud layer may be dominated by longwave component. Moreover, latent heat release in such clouds is likely to be important. Thus, solar absorption cannot be easily isolated from other processes in the Jupiter atmosphere.

Models of the Saturn atmosphere are even more speculative, with little agreement among researchers on the suggested presence of a stratospheric haze layer or on the vertical extent or optical properties of the visible tropospheric cloud layer. The Titan atmosphere is characterized by a photochemical haze in the stratosphere (Hunten et al., 1984), with particles of radius 0.1 μm. The possible presence of

tropospheric methane clouds is speculative at present because of the obscuration of the troposphere by the stratospheric smog.

Considering how little is known regarding the presence of solar absorbers in the planetary atmospheres it might appear premature to speculate on the possibility of strong radiative-dynamical interactions. Speculation, however, has played an important role in the study of planetary atmospheres. Moreover, the radiative-dynamical theory developed here does not require the specific details of solar absorption for comparison of the feedback in the planetary atmospheres. We shall take a general approach by evaluating the potential for radiative-dynamical feedback for each atmosphere. Whether each atmosphere contains sufficient strong solar absorbers to realize the potential remains to be seen, but an inter-planetary comparison of the potential for strong radiative-dynamical interaction should be of some interest.

For the purpose of comparison consider again the exponential absorber distribution. Neglecting perturbations in transmissivity, the maximum feedback rate for such a distribution occurs at the altitude where the absorption optical depth equals the cosine of the solar zenith angle, and is given by the expression

$$\alpha_{max} = 0.37\ \alpha_0\ \mu \frac{H}{h}\left(1 + \frac{H}{h}\right) \tag{11.1}$$

where

$$\alpha_0 = \frac{RS_0}{c_p \rho_0 N^2 H^3} \tag{11.2}$$

is a nominal feedback rate. For a given absorber mixing ratio scale height h, α_0 controls the magnitude of the maximum feedback rate (provided the optical depth exceeds μ, the cosine of the solar zenith angle). The radiative-dynamical feedback rate for planetary atmospheres can therefore be readily compared by evaluating α_0 for each planet. Values of S_0, ρ_0, N^2, H, and α_0 for Venus, Earth, Mars,

Jupiter, Saturn, and Titan are listed in Table 11.1 (the thermodynamic ratio R/c_p is approximated as 0.286 for each planet).

Note first that the insolation values represent the solar constant at the top of the planetary atmosphere. Scattering of sunlight either by the surface, the absorber, or by other atmospheric constituents has been neglected. This tends to overestimate the amount of solar radiation available if the absorber lies below the top of the clouds, and underestimate solar radiation above the top of the clouds. However, the difference between the solar constants of the various planets is typically larger than the bias introduced by such a treatment.

Note also that, because of the strong dependence of atmospheric density ρ_0 and static stability N^2 on altitude, the value of α_0 for each planetary atmosphere depends strongly on altitude. Indeed, α_0 generally increases with altitude as the density decreases. However, at increasingly high altitudes the tenuous atmosphere is incapable of supporting absorption optical depths of order unity, so that the actual feedback rate would be considerably less than α_{max}. To compare single values of α_0 for each planet, care is therefore required in selecting reference levels that are consistent. For the purpose of comparison, we have chosen to evaluate α_0 at reference levels near the planetary tropopause. This choice is based on the premise that the tropopause marks the transition between the troposphere, where strictly dynamical processes dominate radiative processes, and the stratosphere, where radiative processes dominate dynamical processes. Expressed in terms of time scales, we expect the dynamical time scale to be shorter than the radiative relaxation time in the troposphere, but longer in the stratosphere. The importance of the radiative-dynamical feedback is evaluated by comparing the feedback time α^{-1} to the purely dynamical (advective) and purely radiative (infrared) relaxation times at the tropopause. The tropopause pressure for each planet is also listed in

Table 1. To evaluate the static stability we have, in the face of considerable uncertainty in the observations, resorted to the simple assumption that the atmosphere is locally isothermal. Those cases in which the static stability is known with some confidence will be considered separately.

From Table 1 we find that the tropopause value of α_0 for the terrestrial planets is generally much larger than that for the Jovian planets (including the satellite Titan). The most obvious explanation for this is the much weaker insolation for the Jovian planets. Additionally, the density scale height for the Jovian planets is typically somewhat larger, due to their different composition (for Jupiter and Saturn) or lower gravitational constant (for Titan).

Atmospheric density plays an important role in determining the value of α_0 for the terrestrial planets, with the nominal feedback rate more than two orders of magnitude stronger for Mars than for Earth, mainly because of lower density of the Martian atmosphere. This does not, however, imply that radiative-dynamical feedback is necessarily more important for Mars than for Earth. The Martian atmosphere above the 0.3 mb level may not be thick enough to sustain an absorption optical depth of unity (against, say, gravitational settling), so that the actual feedback rate for an exponential absorber distribution may be less than α_{max}. Moreover, radiative relaxation for the thin Martian atmosphere is also much more rapid than for the Earth tropopause. However, we shall now demonstrate that, except under certain conditions, radiative-dynamical feedback can dominate radiative relaxation, independent of atmospheric density. To see this, consider the standard definition of the radiative relaxation time (Leovy, 1985)

$$\tau_r = \frac{c_p}{R}\frac{pH}{\epsilon\sigma T^4} \tag{11.3}$$

where σ is the Stefan-Boltzmann constant and ϵ is the thermal emissivity. According to (11.3), the radiative relaxation time is proportional to density, and hence

should be much less for Mars than for Earth (assuming comparable thermal emissivities). Comparing the radiative relaxation time with α_0, we find that the product can be expressed

$$(\alpha_0 \tau_r)^{-1} = \frac{\rho H^3 N^2 \epsilon \sigma T^4}{pHS_0} \sim \frac{H}{\theta} \frac{\partial \theta}{\partial z} \tag{11.4}$$

which is less than unity except in the presence of an inversion (for an isothermal atmosphere (11.4) reduces to $R/c_p = 2/7$). Thus, the radiative-dynamical feedback time can be much shorter than the thermal relaxation time; equivalently, radiative-dynamical feedback for an exponential absorber mixing ratio profile can dominate infrared radiative damping, the only constraints being that (a) the solar zenith angle is small, (b) an inversion not exist, (c), the absorber mixing ratio scale height be less than or comparable to the density scale height, and (d) the absorption optical depth from the top of the atmosphere be comparable to the cosine of the solar zenith angle, i.e., unity. Thus, the more rapid radiative relaxation of the Martian atmosphere will not necessarily dominate the radiative-dynamical feedback, so that radiative-dynamical feedback is potentially as important on Mars as on Earth, and is certainly faster.

If the radiative-dynamical feedback is to be important in an atmosphere the nominal feedback time α_0^{-1} must be at least as fast as the dynamical time scale. For Venus and Earth the nominal (assuming the absorber scale height is comparable to the density scale height) feedback time is comparable to the dynamical time scale

$$\tau_d = L/U \tag{11.5}$$

which is about 10^5 s for both planets at the tropopause. For Mars the nominal feedback time at the tropopause is much shorter than the dynamical time scale (also about 10^5 s). However, at the surface of Mars, where the atmospheric density is much larger than at the tropopause level (an effect on the feedback rate that dominates the weaker static stability of the Martian troposphere) the nominal

feedback time is comparable to the dynamical time. The nominal feedback time at the surface of Earth is somewhat longer than at the tropopause because the effect of the larger density and the larger density scale height combine to exceed the effect of the weaker static stability.

For the Jovian planets, the nominal radiative-dynamical feedback time is, as we have demonstrated, shorter than the radiative relaxation time, but at the tropopause is clearly much longer than the dynamical time scale. However, within the troposphere of both Jupiter and Saturn the static stability is thought to be quite small, so that radiative-dynamical feedback in the troposphere of Jupiter and Saturn may be much faster than that indicated in Table 1, perhaps as fast as the dynamical time scale. In that case, the radiative-dynamical interaction must compete with other energy release mechanisms, which also develop faster with decreasing static stability. In the lower troposphere of these planets the atmospheric density is probably large enough to eliminate the feedback as an important process.

To summarize, we have found that as might be expected the potential for radiative-dynamical feedback is strongest for those planets closest to the sun. We have shown that the feedback can dominate infrared radiative relaxation for all planets, but that purely dynamical processes in the Jovian atmospheres are probably of greater importance than the feedback. Mars, with its tenuous atmosphere, is probably the most likely candidate for radiative-dynamical instabilities. The potential feedback in the Venus atmosphere is also quite rapid which, given the horizontal uniformity of Venus clouds (a necessary assumption of the present theory), suggests that Venus is also a strong candidate for further application of the instability theory.

Table 11.1. Radiative-dynamical feedback parameters for planetary atmospheres.

	$S_0(Wm^{-2})$	$p_{trop}(mb)$	$\rho_0(kg\ m^{-3})$	$H(m)$	$N^2(s^{-2})$	$\alpha_0(s^{-1})$
Venus	2600.	130.	0.25	5×10^3	4×10^{-4}	6×10^{-5}
Earth	1360.	200.	0.3	6×10^3	5×10^{-4}	1×10^{-5}
Mars	600.	0.3	0.001	10×10^3	1×10^{-4}	2×10^{-3}
Jupiter	50.	100.	0.02	20×10^3	3×10^{-4}	3×10^{-7}
Saturn	15.	100.	0.02	40×10^3	8×10^{-5}	4×10^{-8}
Titan	15.	100.	0.4	20×10^3	2×10^{-5}	7×10^{-8}

12. Summary

The theory developed here demonstrates the potential for unstable radiative-dynamical interactions that are strong enough to compete with other purely dynamical instability mechanisms and with nonmodal forms of absorber transport. Two distinct modes have been identified, described as advective and propagating modes, respectively.

In the advective mode, an instability typically arises when the absorber mixing ratio decreases with altitude. Perturbations in absorber concentration, shortwave radiative heating, vertical motion and temperature are all in phase. Propagation with respect to the mean flow is weak. Amplification is most rapid for modes which are short and deep, i.e., for modes with horizontal scales much less than the internal deformation radius.

Propagating modes such as Rossby and inertia-gravity waves become unstable when the absorber mixing ratio increases with altitude. High absorber concentrations and strong heating lag downward motion by about one quarter cycle; warm temperatures lag the heating by one quarter cycle, and hence are in phase with upward motion. Because strong propagation is necessary to maintain the proper phase relationships for energy release, the growth rate of propagating modes is typically much less than the frequency of oscillation. This constraint limits the growth rate of the slowly propagating Rossby waves.

The fundamental parameter that emerges is the rate of radiative-dynamical feedback, defined as

$$\alpha \equiv -\frac{RS_0 a\overline{T}}{c_p N^2 H}\,\frac{\partial \overline{q}}{\partial z} \quad . \tag{12.1}$$

The growth rate of unstable disturbances has been found in most instances to be bounded by the magnitude of the feedback rate, so that α characterizes the growth rate.

This basic theory has been extended to account for a number of complicating factors, including the effects of perturbations in transmissivity (associated with absorber perturbations at higher altitudes), dissipative processes, basic state vertical shear, and scattering.

Perturbations in transmissivity can either enhance or suppress the radiative-dynamical instability. In all cases such perturbations alter the phase relationship between the radiative heating and the absorber concentration. For absorber perturbations with vertical wavelengths exceeding the density scale height, perturbations in transmissivity can actually reverse the sign of the correlation between the local heating and absorber concentration. This changes the sign of the effective radiative-dynamical feedback rate, so that the propagating modes become unstable when the absorber mixing ratio decreases with altitude, and the advective mode becomes unstable when the absorber mixing ratio increases with altitude. For shallow absorber perturbations, the magnitude of the correlation between the local absorber concentration and heating rate decreases when perturbations in transmissivity are important. In this case the effect on the growth rate depends on the direction of phase propagation. Growth of downward-propagating Rossby waves is enhanced by perturbations in the transmissivity, but the growth rate never exceeds the effective feedback rate, defined by (3.13).

Dissipative processes generally reduce or eliminate the instability. Absorber damping (due to gravitational settling, precipitation scavenging, or photochemical processes) is most effective in suppressing the growth of the advective mode, with the instability eliminated when the absorber damping rate exceeds the radiative-dynamical feedback rate. Mechanical damping suppresses the growth of the inertia-gravity modes, but can actually enhance the amplification of the advective mode. Thermal dissipation reduces the growth rate of all modes when the dissipation rate exceeds the magnitude of the feedback rate.

Vertical shear in the basic state zonal wind can either enhance or reduce the growth rate of the most rapidly amplifying modes. Weak shear suppresses the instability for all but the shortest modes (i.e., those for which the growth rate in the absence of shear is insensitive to vertical wavelength). Strong shear, however, introduces baroclinic instability, so that growth rates eventually increase with increasing shear. In some instances the growth rate of the most unstable mode (for a given horizontal wavelength) is actually greater than both the feedback rate and the adiabatic baroclinic growth rate, but never exceeds the sum of the two rates.

Scattering of sunlight also either enhances or suppresses the growth of unstable modes, depending on the solar zenith angle. If the sun is overhead (small solar zenith angle) scattering increases the path length of photons, thereby enhancing absorption and hence the radiative-dynamical feedback rate; the growth rate is enhanced by scattering in this case. Because some photons are scattered to space, reducing the available sunlight, scattering tends to reduce the growth rate for large solar zenith angles; in this case the path length of the direct beam is already long, so that scattering only serves to reduce the effective solar constant, and hence the absorption of sunlight.

The effect of relaxing the assumption of horizontal uniformity in the basic state has also been addressed. When the initial absorber distribution is inhomogeneous, nonmodal forms of absorber transport become potentially important. Indeed, in numerical simulations nonmodal transport dominates early in the integration, but for sufficiently broad absorber distributions the modal instability eventually emerges as a significant absorber transport mechanism. This suggests that previous simulations of Martian dust storms and the "nuclear winter" smoke lofting phenomenon, using relatively coarse mesh models, may have underestimated the absorber transport.

In a brief digression, radiative feedback is applied to the Morton-Taylor-Turner theory of thermal convection. Assuming that all of an initial absorber injection is retained by a rising spherical cloud, it is shown that normal mode instabilities arise due to the increase in energy absorption as the cloud grows through entrainment and adiabatic expansion. The increased energy absorption raises the buoyancy, thereby accelerating the rise of the cloud, which in turn increases the rate of entrainment. The cloud eventually becomes optically thin, with the total vertical momentum of the cloud stabilizing at a value determined by the balance between the constant solar heating of the cloud and the adiabatic cooling associated with ascent.

Finally, application of the basic radiative-dynamical instability theory to planetary atmospheres demonstrates the obvious result that the feedback is potentially more important for those planets closest to the sun. One significant conclusion from the analysis is that thermal radiative relaxation must, under certain conditions, be weaker than the solar feedback, independent of atmospheric density. This suggests that Mars is a prime candidate for radiative-dynamical interaction, in spite of its short radiative relaxation time.

In conclusion, interactions among solar absorption, dynamical circulations, and inhomogeneous absorber distributions yield a variety of instability mechanisms. Amplification of disturbances can be quite rapid, with growth rates in some cases competitive with those associated with baroclinic instability. Further work is required to determine whether such interactions play an essential or auxiliary role in any geophysical phenomenon.

References

Arakawa, A., and V. R. Lamb, 1977: Computational design of the basic dynamical process of the UCLA general circulation model. *Methods in Computational Physics, 17*, J. Chang, Ed., Academic Press, 173–265.

Arakawa, A., and M. J. Suarez, 1983: Vertical differencing of the primitive equations in sigma coordinates. *Mon. Wea. Rev., 111*, 34–45.

Asselin, R. A., 1972: Frequency filter for time integrations. *Mon. Wea. Rev., 100*, 487–490.

Charney, J. G., 1947: The dynamics of long waves in a baroclinic westerly current. *J. Meteor., 4*, 135–162.

Covey, C., S. H. Schneider, and S. L. Thompson, 1984: Global atmospheric effects of massive smoke injections from a nuclear war: Results from general circulation model simulations. *Nature, 308*, 27–31.

Eady, E. T., 1949: Long waves and cyclone waves. *Tellus, 1*, 33–52.

Emanuel, K. A., 1983: The Lagrangian parcel dynamics of moist symmetric instability. *J. Atmos. Sci., 40*, 2368–2376.

Esposito, L. W., R. G. Knollenberg, M. Y. Marov, O. B. Toon and R. P. Turco, 1983: The clouds and hazes of Venus. Pp. 484–564 In Venus, D. M. Hunten, L. Colin, T. M. Donohue and V. I. Moroz, Ed., Univ. Arizona Press, Tucson.

Farrell, B. , 1984: Modal and nonmodal baroclinic waves. *J. Atmos. Sci., 41*, 668–673.

Fels, S. B., 1982: A parameterization of scale-dependent radiative damping rates in the middle atmosphere. *J. Atmos. Sci., 39*, 1141–1152.

Gierasch, P. J., and R. M. Goody, 1973: A model of a Martian Great Dust Storm. *J. Atmos. Sci., 30*, 169–179.

Gierasch, P. J., A. P. Ingersoll, and R. T. Williams, 1973: Radiative instability of a cloud planetary atmosphere. *Icarus, 19*, 473–481.

Haberle, R. M., C. B. Leovy, and J. B. Pollack, 1982: Some effects of global dust storms on the atmospheric circulation of Mars. *Icarus, 50*, 322–367.

Haberle, R. M., T. P. Ackerman, O. B. Toon, and J. L. Hollingsworth, 1985: Global transport of atmospheric smoke following a major nuclear exchange. *Geophys. Res. Lett., 12*, 405–408.

Harshvardhan, R. Davies, D. A. Randall and T. G. Corsetti, 1987: A fast radiation parameterization for atmospheric circulation models. *J. Geophys. Res., 92*, 1009–1016.

Holton, J. R., 1983: The influence of gravity wave breaking on the general circulation of the middle atmosphere. *J. Atmos. Sci., 40*, 2497–2507.

Houben, H., 1981: A global Martian dust storm model. Presented at Third International Colloquium on Mars, Pasadena.

Hunten, D. M., M. G. Tomasko, F. M. Flaser, R. E. Samuelson, D. F. Strobel, and D. J. Stevenson, 1984: 671–759 in Saturn, T. Gehrels and M. S. Mathews, Ed., Univ. Arizona Press, Tuscon.

Klemp, J. B. and R. B. Wilhelmson, 1978: The simulation of three-dimensional convective storm dynamics. *J. Atmos. Sci., 35*, 1070–1096.

Lacis, A. A., and J. E. Hansen, 1974: A parameterization for the absorption of solar radiation in the Earth's atmosphere. *J. Atmos. Sci., 31*, 118–133.

Leovy, C. B., 1966: Photochemical destabilization of gravity waves near the mesopause. *J. Atmos. Sci., 23*, 223–232.

Leovy, C. B., R. W. Zurek, and J. B. Pollack, 1973: Mechanisms for Mars dust storms. *J. Atmos. Sci., 30*, 749–762.

Leovy, C. B., and R. W. Zurek, 1979: Thermal tides and Martian dust storms: Direct evidence for coupling. *J. Geophys. Res., 84*, 2956–2968.

Leovy, C. B., 1985: The general circulation of Mars: Models and observations. Pp. 327–346 in Issues in Atmospheric and Oceanic Modeling, Part A, Climate Dynamics, Sykuro Manabe, Ed., Academic Press.

Lindzen, R. S., 1966: Radiative and photochemical processes in mesospheric dynamics: Part II, Vertical propagation of long period disturbances at the equator. *J. Atmos. Sci., 23*, 334–343.

Lindzen, R. S., 1966: Radiative and photochemical processes in mesospheric dynamics: Part III, Stability of a zonal vortex at mid-latitudes to axially symmetric disturbances. *J. Atmos. Sci., 23*, 344–349.

Lindzen, R. S., 1966: Radiative and photochemical processes in mesospheric dynamics: Part IV, Stability of a zonal vortex at mid-latitudes to baroclinic waves. *J. Atmos. Sci., 23*, 350–359.

Lindzen, R. S., 1981: Turbulence and stress due to gravity wave and tidal breakdown. *J. Geophys. Res., 86*, 9707–9714.

Malone, R. C., L. H. Auer, G. A. Glatzmaier, M. C. Wood, and O. B. Toon, 1986: Nuclear winter: Three-dimensional simulations including interactive transport, scavenging, and solar heating of smoke. *J. Geophys. Res., 91*, 1039–1054.

Morton, B. R., Sir G. Taylor, and J. S. Turner, 1956: Turbulent gravitational convection from maintained and instantaneous sources. *Proc. Roy. Soc. A, 234*, 1–23.

NRC (National Research Council), 1985: The effects on the atmosphere of a major nuclear exchange. National Academy Press, Washington, DC, 193 pp.

Penner, J. E., L. C. Haselman, and L. L. Edwards, 1986: Smoke plume distribution above large scale fires: Implications for simulations of "nuclear winter." *J. Climate Applied Meteor., 25*, 1434–1444.

Pollack, J. B., O. B. Toon, C. Sagan, A. Summers, B. Baldwin, and W. Van Camp, 1976: Volcanic explosions and climatic change: A theoretical assessment. *J. Geophys. Res., 81*, 1071–1083.

Pollack, J. B., D. S. Colburn, F. M. Flasar, R. Kahn, C. E. Carlston, and D. Pidek, 1979: Properties and effects of dust particles suspended in the Martian atmosphere. *J. Geophys. Res., 84*, 2929–2945.

Rotunno, R., and K. A. Emanuel, 1987: An air-sea interaction theory for tropical cyclones. Part II: Evolutionary study using a nonhydrostatic axisymmetric numerical model. *J. Atmos. Sci., 44*, 542–561.

Schneider, E. K., 1983: Martian great dust storms: Interpretive axially symmetric models. *Icarus, 55*, 302–331.

Smagorinsky, J., 1963: General circulation experiments with the primitive equations. I. The basic experiment. *Mon. Wea. Rev., 91*, 99–164.

Smolarkiewicz, P. K., 1984: A fully multidimensional positive definite advection algorithm with small implicit diffusion. *J. Comp. Phys., 54*, 325–362.

West, R. A., D. F. Strobel, and Martin G. Tomasko: Clouds, aerosols, and photochemistry in the Jovian atmosphere. *Icarus, 65*, 161–217.

Wiscombe, W. J., 1977: The delta-Eddington approximation for a vertically inhomogeneous atmosphere. NCAR Tech. Note 121 + STR.

APPENDIX A. Notation

t	time
x	zonal distance
y	meridional distance
z	vertical distance
p	pressure
u	zonal velocity
v	meridional velocity
w	vertical velocity
ζ	vorticity, $\frac{\partial v}{\partial x} - \frac{\partial u}{\partial y}$
ψ	horizontal streamfunction
Φ	geopotential
θ	potential temperature
q	absorber mixing ratio
ρ_0	atmospheric density
H	density scale height
c_p	specific heat at constant pressure
R	gas constant
κ	thermodynamic ratio R/c_p
N	Brünt-Vaisala frequency
μ	cosine of solar zenith angle
S_0	solar constant
a	specific absorption coefficient
λ	wavelength
Q	radiative heating rate
T	transmissivity from top of atmosphere
f	Coriolis parameter
β	meridional gradient of f
k	zonal wavenumber
ℓ	meridional wavenumber
m	vertical wavenumber
n	vertical wavenumber, $n^2 = m^2 + \left(4H^2\right)^{-1}$
k_2^2	$k^2 + \ell^2$
k_3^2	$k_2^2 + f^2 n^2 / N^2$
α	radiative-dynamical feedback rate
σ	wave frequency (complex)
D	advective operator
ϵ	damping rate or expansion parameter for weak shear
$\overline{(\,)}$	basic state
$(\,)'$	small perturbation from basic state

Appendix B. Numerical Solution of the Eigenvalue Problem

Consider a staggered uniform grid, in which q and ψ are carried at even and odd values, respectively, of the vertical index n. Then (6.20) and (6.21) can be written in the discrete form

$$
\begin{aligned}
&-\left(ik\overline{u}_n + \epsilon_n^u\right) k_2^2 \psi_n + \beta ik\psi_n + \frac{f_0^2}{\rho_n \Delta z^2}\left[\frac{\rho_{n+1}}{N_{n+1}^2}\left(ik\overline{u}_n + \epsilon_{n+1}^T\right)\left(\psi_{n+2} - \psi_n\right)\right] \\
&\quad - \left[\frac{\rho_{n-1}}{N_{n-1}^2}\left(ik\overline{u}_n + \epsilon_{n-1}^T\right)\left(\psi_n - \psi_{n-2}\right)\right] \\
&\quad - ik\psi_n \frac{f_0^2}{\rho_n \Delta z^2}\left[\frac{\rho_{n+1}}{N_{n+1}^2}\left(\overline{u}_{n+2} - \overline{u}_n\right) - \frac{\rho_{n-1}}{N_{n-1}^2}\left(\overline{u}_n - \overline{u}_{n-2}\right)\right] \\
&\quad - \frac{f_0 R}{\rho_n c_p H \Delta z}\left(\frac{Q_{n+1}}{N_{n+1}^2} - \frac{Q_{n-1}}{N_{n-1}^2}\right) = -i\sigma\psi_n + i\sigma\frac{f_0^2}{\rho_n \Delta z}\left[\frac{\rho_{n+1}}{N_{n+1}^2}\left(\psi_{n+2} - \psi_n\right)\right] \\
&\quad - \left[\frac{\rho_{n-1}}{N_{n-1}^2}\left(\psi_n - \psi_{n-2}\right)\right] \quad n = 1, 3, \ldots, 2N-1
\end{aligned}
\tag{B.1}
$$

$$
\begin{aligned}
&\left(ik\overline{u}_n + \epsilon_n^q\right) q_n - \frac{f_0}{N_n^2 \Delta z^2}\left(\overline{q}_{n+1} - \overline{q}_{n-1}\right)\left(ik\overline{u}_n + \epsilon_n^T\right)\left(\psi_{n+1} - \psi_{n-1}\right) \\
&\quad + \frac{ikf_0}{2N_n^2 \Delta z^2}\left(\overline{q}_{n+1} - \overline{q}_{n-1}\right)\left(\overline{u}_{n+1} - \overline{u}_{n-1}\right)\left(\psi_{n+1} + \psi_{n-1}\right) \\
&\quad + \frac{RQ_n}{c_p \rho_n H N^2 \Delta z}\left(\overline{q}_{n+1} - \overline{q}_{n-1}\right) \\
&\quad = i\sigma q_n - \frac{if_0\sigma}{N_n^2 \Delta z^2}\left(\overline{q}_{n+1} - \overline{q}_{n-1}\right)\left(\psi_{n+1} - \psi_{n-1}\right) \quad n = 0, 2, 4, \ldots, 2N
\end{aligned}
\tag{B.2}
$$

where

$$
Q_n = S_0 \overline{T}_n a_n \rho_n \Delta z q_n - S_0\left(\overline{T}_{n+2} - \overline{T}_n\right) \sum_{m=\frac{n+1}{2}}^{N} a_{2m}\ \rho_{2m}\ q_{2m} \quad . \tag{B.3}
$$

Note that the second term on the right hand side of (B.3) is neglected if perturbations in transmissivity are not accounted for. The dependence of the heating on the perturbation absorber concentration can also be evaluated from general radiative transfer models as the Jacobian of the heating with respect to the absorber concentration, evaluated numerically for the basic state absorber distribution. The

excellent agreement between (B.3) and a delta-Eddington model with no scattering supports the use of (B.3) in the absence of scattering.

To complete the formulation of the eigenvalue problem the boundary conditions are expressed

$$f_0\left(ik\overline{u}_n + \epsilon_n^T\right)\left(\psi_{n+1} - \psi_{n-1}\right) - \frac{f_0 ik}{2}\left(\overline{u}_{n+1} - \overline{u}_{n-1}\right)\left(\psi_{n+1} + \psi_{n-1}\right) - \frac{RQ_n\Delta z}{c_p\rho_n H} = f_0 i\sigma\left(\psi_{n+1} - \psi_{n-1}\right) \quad n = 0, 2N \quad . \tag{B.4}$$

Using (B.1)–(B.4) as stencils, the problem reduces to the matrix form

$$\mathbf{A}\mathbf{x} = \sigma\,\mathbf{B}\mathbf{x} \tag{B.5}$$

where

$$\mathbf{x}_n = \begin{cases} q_n & n = 0, 2, 4, \ldots, 2N \\ \psi_n & n = -1, 1, 3, \ldots, 2N+1 \end{cases} \quad . \tag{B.6}$$

Although software is available to solve the general problem (B.5), more reliable solutions can be found by taking advantage of the fact that, for this particular problem, **B** is nonsingular (even in the absence of a basic state absorber). The general problem (B.5) can therefore be transformed to the standard form

$$\mathbf{A}^*\mathbf{x} = \sigma\,\mathbf{x} \tag{B.7}$$

where $\mathbf{A}^* = \mathbf{B}^{-1}\mathbf{A}$. For eigenvalue problems of the form (B.7), software is available from the Numerical Algorithms Group (NAG) library which first "balances" the matrix A* (reduces its norm), solves the resulting eigenvalue problem, and then transforms the eigenvectors back to those of A*. The balancing procedure is particularly important for cases with strong vertical shear and strong radiative-dynamical feedback in the basic state, which produces large differences in the magnitudes of the elements of A*.

Appendix C. Two-Dimensional Model Description

The dynamical model is formulated using the hybrid vertical coordinate (Arakawa and Lamb, 1977)

$$\sigma = \frac{p - p_I}{\pi} \tag{C.1}$$

where p_I is a constant interface pressure and

$$\pi = \begin{cases} \pi_U \equiv p_I - p_T\ , & p \preceq p_I \\ \pi_L \equiv p_S - p_I\ , & p > p_I \end{cases} \quad . \tag{C.2}$$

Thus, π_U represents the (constant) pressure thickness between the interface pressure and the model top p_T, while π_L represents the (variable) pressure thickness between the interface pressure and the surface pressure p_s. For $p < p_I$, surfaces of constant σ are also surfaces of constant pressure. The constant interface pressure must be chosen to be less than the lowest anticipated surface pressure.

The dynamical equations are formulated for either zonally-symmetric flow on a sphere, axially-symmetric flow in a cylinder, or flow through an infinite slab. For all cases the primitive equations can be written

$$\frac{Du}{Dt} - f^* v = E_u + D_u \tag{C.3a}$$

$$\frac{Dv}{Dt} + f^* u + \frac{\partial \Phi}{\partial y} + \sigma \frac{R\theta E}{p} \frac{\partial \pi}{\partial y} = E_v + D_v \tag{C.3b}$$

$$\frac{D\theta}{Dt} = E_\theta + D_\theta + Q/(E c_p \rho_0) \tag{C.3c}$$

$$\frac{\partial \pi}{\partial t} + \frac{1}{c} \frac{\partial}{\partial y}(v \pi c) + \frac{\partial w}{\partial \sigma} = 0 \tag{C.3d}$$

$$\frac{\partial \Phi}{\partial E} = -c_p \theta \quad . \tag{C.3e}$$

Here $y = a\varphi$ for flow on a sphere and $y = r$ for flow in a cylinder, and

$$\frac{D}{Dt} \equiv \frac{\partial}{\partial t} + v \frac{\partial}{\partial y} + \frac{w}{\pi} \frac{\partial}{\partial \sigma} \tag{C.4}$$

where

$$v = \frac{dy}{dt} \tag{C.5}$$

$$w = \pi \frac{d\sigma}{dt} \quad . \tag{C.6}$$

The metric term $c = \cos\varphi$ for a sphere, $c = r$ for a cylinder, and $c = 1$ for a slab. The Coriolis term is $f^* = 2\ \Omega\ \sin\varphi + u/a\ \tan\varphi$ for a sphere, $f^* = f_0 - u/r$ for a cylinder, and $f^* = f_0$ for slab.

The eddy terms E_u, E_v and E_θ represent the effects of transport due to asymmetric motions. On a sphere they are

$$E_u = -\frac{1}{c^2}\frac{\partial}{\partial y}\left(\left[v^*u^*\right]c^2\right) - \frac{1}{\pi}\frac{\partial}{\partial \sigma}\left[w^*u^*\right] \tag{C.7a}$$

$$E_v = -\frac{1}{c}\frac{\partial}{\partial y}\left(\left[v^*v^*\right]c\right) - \frac{1}{\pi}\frac{\partial}{\partial \sigma}\left[w^*v^*\right] - \left[u^*u^*\right]\frac{\tan\varphi}{a} \tag{C.7b}$$

$$E_\theta = -\frac{1}{c}\frac{\partial}{\partial y}\left(\left[v^*\theta^*\right]c\right) - \frac{1}{\pi}\frac{\partial}{\partial \sigma}\left[w^*\theta^*\right] \quad . \tag{C.7c}$$

These can be prescribed, parameterized or neglected.

The terms D_u, D_v and D_θ represent the effects of sub-grid scale turbulent eddy transport which are parameterized to prevent the accumulation of energy on the smallest resolved scales.

In applying the model to mesoscale circulations, the lateral boundary conditions may require special consideration. If the simple boundary condition of no normal flow is applied to the lateral boundaries, gravity waves excited during the geostrophic adjustment process will be reflected back toward the fluid interior, degrading the simulation. Although such reflections are a serious concern in simulations in which latent heat release or orographic forcing are important sources of ageostrophic kinetic energy, they may not be a problem for simulations that neglect those processes. For present purposes, in which latent heat release and orographic forcing are neglected, most of the kinetic energy will be in the geostrophically balanced, rather than inertia gravity mode (provided the radiative heating evolves

on sufficiently long time scales). The only remaining concern with regard to the boundary conditions is that the boundaries be sufficiently far from the sources of kinetic energy that the circulation is unaffected by the rigid boundaries.

C.1. Time Discretization

Time integration of (C.3) is accomplished using the leapfrog scheme with a temporal filter applied to damp the separation of the computational modes. To permit the use of long time steps, many terms are treated implicitly. These include the gravity wave terms, the Coriolis terms, and the vertical diffusion terms. To do so, the equations are linearized about a mean state, which is redefined every few time steps (we do not redefine the basic state every time step because the implicit solution procedure requires that a linear operator be inverted, an expensive procedure; redefining the basic state every, say, ten time steps permits some of the local structure to be treated implicitly).

Upon linearization, the primitive equations become

$$\frac{\partial u}{\partial t} = N_u - v\frac{\partial \overline{u}}{\partial y} + \overline{f}^* v + \frac{1}{\overline{\pi}}\frac{\partial}{\partial \sigma}\frac{\overline{p}^2 K}{H^2 \overline{\pi}}\frac{\partial u}{\partial \sigma} \tag{C.9a}$$

$$\frac{\partial v}{\partial t} = N_v - \overline{f}^* u - \frac{\partial \Phi'}{\partial y} - \sigma\frac{R\overline{\theta}\,\overline{E}}{\overline{p}}\frac{\partial \pi}{\partial y} + \frac{1}{\overline{\pi}}\frac{\partial}{\partial \sigma}\frac{\overline{p}^2 K}{H^2 \overline{\pi}}\frac{\partial v}{\partial \sigma} \tag{C.9b}$$

$$\frac{\partial \theta}{\partial t} = N_\theta - \frac{w}{\overline{\pi}}\frac{\partial \overline{\theta}}{\partial \sigma} + \frac{1}{\overline{\pi}}\frac{\partial}{\partial \sigma}\frac{\overline{p}^2 K}{H^2 \overline{\pi}}\frac{\partial \theta}{\partial \sigma} \tag{C.9c}$$

$$\frac{\partial \pi}{\partial t} = N_\pi - \frac{1}{c}\frac{\partial}{\partial y}(\overline{\pi} v c) - \frac{\partial w'}{\partial \sigma} \quad . \tag{C.9d}$$

Here N_u, N_v, N_θ, N_π represent those terms not accounted for by the linear terms, i.e., they are calculated as the total terms minus the linear terms. The perturbation geopotential represents that part of the geopotential which depends linearly on θ and π. The perturbation vertical velocity is calculated from

$$w' = \begin{cases} -\frac{1}{c}\frac{\partial}{\partial y}\int_{-1}^{\sigma} \overline{\pi} v c \, d\sigma & -1 < \sigma \leq 0 \\ -\frac{1}{c}\frac{\partial}{\partial y}\left(\int_{-1}^{1} \overline{\pi} v c \, d\sigma - \sigma \int_{-1}^{1} \overline{\pi} v d\sigma\right) & 0 < \sigma < 1 \end{cases} \quad . \tag{C.10}$$

Note that the mean state assumes $\overline{w} = \overline{v} = 0$.

Upon vertical discretization, equations (C.9) become

$$\frac{\partial \mathbf{u}}{\partial t} = \mathbf{N}_u + \mathbf{L}_{uv}\mathbf{v} + \mathbf{K}\ \mathbf{u} \tag{C.11a}$$

$$\frac{\partial \mathbf{v}}{\partial t} = \mathbf{N}_v + \mathbf{L}_{vu}\mathbf{u} - \mathbf{L}_{\Phi\theta}\frac{\partial}{\partial y}\Theta - \mathbf{L}_{\Phi\pi}\frac{\partial \pi}{\partial \varphi} + \mathbf{K}\ \mathbf{v} \tag{C.11b}$$

$$\frac{\partial \Theta}{\partial t} = \mathbf{N}_\theta + \mathbf{L}_{\theta v}\frac{1}{c}\frac{\partial}{\partial y}(\mathbf{v}c) + \mathbf{K}\Theta \tag{C.11c}$$

$$\frac{\partial \pi}{\partial t} = \mathrm{N}_\pi + \mathbf{L}^T_{\pi\dot{v}}\frac{1}{c}\frac{\partial}{\partial y}(\mathbf{v}c) \quad . \tag{C.11d}$$

Here the column fields have been represented as vectors. The linear matrix operators $\mathbf{L}_{uv}$, $\mathbf{L}_{vu}$, $\mathbf{L}_{\theta v}$, $\mathbf{L}_{\Phi\theta}$, $\mathbf{L}_{\Phi\pi}$, $\mathbf{L}_{\pi v}$ and $\mathbf{K}$ are defined later, when the details of spatial differencing are discussed.

Treating the linear terms implicitly, the time-differenced form of (C.11) becomes

$$\mathbf{u}^{n+1} = \mathbf{u}^{n-1} + 2\Delta t\left[\mathbf{N}^n_u + \frac{1}{2}\mathbf{L}_{uv}\left(\mathbf{v}^{n+1} + \mathbf{v}^{n-1}\right) + \mathbf{K}\ \mathbf{u}^{n+1}\right]$$

$$\mathbf{v}^{n+1} = \mathbf{v}^{n-1} + 2\Delta t\left[\mathbf{N}^n_v + \frac{1}{2}\mathbf{L}_{vu}\left(\mathbf{u}^{n+1} + \mathbf{u}^{n-1}\right)\right] \tag{C.12a}$$

$$\left[-\frac{1}{2}\mathbf{L}_{\Phi\theta}\frac{\partial}{\partial y}\left(\Theta^{n+1} + \Theta^{n-1}\right) - \frac{1}{2}\mathbf{L}_{\Phi\pi}\frac{\partial}{\partial y}\left(\pi^{n+1} + \pi^{n-1}\right) + \mathbf{K}\ \mathbf{v}^{n+1}\right] \tag{C.12b}$$

$$\Theta^{n+1} = \Theta^{n-1} + 2\Delta t\left[\mathbf{N}^n_\theta + \frac{1}{2}\mathbf{L}_{\theta v}\frac{1}{c}\frac{\partial}{\partial y}\left(\mathbf{v}^{n+1}c + \mathbf{v}^{n-1}c\right) + \mathbf{K}\Theta^{n+1}\right] \tag{C.12c}$$

$$\pi^{n+1} = \pi^{n-1} + 2\Delta t\left[N^n_\pi + \frac{1}{2}\mathbf{L}^T_{\pi v}\cdot\frac{1}{c}\frac{\partial}{\partial y}\left(\mathbf{v}^{n+1}c + \mathbf{v}^{n-1}c\right)\right] \quad . \tag{C.12d}$$

Note that backward implicit differencing is used for the vertical diffusion terms, but centered implicit differencing is applied to the remaining linear terms.

Reducing the four time-differenced equations to a single equation for $\mathbf{v}^{n+1}$, equations (C.12) become

$$\left(\mathbf{I}_K - \Delta t^2\mathbf{L}_{vv}\right)\mathbf{v}^{n+1} = \left(\mathbf{I} + \Delta t^2\mathbf{L}_{vv}\right)\mathbf{v}^{n-1}$$
$$+ \Delta t\left[2\mathbf{N}^n_v + \mathbf{L}_{vu}\mathbf{u}^{n-1} - \mathbf{L}_{\Phi\theta}\frac{\partial}{\partial y}\,\Theta^{n-1} - \mathbf{L}_{\Phi\pi}\frac{\partial}{\partial y}\pi^{n-1}\right]$$

$$+ \mathbf{L}_{vu}\mathbf{I}_K^{-1}\left(\mathbf{u}^{n-1} + 2\Delta t\mathbf{N}_u^n\right) - \left[\mathbf{L}_{\Phi\theta}\mathbf{I}_K^{-1}\frac{\partial}{\partial y}\left(\Theta^{n-1} + 2\Delta t\mathbf{N}_\theta^n\right)\right]$$
$$- \left[\mathbf{L}_{\Phi\pi}\frac{\partial}{\partial y}\left(\pi^{n-1} + 2\Delta t N_\pi^n\right)\right] \tag{C.13}$$

where

$$\mathbf{L}_{vv}(\mathbf{v}) \equiv \mathbf{L}_{vu}\mathbf{I}_K^{-1}\mathbf{L}_{uv}\mathbf{v} - \mathbf{L}_{\Phi\theta}\mathbf{I}_K^{-1}\frac{\partial}{\partial y}\left(\mathbf{L}_{\theta v}\frac{1}{c}\frac{\partial}{\partial y}(\mathbf{vc})\right)$$
$$- \mathbf{L}_{\theta\pi}\frac{\partial}{\partial y}\left(\mathbf{L}_{\pi v}\frac{1}{c}\frac{\partial}{\partial y}(\mathbf{vc})\right) \tag{C.14}$$

and

$$\mathbf{I}_K = \mathbf{I} - 2\Delta t\mathbf{K} \quad . \tag{C.15}$$

The solution of (C.13) for $\mathbf{v}^{n+1}$, (C.12a) for $\mathbf{u}^{n+1}$, (C.12c) for Θ^{n+1}, and (C.12d) for π^{n+1} is accomplished by standard Gaussian elimination techniques, given appropriate spatial discretization. Finally, to prevent the spurious amplification of the computation mode arising from the leapfrog scheme, a weak time filter (Asselin, 1972) is applied each time step.

C.2. Spatial Discretization

A staggered grid is employed, with the prognostic variables $u_{\ell j}, \theta_{\ell j}$, and π_j carried on the primary grid, $v_{\ell j+1/2}$ carried at intermediate horizontal points, and $w_{\ell+1/2j}$ carried at intermediate levels. Vertical finite differencing follows Arakawa and Suarez (1983); horizontal differencing employs the C grid treatment of Arakawa and Lamb (1977). In the usual implementation of the model, levels above the interface pressure p_I are spaced equally in log pressure, whereas levels below p_I are spaced equally in pressure. This treatment permits the resolution of shallow processes in the lower troposphere while retaining the preferred equal spacing with height in the stratosphere.

Whereas the details of the spatial finite difference treatment of the full dynamical terms can be found in Arakawa and Lamb (1977) and Arakawa and Suarez

(1983), the linear operators $\mathbf{L}_{uv}$, $\mathbf{L}_{vu}$, $\mathbf{L}_{\theta v}$, $\mathbf{L}_{\bar{\Phi}\theta}$, $\mathbf{L}_{\bar{\Phi}\pi}$, $\mathbf{L}_{\pi v}$, and $\mathbf{K}$, required for the implicit time integration scheme, remain to be defined. These defintions are given below.

$$\left(\mathbf{L}_{uv}\mathbf{v}\right)_j = \mathbf{L}^+_{uv}(j)\mathbf{v}_{j+1/2} + \mathbf{L}^-_{uv}(j)\mathbf{v}_{j-1/2} \tag{C.16a}$$

where

$$L^+_{uv}(\ell,k,j) = \delta_{\ell k}\left[\frac{1}{2}f^*_{\ell j} - \frac{\overline{u}_{\ell j+1} - \overline{u}_{\ell j}}{2\Delta y_{j+1/2}}\right] \tag{C.16b}$$

$$L^-_{uv}(\ell,k,j) = \delta_{\ell k}\left[\frac{1}{2}f^*_{\ell j} - \frac{\overline{u}_{\ell j} - \overline{u}_{\ell j-1}}{2\Delta y_{j-1/2}}\right] \tag{C.16c}$$

and $\delta_{\ell k}$ is the Kronecker delta.

$$\left(\mathbf{L}_{vu}\mathbf{u}\right)_{j+1/2} = \mathbf{L}^+_{vu}\left(j+1/2\right)\mathbf{u}_{j+1} + \mathbf{L}^-_{vu}\left(j+1/2\right)\mathbf{u}_j \tag{C.17a}$$

where

$$L^+_{vu}(\ell,k,j+1/2) = -\delta_{\ell k}\frac{c_{j+1}\Delta y_{j+1}}{c_j\Delta y_j + c_{j+1}\Delta y_{j+1}} \quad f^*_{\ell j+1} \tag{C.17b}$$

$$L^-_{vu}(\ell,k,j+1/2) = -\delta_{\ell k}\frac{c_j\Delta y_j}{c_j\Delta y_j + c_{j+1}\Delta y_{j+1}} \quad f^*_{\ell j} \tag{C.17c}$$

$$\mathbf{L}_{\theta v} = \mathbf{L}_{\theta w}\mathbf{L}_{wv} \tag{C.18a}$$

where

$$L_{\theta w}(\ell,k,j) = \begin{cases} \left(\frac{\overline{\theta}_\ell - \overline{\theta}_{\ell-1/2}}{\overline{\pi}_\ell \Delta\sigma_\ell}\right)_j & k = \ell - 1 \\ \left(\frac{\overline{\theta}_{\ell+1/2} - \overline{\theta}_\ell}{\overline{\pi}_\ell \Delta\sigma_\ell}\right)_j & k = \ell \end{cases} \tag{C.18b}$$

$$L_{wv}(\ell,k) = \begin{cases} \overline{\pi}_k\Delta\sigma_k & k \le \ell \quad \ell \le I \\ 0 & k > \ell \quad \ell \le I \\ (1-\sigma)_{\ell+1/2}\overline{\pi}_k\Delta\sigma_k & k \le \ell \quad I < \ell < L \\ -\sigma_{\ell+1/2}\overline{\pi}_k\Delta\sigma_k & k > \ell \quad I < \ell < L \\ 0 & \ell = L \end{cases} \tag{C.18c}$$

$$L_{\bar{\Phi}\theta}(\ell,k) = c_p \begin{cases} \overline{E}_s - \overline{E}_L & \ell = k = L \\ \overline{E}_s - \overline{E}_L - \overline{E}_{L-1/2} - \overline{E}_{L-1} & \ell < k = L \\ \overline{E}_{k-1/2} - \overline{E}_{k-1} + \overline{E}_{k+1} - \overline{E}_{k+1/2} & \ell < k < L \\ \overline{E}_{k+1} - \overline{E}_{k+1/2} & \ell = k < L \\ 0 & k < \ell < L \end{cases} \tag{C.19}$$

$$L_{\bar{\Phi}\pi}(\ell) = L_{\bar{\Phi}\pi}(\ell+1) + c_p\overline{\theta}_{\ell+1/2}\left[\left(\frac{dE}{d\pi}\right)_{\ell+1} - \left(\frac{dE}{d\pi}\right)_\ell\right] \tag{C.20a}$$

$$L_{\Phi\pi}(L) = c_p\overline{\theta}_L\left[\left(\frac{dE}{d\pi}\right)_S - \left(\frac{dE}{d\pi}\right)_L\right] \tag{C.20b}$$

$$L_{\pi v}(\ell) = \overline{\pi}_\ell \Delta\sigma_\ell \tag{C.21}$$

$$K_{\ell,\ell+1} = -\frac{\overline{p}^2_{\ell+1/2}K_{\ell+1/2}}{\left(\overline{p}_{\ell+1/2} - \overline{p}_{\ell-1/2}\right)H^2_{\ell+1/2}\left(\overline{p}_{\ell+1} - \overline{p}_\ell\right)} \quad 1 \le \ell < L \tag{C.22a}$$

$$K_{\ell,\ell-1} = -\frac{\overline{p}^2_{\ell-1/2}K_{\ell-1/2}}{\left(\overline{p}_{\ell+1/2} - \overline{p}_{\ell-1/2}\right)H^2_{\ell-1/2}\left(\overline{p}_\ell - \overline{p}_{\ell-1}\right)} \quad 2 \le \ell \le L \tag{C.22b}$$

$$K_{\ell,\ell} = -K_{\ell,\ell+1} - K_{\ell,\ell-1} \quad 1 \le \ell \le L \quad . \tag{C.22c}$$

It should be noted here that because the vertical diffusion term depends on the surface value ψ_s, the term $(K_{LL} + K_{LL-1})\psi_s$ must be treated as a forcing term in the equations.

C.3. Source Terms

In addition to the background vertical diffusion, source terms consist of solar and longwave radiative heating, several convective adjustments, an inertial adjustment, a slantwise adjustment, and a treatment of mixing based on horizontal and vertical shear.

Solar heating is treated using Wiscombe's delta-Eddington model. For simplicity the only absorbers are ozone and smoke. Although scattering is the forte of the delta-Eddington method, it is neglected in the experiments discussed in Chapter 9. To treat ozone absorption, which is nongrey, the absorption of the direct beam is matched with the total absorption given by the formulae of Lacis and Hansen (1974), i.e.,

$$1 - \exp(-\tau/\mu) = A(u/\mu) \tag{C.23}$$

where τ is the optical depth from the top of the atmosphere, u is the ozone vertical path length from the top of the atmosphere, and A is the Lacis and Hansen total

absorption. The optical depth of any layer is then the difference between the optical depths to the bottom and top of the layer.

Longwave radiative heating is calculated by the Harshvardhan et al. (1987) model, which treats absorption by water vapor, CO_2, and ozone. In addition, the capability to treat the longwave absorption by smoke has been added. The water vapor and ozone distributions are taken from the AFGL midlatitude summer profiles.

Convective adjustments include adjustments to a dry adiabat, a moist adiabat, and a stable stratification in which potential temperature increases with altitude at the rate 3 K km^{-1}. In each case heat is conserved under the adjustment. A somewhat different algorithm than the traditional Manabe scheme has been developed which is considerably more efficient when many levels are adjusted. Rather than adjust temperatures to the average temperature of adjacent layers,

$$\overline{\theta} = (w_1\theta_1 + w_2\theta_2)/(w_1 + w_2) \tag{C.24}$$

where w_1 and w_2 are weights depending on layer thickness, the Exner function, etc., the average temperature involves multiple layers. If, for example, two adjacent levels are found to be supercritical, $\overline{\theta}$ is defined to be the weighted average of the two levels, as above. The levels adjacent to these two levels (above and below the convecting region) are then tested for stability, not on the basis of the value of θ at the adjacent levels, but on the basis of $\overline{\theta}$. The weighted average is then redefined to account for these new convecting layers,

$$\overline{\theta} = \frac{\sum w_\ell \theta_\ell}{\sum w_\ell} \tag{C.25}$$

and the procedure moves on to the next pair of adjacent levels above and below the convecting region. The significant difference from the traditional scheme is that θ in each layer is not reset to $\overline{\theta}$ until the limits of convection have been determined.

The net result is identical to the traditional solution (to within the accuracy of the iterative solution technique), but at a fraction of the cost.

In the same spirit of convective adjustments, the zonal velocity (i.e., the velocity component perpendicular to the plane of symmetry) is adjusted horizontally when the conditions for inertial instability are satisfied. Following Holton (1983), the zonal windfield is adjusted toward constant angular momentum when the sign of the absolute vorticity differs from the sign of the Coriolis parameter. Angular momentum is conserved under the adjustment.

In some circumstances the atmosphere can be convectively and inertially stable, yet unstable with respect to slantwise convection (Emanuel, 1983). A slantwise adjustment has therefore been added, which adjusts potential temperature along lines of constant angular momentum when the slope of isentropes exceeds that of lines of constant angular momentum. The adjustment could in principle instead consist of a transport of angular momentum along the isentropes, the difference between the two methods being absorbed by geostrophic adjustment. In practice the geostrophic adjustment process is not well represented by the long time steps of the model, and unsatisfactory circulations develop. This problem has been circumvented for the time being by avoiding circumstances in which slope of the isentropes exceeds that of the line of constant angular momentum, i.e., cases in which the Ertel potential vorticity becomes negative.

Horizontal and vertical mixing due to shears in the zonal and meridional wind is represented following Rotunno and Emanuel (1987). The horizontal mixing length is chosen to be 10 km, while the vertical mixing length is 200 m.

Finally, advection of the absorber mixing ratio is accomplished using the Smolarkiewicz (1984) algorithm (kindly written by K. E. Taylor), which minimizes numerical diffusion while maintaining positive mixing ratio concentrations.

Parameter values for the experiments described in Chapter 9 include Coriolis parameter 10^{-4} s^{-1}, time step 3600 s, internal vertical diffusivity 5 m^2 s^{-1}, and surface diffusivity 20 m^2 s^{-1}.